AN ANALYTIC APPROACH TO ELECTROMAGNETIC SCATTERING PROBLEMS

Proefschrift

ter verkrijging van de graad van doctor
aan de Technische Universiteit Delft,
op gezag van de Rector Magnificus prof.dr.ir. J.T. Fokkema,
voorzitter van het College voor Promoties,
in het openbaar te verdedigen op

donderdag 28 juni 2007 om 15.00 uur

door

Janne Maria BROK

natuurkundig ingenieur
geboren te 's-Hertogenbosch.

Dit proefschrift is goedgekeurd door de promotor:
prof.dr. H.P. Urbach

Samenstelling promotiecommissie:

Voorzitter	
Rector Magnificus,	Technische Universiteit Delft
Promotor	
prof.dr. H.P. Urbach,	Technische Universiteit Delft
Leden	
prof.dr.ir. J.J.M. Braat,	Technische Universiteit Delft
prof.dr.ir. P.M. van den Berg,	Technische Universiteit Delft
prof.dr. M.S. Soskin,	National Academy of Science of Ukraine
prof.dr. G.W. ’t Hooft,	Universiteit Leiden
prof.dr.ir J. de Graaf,	Technische Universiteit Eindhoven
dr H.J.W.M Hoekstra,	Universiteit Twente

This research was supported by the Dutch Technology Foundation STW.

Cover: Cypressen nabij Poggibonsi, Italië 2002.

ISBN 978-90-78314-07-3

Summary

An analytic approach to electromagnetic scattering problems

Electromagnetic scattering problems deal with the diffraction of electromagnetic radiation by objects or apertures. The effects of diffraction are mostly noticeable when the wavelength of the radiation is of the same order of magnitude as the feature sizes of the diffracting objects or apertures. For a rigorous solution of a scattering problem one has to solve, for a given incident field, the Maxwell equations with the appropriate boundary conditions for the total field at the boundaries of the scattering bodies. Only for a few objects and apertures analytical solutions have been derived.

In this thesis we present a mode expansion theory to model rigorously the scattering from three-dimensional pits and holes that are pressed in a perfectly conducting metal layer. The metal layer has a finite thickness and the sizes of the holes and pits are of the same order of magnitude as the wavelength of the scattering light. The total electromagnetic field above and below the conducting layer is written as an integral over plane waves. These plane waves can be S- or P-polarized and they can be propagating or evanescent. The field inside the pits and holes is expanded into waveguide modes, that can have TE or TM polarization and can also be propagating or evanescent.

A system of equations is derived by matching the tangential field components at the interfaces. As unknowns, this system only contains the expansion coefficients of the waveguide modes. Therefore the number of unknowns is small. Once the system of equations of a particular diffraction geometry is computed, important parameters such as the thickness of the conducting layer and the index of refraction inside the pit or hole can be varied with negligible computational effort.

The right-hand side of the system of equations is determined by the incident field. The incident field can consists of one or several plane waves or a continuum of plane waves. These originate from a (not specified) source located at infinity. Our model, in addition, allows for an oscillating electric dipole as the source of electromagnetic radiation. This dipole can be located inside a pit or hole, as well as above or below the perfectly conducting layer.

Except for absorption, all relevant physics is present in the model. This means

that, apart from the microwave and terahertz frequency regimes, the results found can also be of use in the optical domain, as long as the penetration depth inside the metal is not too large as compared to the thickness of the metal layer and the distances between the holes or pits.

We compared calculations, obtained with our mode expansion technique, with experimental results on the scattering of a teraherz pulse. The near field of this pulse was measured at the shadow side of an aluminum foil with square holes. Our calculations were found to be in excellent agreement with these near field measurements.

Furthermore, we have studied the transmission of energy through single and multiple holes. We have found that extraordinary transmission occurs for a single hole when the lowest order waveguide mode is just above cutoff. This is due to the Fabry-Perot resonance of this lowest order mode inside the waveguide. We have also calculated the transmission through two and three holes. From this analysis we concluded that the presence of a second and third hole can increase or decrease the transmission through the first hole. As this is not the case for all polarizations, we concluded that electromagnetic surface waves are responsible for this modulation in the transmission.

We have studied the behavior of optical vortices inside holes as well as the transmission of angular momentum through holes. We used a Laguerre-Gaussian mode as incident field. As degree theory predicts, the total topological charge in a plane inside the hole can change only if a vortex either appears or disappears via the walls of the hole. If this is not the case, the total topological charge is conserved. This means that pairs of oppositely handed vortices may appear abruptly within the area of the hole. When studying the transmission of angular momentum of a hole, we have found that, depending on the size of the hole and the thickness of the conducting layer, angular momentum can be transferred from the field to the surface currents of the perfect conductor. However, angular momentum can also be transferred from the currents to the field.

Spontaneous emission is the phenomenon of the transition of an excited state to a state with lower energy by the interaction of this excited state with vacuum fluctuations. When an excited state is placed near an interface between optically different materials, the spontaneous emission rate is changed with respect to the spontaneous emission in free space. Although spontaneous emission can not be explained by classical electromagnetics, it is possible to calculate relative spontaneous emission rates: the relative spontaneous emission for an excited state near some kind of interface is equal to the total emitted radiation of the oscillating dipole, normalized by the total emitted radiation of the free space dipole.

We have examined the relative spontaneous emission for dipoles located inside pits and holes, as well as above and below the conducting layer. We have found that a dipole that is oriented in the plane of the conducting layer excites other waveguide modes than a dipole that is oriented perpendicular to the conducting layer. As a consequence, the relative spontaneous emission of a parallel dipole is reduced for pits and holes with a width that is smaller than half the wavelength λ. For a perpendicular dipole, the relative spontaneous emission is reduced when the width is smaller than $\lambda/\sqrt{2}$. The spontaneous emission can be enhanced by a factor 3 to 5 if the size of the hole or pit is chosen well. Close to the edges of the holes, however, the relative spontaneous emission can be orders of magnitude larger, due to the infinite fields that occur near sharp edges.

Janne Brok, May 2007

Samenvatting

Een analytische aanpak voor elektromagnetische verstrooiingsproblemen

Dit proefschrift gaat over de verstrooiing van licht door metalen structuren. Wanneer een lichtstraal op zijn weg door de ruimte een verandering in de optische dichtheid tegenkomt, dan verandert de voortplantingsrichting van het licht. Een voorbeeld hiervan is de *buiging* van licht aan het scheidingsoppervlak tussen lucht en water. Omdat water een andere optische dichtheid heeft dan lucht, is de voortplantingsrichting van de lichtstraal in water anders dan in lucht. Daardoor lijkt het alsof een voorwerp, dat zich deels boven en deels onder water bevindt, op het scheidingsoppervlak vervormd wordt. Een ander voorbeeld is de *reflectie* van licht door een spiegelend oppervlak.

Naast buiging en reflectie is er nog een derde manier waarop de voortplantingsrichting van licht kan veranderen en dat is *verstrooiing*. Verstrooiing treedt vooral op als de afmeting van de verstrooiende structuur zeer klein is. Hoe klein is klein? Ongeveer even groot als de *golflengte* van het licht dat erop valt. Dat licht eigenlijk een golfverschijnsel is, kun je met het blote oog niet zien. Dit komt doordat de golflengte van licht te klein is. De golflengte van een golf op het strand is een paar meter. De golflengte van het voor ons zichtbare licht van de zon zit tussen de 400 en 700 nanometer. En een nanometer is een miljardste van een meter. De golflengte van licht is ongeveer 100 keer kleiner dan de dikte van een haar. Geen wonder dat we licht niet kunnen zien golven. Maar als het licht op een structuur valt die ongeveer even groot is als de golflengte van het licht, dan kunnen we het effect van die golfbeweging wel zien. Het licht wordt dan namelijk door de structuur in alle richtingen verstrooid. We zien dan geen spiegeling, maar juist een diffuus effect: een verstrooiend oppervlak ziet er wat doffer uit.

Hoe structuren, die ongeveer dezelfde afmeting hebben als de golflengte van het licht, dit licht precies verstrooien, is een natuurkundig probleem dat niet zo gemakkelijk op te lossen is. We weten dat de verstrooiing van licht beschreven wordt door de zogenaamde *Maxwell vergelijkingen*. De Schot James Clark Maxwell heeft deze wiskundige vergelijkingen in 1864 voor het eerst als een samenhangend geheel opgeschreven. Hij toonde aan dat licht een elektromagnetisch fenomeen is en dat lichtgolven elektromagnetische golven zijn. De Maxwell vergelijkingen geven een verband tussen de elektrische en magnetische velden waaruit licht bestaat en tussen elektrische ladingen en stromen.

We beschikken dus over de wiskundige vergelijkingen waaraan de elektromagnetische velden die door kleine structuren verstrooid worden, moeten voldoen. Dit betekent niet dat we voor een specifiek verstrooiingsprobleem deze vergelijkingen gemakkelijk op kunnen lossen. Voor de meeste verstrooiingsproblemen zijn de oplossingen van de Maxwell vergelijkingen erg moeilijk. Met krachtige computers en veel rekenkracht kunnen we in veel gevallen een heel eind komen, maar in dit proefschrift gebruiken we een elegantere manier om de Maxwell vergelijkingen op te lossen. We gebruiken een *analytische* aanpak, die ons in staat stelt beter te begrijpen hoe die ingewikkelde Maxwell vergelijkingen werken.

Hoe werkt deze analytische aanpak? Om dit uit te leggen moeten we eerst nader ingaan op de precieze vorm die de structuur heeft waardoor het licht wordt verstrooid. In dit proefschrift is deze structuur een vlakke, metalen plaat waarin rechthoekige putten en gaten zitten. De afmetingen van die putten en gaten zijn ongeveer even groot als de golflengte van het licht. Een dergelijke metalen plaat zou bijvoorbeeld model kunnen staan voor een DVD disk, waarop men tegenwoordig informatie zoals films en muziek op kan slaan. De informatie op deze disk is gecodeerd met behulp van putjes die verschillende lengtes hebben. Als je naar een DVD disk kijkt, kun je deze putjes niet onderscheiden, want daar zijn ze te klein voor. De verschillende kleuren die je ziet, zijn echter wel een gevolg van de verstrooiing van het licht door deze putjes.

De geometrie van een vlakke metalen plaat met rechthoekige putten en gaten die in dit proefschrift bestudeerd wordt, komt in de praktijk veel vaker voor. Het is dus handig als we de verstrooiing van licht door een dergelijke geometrie kunnen beschrijven en begrijpen. Hiervoor maken we wel een belangrijke aanname. Deze aanname is dat het metaal waaruit de plaat bestaat niet zomaar een metaal is, maar een geïdealiseerd metaal. We noemen dit een *perfect metaal*. Dat betekent dat dit metaal geen licht absorbeert. Al het licht dat op het perfecte metaal valt, wordt weerkaatst. In welke richting het weerkaatst wordt, moet berekend worden met de Maxwell vergelijkingen, maar dat het weerkaatst wordt is een aanname die we van tevoren gedaan hebben.

Nu we weten over welke verstrooiende structuur we het hebben, kunnen we wat dieper ingaan op de analytische aanpak die we hier gebruiken. Een synoniem van analyse is ontledingskunst. We ontleden het verstrooiingsprobleem in meerdere deelproblemen en die deelproblemen lossen we afzonderlijk op. Het eerste deelprobleem is de vraag hoe het elektromagnetische veld eruit ziet in de putten en gaten. Uit de Maxwell vergelijkingen blijkt dat we dit veld kunnen schrijven als een som van *basisfuncties*. Deze basisfuncties zijn als het ware de bouwstenen van het elektromagnetische veld in de putten en gaten. Ze vertonen een gelijkenis met de staande golven zoals die bijvoorbeeld voorkomen in het vlies van een trommel. Het tweede deelprobleem is de vraag hoe het elektromagnetische veld eruit ziet boven en onder de metalen plaat. Ook hier kunnen we het veld schrijven als een som van basisfuncties. Deze basisfuncties worden vlakke golven genoemd. Om je iets voor te stellen bij een vlakke golf kun je denken aan de 'wave' die toeschouwers in een stadion samen kunnen maken.

Op het metaal zelf na, hebben we nu een beschrijving voor het elektromagnetische veld in de gehele ruimte. Maar vanwege de aanname van het perfecte metaal is er helemaal geen elektromagnetisch veld in het metaal. Dus nu zijn we toe aan het derde en laatste deelprobleem: hoe brengen we de twee beschrijvingen van het elektromagnetische veld in de putten en gaten enerzijds en boven en onder de metalen plaat anderzijds met elkaar in overeenstemming? Hiervoor hebben we weer de Maxwell vergelijkingen nodig. Deze vertellen wat de randvoorwaarden zijn waaraan het elektromagnetische veld moet voldoen en hoe we deze beschrijvingen aan elkaar moeten plakken.

We hebben nu de titel van dit proefschrift uitgelegd. We zullen nu nog een korte uitleg geven van de inhoud van de verschillende hoofdstukken. Na een inleiding in Hoofdstuk 1, wordt de theorie van de deelproblemen in Hoofdstuk 2, 6 en 7 uitgewerkt voor drie versies van het verstrooiingsprobleem. In Hoofdstuk 2 behandelen we de verstrooiing aan een metalen plaat met een klein (eindig) aantal putten en gaten. Hoofdstuk 6 handelt over verstrooiing aan een metalen plaat met een periodiek rooster van putten en gaten. Hoofdstuk 7 gaat over de mogelijkheid dat een elektromagnetische bron zich dichtbij of in de putten en gaten bevindt.

Verschillende toepassingen van de theorie worden behandeld in de overige hoofdstukken. Zo zijn Hoofdstukken 3, 4 en 5 gebaseerd op de theorie van Hoofdstuk 2. In Hoofdstuk 3 worden resultaten van experimenten vergeleken met berekeningen. Uit deze vergelijking blijkt dat onze analytische aanpak van het verstrooiingsprobleem uitstekend werkt. Hoofdstuk 4 gaat over de transmissie van energie door een eindig aantal gaten. Door de grootte en afstand tussen de gaten te veranderen, kan deze transmissie beïnvloed worden. Hoofdstuk 5 gaat over de transmissie van hoekimpuls door enkele gaten. Hierbij is het invallende licht geen vlakke golf, maar een gefocusseerde bundel met een spiraalvormige golfstructuur. Hoofdstuk 8, tot slot, is een toepassing van de theorie van Hoofdstuk 7. Dit hoofdstuk gaat over een kwantummechanisch verschijnsel dat spontane emissie heet. Hoewel de kwantummechanica een theorie is die geavanceerder is dan de theorie van Maxwell, blijkt het zo te zijn dat het verschijnsel van spontane emissie onder bepaalde voorwaarden toch met de theorie van Maxwell kan worden berekend en onze analytische aanpak blijkt daarvoor zeer geschikt.

Janne Brok, mei 2007

Man kann diese wunderbare Theorie nicht studieren, ohne bisweilen die Empfindung zu haben, als wohne den mathematischen Formeln sebständiges Leben und eigener Verstand inne, als seien dieselben klüger als wir, klüger sogar als ihr Erfinder, als gäben sie uns mehr heraus, als seinerzeit in sie hineingelegt wurde. Es ist dies auch nicht geradezu unmöglich; es kann eintreten, wenn nämlich die Formeln richtig sind über das Maß dessen hinaus, was der Erfinder sicher wissen konnte. Freilich lassen sich solche umfassenden und richtigen Formeln nicht finden, ohne daß mit dem schärfsten Blicke jede leise Andeutung der Wahrheit aufgefaßt wird, welche die Natur durchscheinen läßt.

Heinrich Hertz, September 1889
Über die Beziehungen zwischen Licht und Elektrizität

Men kan deze prachtige theorie niet bestuderen, zonder zo nu en dan het gevoel te krijgen dat deze wiskundige vergelijkingen een zelfstandig leven leiden en een eigen verstand bezitten, dat zij wijzer zijn dan wij, zelfs wijzer dan hun geestelijke vader, dat ze ons meer geven dan er ooit werd ingestopt. Dit is ook niet onmogelijk; het kan zijn dat de vergelijkingen waar zijn op een manier die de kennis van de ontdekker ontstijgt. Nochtans laten zulke veelomvattende en juiste vergelijkingen zich pas dan ontdekken, als iedere subtiele hint naar de waarheid, die de natuur prijsgeeft, met de scherpste blik wordt geduid.

(Mijn vertaling)

Contents

Chapter 1

Introduction

1.1 On the notion of scale in physical theories

In the historic development of the science of physics, people began by describing phenomena around them that happened at human scales: for example length scales of the order of one meter and energy scales of the order of one Joule.

When a theory for a certain phenomenon was established and found to be correct, the applicability of this theory was challenged for other scales than the scale for which it was intended. This then led to refined or new theories that had a broader range of validity. In many cases, the old theory turned out to be a limiting case of the new theory.

This line of development is especially true for the theory of optics and electromagnetism. The law of reflection was known to the ancient Greeks and the law of refraction was discovered in 1621 by Snell. These two laws belong to the realm of geometrical or ray optics. In this theory, the order of magnitude of the wavelength of the light is assumed to be much smaller than the order of magnitude of the details of the reflecting of refracting structures, that are of a scale that can be seen with the human eye.

To understand the interaction of light with objects that have much smaller sizes, or, more precisely, sizes of the order of the wavelength, we have to apply the more refined theory of classical electrodynamics. An example of a limiting case of classical electrodynamics is the far field approximation.

In retrospective, we can say that the discovery of the theory of classical electrodynamics in 1864 by Maxwell was one of the great moments in the history of science, as it unified the optics with the field of electric and magnetic phenomena. Moreover, this theory is valid for a vast range of length scales, as it is able to explain wave phenomena from gamma rays with wavelengths of picometers to radio waves with wavelengths that are of the order of hundreds of meters.

What can we say about the relation between energy scale and electromagnetic theories? In ray optics as well as classical electrodynamics, the sensitivity in energy of the detector, which can be, for example, the human eye or a photographic plate, is such that a large number of photons have to be captured in order to obtain a measurable signal. However, when using detectors with a much better sensitivity, or, stated differently, to study phenomena that involve small numbers of photons, we have to use a more elaborate theory. This theory is called quantum electrodynamics, and was developed in the beginning of the twentieth century. In contrast with classical electrodynamics, quantum electrodynamics can be applied to a vast range of energy scales. It is the best theory we have, anno 2007, for describing electromagnetic phenomena.

However, for the scales at which it is intended, classical electrodynamics is still the right theory to use. Applying quantum mechanical theory is possible, but often very cumbersome. Moreover, results obtained with the classical theory can still be of value for the quantum theory. An example of this is the calculation of the quantum mechanical phenomenon of the spontaneous emission rate of an atom, for which the classical theory can be used.

The problems in this thesis are all solved within the framework of classical electrodynamics. A short summary of this theory will be given in the next two sections. However, in applying the far field approximation and by calculating spontaneous emission coefficients, we will sometimes touch upon both the older and the newer theory.

1.2 Maxwell's equations and Lorentz's force equation

We assume to have linear, homogeneous, isotropic, non-magnetic and non-dispersive materials, and a charge density ρ and current density $\mathcal{J}$. We can then calculate the resulting electromagnetic fields with Maxwell's equations:

$$\nabla \cdot [\varepsilon \mathcal{E}(\mathbf{r}, t)] = \frac{\rho(\mathbf{r}, t)}{\varepsilon_0}, \tag{1.1a}$$

$$\nabla \cdot \mathcal{H}(\mathbf{r}, t) = 0, \tag{1.1b}$$

$$\nabla \times \mathcal{E}(\mathbf{r}, t) = -\mu_0 \frac{\partial \mathcal{H}(\mathbf{r}, t)}{\partial t}, \tag{1.1c}$$

$$\nabla \times \mathcal{H}(\mathbf{r}, t) = \mathcal{J}(\mathbf{r}, t) + \frac{\partial [\varepsilon_0 \varepsilon \mathcal{E}(\mathbf{r}, t)]}{\partial t}, \tag{1.1d}$$

where $\mathcal{E}$ and $\mathcal{H}$ are the electric and magnetic field, respectively, with space coordinate $\mathbf{r}$ and time coordinate t. Both $\mathcal{E}$ and $\mathcal{H}$ are locally square integrable functions in three-dimensional space. The relative permittivity ε is taken to be real and constant. Furthermore, ε_0 and μ_0 are the electric permittivity and magnetic permeability of empty space, respectively.

For a known charge and current density we use Maxwell's equations to calculate the electric and magnetic field. In turn, the force $\mathbf{F}$ that an electromagnetic field exerts on a charge q that has a velocity $\mathbf{v}$ is given by the Lorentz force:

$$\mathbf{F} = q\mathscr{E} + \mu_0 q \mathbf{v} \times \mathscr{H}. \tag{1.2}$$

According to Newton's law of motion, the force is equal to the rate of change of the momentum, and we can cast this equation into an integral form by integrating all charges in a certain volume:

$$\frac{\mathrm{d}\mathbf{p}_m(t)}{\mathrm{d}t} = \iiint \left[\rho(\mathbf{r},t)\mathscr{E}(\mathbf{r},t) + \mu_0 \mathscr{J}(\mathbf{r},t) \times \mathscr{H}(\mathbf{r},t)\right] \mathrm{d}v, \tag{1.3}$$

with infinitesimal volume element $\mathrm{d}v$. Hence, the quantity $\frac{\mathrm{d}\mathbf{p}_m(t)}{\mathrm{d}t}$ is the increase of mechanical momentum of the charges inside the volume considered.

The above equations together form the heart of classical electrodynamics [1,2]. In the next section, we will derive conservation laws from these equations.

1.3 Conservation laws

The law of conservation of energy is derived as follows. We first take the scalar product of $\mathscr{H}$ with Maxwell's Equation (1.1c) and the scalar product of $\mathscr{E}$ with Equation (1.1d). After subtraction we have:

$$\mathscr{E} \cdot \mathscr{J} = -\frac{\partial}{\partial t}\left(\frac{\varepsilon_0 \varepsilon}{2}\mathscr{E} \cdot \mathscr{E} + \frac{\mu_0}{2}\mathscr{H} \cdot \mathscr{H}\right) - \nabla \cdot (\mathscr{E} \times \mathscr{H}), \tag{1.4}$$

where we have used the vector identity $\mathbf{B} \cdot (\nabla \times \mathbf{A}) - \mathbf{A} \cdot (\nabla \times \mathbf{B}) = \nabla \cdot (\mathbf{A} \times \mathbf{B})$. The quantity $\mathscr{E} \cdot \mathscr{J}$ is the rate of transfer of electromagnetic energy to the charges, per unit of volume. In integral form, with infinitesimal surface element $\mathrm{d}a$, this equation is given by:

$$\iiint \mathscr{E} \cdot \mathscr{J}\, \mathrm{d}v = -\frac{\mathrm{d}}{\mathrm{d}t} \iiint \left(\frac{\varepsilon_0 \varepsilon}{2}\mathscr{E} \cdot \mathscr{E} + \frac{\mu_0}{2}\mathscr{H} \cdot \mathscr{H}\right) \mathrm{d}v - \oiint \mathscr{S} \cdot \mathbf{n}\, \mathrm{d}a, \tag{1.5}$$

where we have used the divergence theorem for the last term, in which $\mathbf{n}$ is the external unit normal of the closed surface that surrounds the integration volume. The quantity $\mathscr{S}$, defined by:

$$\mathscr{S} \equiv \mathscr{E} \times \mathscr{H}, \tag{1.6}$$

is called the Poynting vector. Equation (1.5) is called the Poynting theorem and is the law of conservation of energy. It states that an increase in mechanical energy of the charges in a certain volume, due to interaction with the electric field, is accounted for by a decrease in the electromagnetic energy that is stored in the fields and a flux of energy into the closed surface bounding the volume. More generally, the quantity $\iint \mathscr{S}\cdot\mathbf{n}\,\mathrm{d}a$ is associated with the flux of energy through a surface, in the direction of $\mathbf{n}$, even when this surface is not closed.

For the derivation of the law of conservation of momentum, we start with the Lorentz force Equation (1.2) and we substitute the two Maxwell Equations (1.1a) and (1.1d) to eliminate the charge and current densities. After some manipulations, adding Maxwell's Equation (1.1c) and after adding the term $\mu_0(\nabla\cdot\mathscr{H})\mathscr{H}$ that is equal to zero, we arrive at:

$$\begin{aligned} q\mathscr{E} + \mu_0 q\mathbf{v}\times\mathscr{H} = &-\frac{\mathrm{d}}{\mathrm{d}t}\left(\varepsilon_0\varepsilon\mu_0\mathscr{S}\right) \\ &+ \varepsilon_0\varepsilon\left[(\nabla\cdot\mathscr{E})\mathscr{E} + (\nabla\times\mathscr{E})\times\mathscr{E}\right] + \mu_0\left[(\nabla\cdot\mathscr{H})\mathscr{H} + (\nabla\times\mathscr{H})\times\mathscr{H}\right]. \end{aligned} \tag{1.7}$$

We define the components of the Maxwell stress tensor $\overleftrightarrow{\mathscr{T}}$ by:

$$\mathscr{T}_{\alpha\beta} \equiv \left(\frac{\varepsilon_0\varepsilon}{2}\mathscr{E}\cdot\mathscr{E} + \frac{\mu_0}{2}\mathscr{H}\cdot\mathscr{H}\right)\delta_{\alpha\beta} - \varepsilon_0\varepsilon\,\mathscr{E}_\alpha\mathscr{E}_\beta - \mu_0\,\mathscr{H}_\alpha\mathscr{H}_\beta, \tag{1.8}$$

where the subscripts α and β can be x, y or z and $\delta_{\alpha\beta}$ is the Kronecker delta. Then we can write the previous equation as[1]:

$$q\mathscr{E} + \mu_0 q\mathbf{v}\times\mathscr{H} = -\frac{\mathrm{d}}{\mathrm{d}t}\left(\varepsilon_0\varepsilon\mu_0\mathscr{S}\right) - \nabla\cdot\overleftrightarrow{\mathscr{T}}, \tag{1.9}$$

which is the differential formulation of the law of conservation of momentum. With the divergence theorem, we can cast this into the integral form[2]:

$$\iiint\left(\rho\mathscr{E} + \mu_0\mathscr{J}\times\mathscr{H}\right)\mathrm{d}v = -\frac{\mathrm{d}}{\mathrm{d}t}\iiint \varepsilon_0\varepsilon\mu_0\mathscr{S}\,\mathrm{d}v - \oiint \overleftrightarrow{\mathscr{T}}\cdot\mathbf{n}\,\mathrm{d}a. \tag{1.10}$$

In words, this law of conservation of momentum states that the rate at which momentum is transferred to the charges in a volume is equal to the rate of loss of electromagnetic momentum minus the flux of electromagnetic momentum through the bounding surface out of the volume. Again, the quantity $\iint \overleftrightarrow{\mathscr{T}}\cdot\mathbf{n}\,\mathrm{d}a$ is associated with the flux of momentum through any, not necessarily closed surface.[3]

---

[1] The components of the gradient of a tensor are given by:

$$\left(\nabla\cdot\overleftrightarrow{\mathscr{A}}\right)_\alpha = \sum_\beta \frac{\partial}{\partial\beta}\mathscr{A}_{\alpha\beta}.$$

[2] The components of the dot product of a tensor with a vector are given by:

$$\left(\overleftrightarrow{\mathscr{A}}\cdot\mathbf{b}\right)_\alpha = \sum_\beta \mathscr{A}_{\alpha\beta}\,b_\beta.$$

[3] The Maxwell stress tensor is discontinuous at interfaces between different materials. In applying Equation (1.10), we have to take the limit of $\overleftrightarrow{\mathscr{T}}$ from outside the volume.

The third conservation law that we state here is the law of conservation of angular momentum. It is obtained by forming the cross product of the position vector with the law of conservation of momentum:

$$\mathbf{r}\times\left(q\mathscr{E}+\mu_0 q\,\mathbf{v}\times\mathscr{H}\right)=-\frac{\mathrm{d}}{\mathrm{d}t}\left[\varepsilon_0\varepsilon\mu_0\left(\mathbf{r}\times\mathscr{S}\right)\right]-\mathbf{r}\times\left(\nabla\cdot\overleftrightarrow{\mathscr{T}}\right). \tag{1.11}$$

Due to the symmetry of the Maxwell stress tensor, the term $\mathbf{r}\times\left(\nabla\cdot\overleftrightarrow{\mathscr{T}}\right)$ is equal to $\nabla\cdot\left(\mathbf{r}\times\overleftrightarrow{\mathscr{T}}\right)$[4]. In integral form, after again using the divergence theorem, we find the law of conservation of angular momentum:

$$\iiint\mathbf{r}\times\left(\rho\mathscr{E}+\mu_0\mathscr{J}\times\mathscr{H}\right)\mathrm{d}v=-\frac{\mathrm{d}}{\mathrm{d}t}\iiint\varepsilon_0\varepsilon\mu_0\left(\mathbf{r}\times\mathscr{S}\right)\mathrm{d}v-\oiint\overleftrightarrow{\mathscr{K}}\cdot\mathbf{n}\,\mathrm{d}a, \tag{1.12}$$

with $\overleftrightarrow{\mathscr{K}}$ the angular momentum flux:

$$\overleftrightarrow{\mathscr{K}}=\mathbf{r}\times\overleftrightarrow{\mathscr{T}}. \tag{1.13}$$

Hence, the rate at which angular momentum is transferred to the charges in a volume is equal to the rate of loss of electromagnetic angular momentum minus the flux of electromagnetic angular momentum through the bounding surface out of the volume. Again, the quantity $\iint\overleftrightarrow{\mathscr{K}}\cdot\mathbf{n}\,\mathrm{d}a$ is associated with the flux of angular momentum through any surface, in the direction of the unit normal $\mathbf{n}$.

1.4 Monochromatic fields and pulses

The electric and magnetic fields $\mathscr{E}$ and $\mathscr{H}$ are functions of space coordinate $\mathbf{r}$ and time t. The time dependence can be arbitrary. However, in this thesis we will mainly consider monochromatic or time-harmonic fields. In good approximation, the fields from a continuous laser can be considered time-harmonic. This means that the fields have a fixed positive frequency ω. Instead of working with the real physical quantities, denoted by the calligraphic fonts, we can then work with complex quantities which we denote by the usual fonts. These are related as follows:

$$\mathscr{F}(\mathbf{r},t)=\mathrm{Re}\left[F(\mathbf{r})\,e^{-i\omega t}\right], \tag{1.14}$$

with $\mathscr{F}$ any physical quantity. Furthermore, Re means the real part.

---

[4] The result of the cross product of a vector with a tensor is a tensor, with components:

$$\left(\mathbf{a}\times\overleftrightarrow{\mathscr{B}}\right)_{\alpha\beta}=\sum_{\gamma}\sum_{\delta}\epsilon_{\beta\gamma\delta}\,a_\gamma\,\mathscr{B}_{\alpha\delta},$$

with $\epsilon_{\alpha\beta\gamma}$ the Levi-Civita symbol [2].

Maxwell's equations for time-harmonic fields are given by:

$$\nabla \cdot [\varepsilon_0 \varepsilon \mathbf{E}(\mathbf{r})] = \rho(\mathbf{r}), \tag{1.15a}$$

$$\nabla \cdot \mathbf{H}(\mathbf{r}) = 0, \tag{1.15b}$$

$$\nabla \times \mathbf{E}(\mathbf{r}) = i\omega\mu_0 \mathbf{H}(\mathbf{r}), \tag{1.15c}$$

$$\nabla \times \mathbf{H}(\mathbf{r}) = \mathbf{J}(\mathbf{r}) - i\omega\varepsilon_0\varepsilon \mathbf{E}(\mathbf{r}), \tag{1.15d}$$

where the charge density ρ and the current density $\mathbf{J}$ are also time-harmonic.

The time averages of the conservation laws for time harmonic fields are given by:

$$\tfrac{1}{2}\,\mathrm{Re} \iiint \mathbf{E} \cdot \mathbf{J}^* \,\mathrm{d}v = - \oiint \mathbf{S} \cdot \mathbf{n} \,\mathrm{d}a, \tag{1.16a}$$

$$\tfrac{1}{2}\,\mathrm{Re} \iiint \left(\rho\,\mathbf{E}^* + \mu_0 \mathbf{J} \times \mathbf{H}^*\right) \mathrm{d}v = - \oiint \overleftrightarrow{\mathbf{T}} \cdot \mathbf{n} \,\mathrm{d}a, \tag{1.16b}$$

$$\tfrac{1}{2}\,\mathrm{Re} \iiint \mathbf{r} \times \left(\rho\,\mathbf{E}^* + \mu_0 \mathbf{J} \times \mathbf{H}^*\right) \mathrm{d}v = - \oiint \overleftrightarrow{\mathbf{K}} \cdot \mathbf{n} \,\mathrm{d}a, \tag{1.16c}$$

where the superscript $*$ denotes complex conjugation. The time averages of the energy flux, the components of the momentum flux, and the angular momentum flux are given by:

$$\mathbf{S} = \tfrac{1}{2}\,\mathrm{Re}\left(\mathbf{E} \times \mathbf{H}^*\right), \tag{1.17a}$$

$$T_{\alpha\beta} = \tfrac{1}{2}\,\mathrm{Re}\left[\left(\frac{\varepsilon_0\varepsilon}{2}\,|\mathbf{E}|^2 + \frac{\mu_0}{2}\,|\mathbf{H}|^2\right)\delta_{\alpha\beta} - \varepsilon_0\varepsilon\, E_\alpha E_\beta^* - \mu_0\, H_\alpha H_\beta^*\right], \tag{1.17b}$$

$$\overleftrightarrow{\mathbf{K}} = \mathbf{r} \times \overleftrightarrow{\mathbf{T}}. \tag{1.17c}$$

It should be noted that the relative permittivity ε is assumed to be real.

When we solve a certain scattering problem for a range of frequencies, we can add the fields to form the solution of a problem that is not time-harmonic. We will do this in Chapter 3 for a terahertz pulse. If, for example, the x-component of the incident electric field of the terahertz pulse is $E^i(t)$, which is measured in an experiment, then the dimensionless spectrum $A(\omega)$ of this pulse is:

$$A(\omega) = A_0 \int E^i(t) e^{-i\omega t} \mathrm{d}t, \tag{1.18}$$

where $A_0 \equiv 1\mathrm{m/Vs}$ is a normalization constant. Denoting the calculated diffracted (complex) field for an incident monochromatic plane wave with frequency ω and unit amplitude by $\hat{\mathbf{E}}(\mathbf{r}, \omega)$, we have for the scattered field of the pulse:

$$\mathbf{E}(\mathbf{r}, t) = \tfrac{1}{2\pi} \int A(\omega)\, \hat{\mathbf{E}}(\mathbf{r}, \omega)\, e^{i\omega t}\, \mathrm{d}\omega. \tag{1.19}$$

The method of decomposing a time signal into its constituent frequencies, calculating the solution of the diffraction problem for each frequency separately, and, finally, adding the solutions coherently, is basic Fourier theory.

1.5 Helmholtz equations

By taking the cross product of Maxwell's Equations (1.15c) and (1.15d), respectively, and by applying the vector identity[5] $\nabla \times (\nabla \times \mathbf{F}) = \nabla(\nabla \cdot \mathbf{F}) - \Delta \mathbf{F}$, we obtain the inhomogeneous Helmholtz equations for the cartesian components of the electric and magnetic field:

$$\left(\Delta + \omega^2 \mu_0 \varepsilon_0 \varepsilon\right) \mathbf{E} = -i\omega\mu_0 \mathbf{J} + \tfrac{1}{\varepsilon_0 \varepsilon} \nabla \rho, \tag{1.20a}$$

$$\left(\Delta + \omega^2 \mu_0 \varepsilon_0 \varepsilon\right) \mathbf{H} = -\nabla \times \mathbf{J}, \tag{1.20b}$$

with Δ the Laplace operator.

These Helmholtz equations show that every cartesian component of the electromagnetic field satisfies the scalar Helmholtz equation. However, even though satisfying the Helmholtz equation is a *necessary* condition for any electromagnetic field, it is not *sufficient*. In the derivation of the Helmholtz equation for the electric field, we used Maxwell's equation for the divergence of the electric field. For the Helmholtz equation for the magnetic field, similarly, we used the condition that the magnetic field must be divergence-free. However, when using only the above Helmholtz equations to derive solutions of some kind of electromagnetic problem, we can not be sure that these solutions satisfy Maxwell's Equations (1.15a) and (1.15b). This must be verified separately.

For regions without currents and charges, the Helmholtz equations reduce to the homogeneous wave equation that holds for every component of the electromagnetic field U:

$$\left(\Delta + \omega^2 \mu_0 \varepsilon_0 \varepsilon\right) U = 0. \tag{1.21}$$

Hence, in source-free regions, the electromagnetic field consists of waves that travel with velocity c/n with c the speed in vacuum and n the index of refraction:

$$c = (\mu_0 \varepsilon_0)^{-1/2}, \tag{1.22}$$

$$n = \sqrt{\varepsilon}. \tag{1.23}$$

The real wave number k is equal to $\omega\sqrt{\mu_0 \varepsilon_0 \varepsilon}$, which is the amplitude of the wave vector $\mathbf{k}$ that gives the direction of propagation of the wave.

In this thesis, the main direction of propagation, or the optical axis, is always the z-axis. We can then have waves that are either propagating or evanescent in the z-direction. For a wave that is propagating in the z-direction, the z-component of the wave vector k_z is purely real, whereas for an evanescent wave, k_z is purely imaginary:

$$k_z = \pm\sqrt{k^2 - k_x^2 - k_y^2}, \qquad \text{if } k_x^2 + k_y^2 \le k^2, \tag{1.24a}$$

$$k_z = \pm i\sqrt{k_x^2 + k_y^2 - k^2}, \qquad \text{if } k_x^2 + k_y^2 > k^2, \tag{1.24b}$$

---

[5] This identity is only valid for cartesian coordinate systems.

where ± denotes the direction of propagation (+ for a wave that is propagating or evanescent in the positive z-direction) and i is the imaginary unit.[6] The wavelength λ of a wave with wave vector k is given by $\frac{2\pi}{k}$. The frequency f (measured in Hertz) is related to the radial frequency ω (measured in radians per second) by $\omega = 2\pi f$.

The range of frequencies in the electromagnetic spectrum ranges from waves with wavelengths smaller than a picometer for gamma rays, to wavelengths of hundreds of meters for radio waves. Central in the electromagnetic spectrum is the visible region, between 400 and 700 nanometers. A region that has gained a lot of attention recently is the terahertz region with frequencies around one terahertz and wavelengths around 300 micron. In Chapter 3 we will compare measurements done in the terahertz range with simulations.

1.6 On material parameters and boundary conditions

As we saw in the previous section, the index of refraction for a dielectric is given by $n = \sqrt{\varepsilon}$, with ε the relative permitivitty. Throughout this thesis, all dielectrics are lossless and homogeneous, so that ε is a real scalar.

A metal differs from a dielectric mainly in the presence of free electrons. When an electric field is applied to a metal, the free electrons are accelerated by the field according to the Lorentz force law (1.2). The collisions of electrons with the ion cores of the metal and with other electrons cause a frictional force. The motion of a free electron is then governed by the following differential equation:

$$q\mathcal{E} = m\left(\frac{\mathrm{d}^2\mathbf{x}}{\mathrm{d}t^2} + \gamma\frac{\mathrm{d}\mathbf{x}}{\mathrm{d}t}\right), \tag{1.25}$$

with q the charge of an electron, m its mass and $\gamma > 0$ the damping constant. If we now assume a time-harmonic field, we obtain:

$$\mathbf{x}(t) = \frac{-q}{m\omega\left(\omega + i\gamma\right)}\mathbf{E}(t). \tag{1.26}$$

If the metal contains N free electrons per unit volume, then these form a current density:

$$\mathbf{J}(t) = Nq\frac{\mathrm{d}\mathbf{x}}{\mathrm{d}t} = \frac{q^2 N}{m\left(\gamma - i\omega\right)}\mathbf{E}(t). \tag{1.27}$$

Inserting Ohm's law $\mathbf{J} = \sigma\mathbf{E}$, we find for the conductivity:

$$\sigma = \frac{q^2 N}{m\left(\gamma - i\omega\right)}. \tag{1.28}$$

---

[6] Here and henceforth the square root of a complex number z is defined such that for real $z > 0$ we have $\sqrt{z} > 0$ and $\sqrt{-z} = +i\sqrt{z}$, with the branch cut along the negative real axis.

With the plasma frequency:

$$\omega_p = \sqrt{\frac{Nq^2}{\varepsilon_0 m}}, \tag{1.29}$$

which is the resonance frequency of the free electrons in the metal, and with the damping frequency:

$$\omega_\tau = \gamma, \tag{1.30}$$

which is the collision frequency of the free electrons, we have for the conductivity:

$$\sigma = \varepsilon_0 \frac{\omega_p^2}{\omega_\tau - i\omega}. \tag{1.31}$$

Values of the plasma frequency and the damping frequency for various materials can be found in, for example, reference [3].

If we substitute Ohm's law in Maxwell's Equation (1.15d), take the divergence and substitute Maxwell's Equation (1.15a), we find for the charge density:

$$\left(\frac{\sigma}{\varepsilon_0\varepsilon} - i\omega\right)\rho(t) = 0, \tag{1.32}$$

so that it is clear that for a time-harmonic field the charge density inside a metal must vanish. Stated differently, the charge is concentrated on the surface of the metal. We can then write the Helmholtz equation for the electromagnetic field as:

$$\left(\Delta + \omega^2\mu_0\varepsilon_0\varepsilon + i\omega\mu_0\sigma\right)\mathbf{E} = 0, \tag{1.33a}$$

$$\left(\Delta + \omega^2\mu_0\varepsilon_0\varepsilon + i\omega\mu_0\sigma\right)\mathbf{H} = 0. \tag{1.33b}$$

Hence, for a metal, we can introduce a complex index of refraction, of which the square is given by:

$$\begin{aligned} n^2 &= \varepsilon + \frac{i\sigma}{\omega\varepsilon_0}, \\ &= \varepsilon + \frac{i\omega_p^2}{\omega(\omega_\tau - i\omega)}, \end{aligned} \tag{1.34}$$

where in the second line, we have used Equation (1.31). The relative permittivity of a metal can usually be neglected, such that we obtain:

$$n^2 = \frac{-\omega_p^2}{\omega(\omega + i\omega_\tau)}. \tag{1.35}$$

This is the Drude model for the refractive index of a metal. Within a metal with a large conductivity, a plane wave with wave number $k_0 n$ with k_0 the wave number in vacuum, only penetrates a distance that is inversely proportional to the imaginary part of the index of refraction. Hence, for a conductivity that approaches infinity, or, differently stated, for a plasma frequency much larger than the frequency of the wave, the penetration depth goes to zero. This is the behaviour of a perfect conductor, of which the conductivity is assumed to be infinite.

It is only at the interface between optically different media that scattering or diffraction of electromagnetic radiation can take place. If we calculate a diffraction problem by solving the Helmholtz equation in each medium separately, we have to match the fields at the interface between the materials. Therefore we need boundary conditions that relate the fields. These can easily be derived from Maxwell's equations, by applying the integral versions of Maxwell's equations to the area of a Stokesian loop. See reference [1] for a detailed derivation. Here we only state the results.

If **n** is the normal of the interface between two media, we have the following relations for the tangential field components:

$$(\mathbf{E}_1 - \mathbf{E}_2) \times \mathbf{n} = 0, \tag{1.36a}$$

$$(\mathbf{H}_1 - \mathbf{H}_2) \times \mathbf{n} = \mathbf{J}^{\mathrm{surf}}, \tag{1.36b}$$

where the subscripts 1 and 2 denote the two media and with $\mathbf{J}^{\mathrm{surf}}$ the surface current density. At the interface between a dielectric and a perfect conductor, we find that the total tangential electric field vanishes and the total tangential magnetic field is equal to the surface current density.

These boundary conditions are local boundary conditions. There is, however, another important boundary condition that applies to the electromagnetic field far away from the scattering object. It is the Sommerfeld radiation condition which states that the energy scattered from an object must be radiated to infinity, away from the object [4]. Stated differently: the scattering objects can be considered energy sources, but not energy sinks.

1.7 Electromagnetic surface waves

Along the interface between a dielectric and a metal, Maxwell's equations allow for a special electromagnetic field, which can be interpreted as a surface wave: an electromagnetic wave propagating along the interface. For optical frequencies, these electromagnetic surface waves are usually called plasmons or surface plasmon polaritons. In the case of a flat interface, we can easily derive the dispersion equation.

Let the half space $z > 0$ be filled with medium 1, having index of refraction n_1. The half space $z < 0$ has index of refraction n_2. Without loss of generality, we will consider a surface wave propagating in the positive x-direction. Our problem is then reduced to a two-dimensional problem. We seek a time-harmonic solution of Maxwell's equations of the following form:

$$U(x,z) = \begin{cases} A_1 e^{ik_{\mathrm{sw}}x - \kappa_1 z}, & \text{for } z > 0, \\ A_2 e^{ik_{\mathrm{sw}}x + \kappa_2 z}, & \text{for } z < 0, \end{cases} \tag{1.37}$$

where U is any component of the electromagnetic field and A_1, A_2 are the complex amplitudes. We require the real parts of κ_1 and κ_2 to be positive, in order to prevent the solution from growing exponentially away from the interface. We assume media 1 and 2 to be non-magnetic and isotropic. Their indices of refraction may be complex. In both media, the components of the electromagnetic field have to satisfy the scalar wave Equation (1.21), such that we find the following relation for the x-component of the wave number of the surface wave:

$$k_{\mathrm{sw}}^2 = \omega^2 \mu_0 \varepsilon_0 n_1^2 + \kappa_1^2 = \omega^2 \mu_0 \varepsilon_0 n_2^2 + \kappa_2^2. \tag{1.38}$$

As the electromagnetic field of the surface wave is transverse, we will separately consider the two independent polarizations S and P. S-polarization means that the electric field only has a y-component and P-polarization means that the magnetic field only has a y-component. In this thesis, we will also use TE and TM, respectively, to distinguish between both polarizations.

When we have S-polarization, $U = E_y$ should satisfy the following boundary conditions for $z = 0$:

$$E_{y1} = E_{y2}, \tag{1.39a}$$

$$\frac{\partial E_{y1}}{\partial z} = \frac{\partial E_{y2}}{\partial z}, \tag{1.39b}$$

where the second condition follows from Maxwell's Equation (1.15c) and the continuity of H_x. From these boundary conditions it follows that $A_1 = A_2$ and $-\kappa_1 = \kappa_2$. However, this latter equality can not be satisfied simultaneously with the condition for k_{sw} when the two media have a different index of refraction, as we assumed. Hence, a surface wave can not exist for S-polarization. Generally speaking, a surface wave can not exist if the electric field is parallel to the surface.

Let us turn to P-polarization. Then, we choose $U = H_y$ and we have the following boundary conditions for $z = 0$:

$$H_{y1} = H_{y2}, \tag{1.40a}$$

$$\frac{1}{n_1^2}\frac{\partial H_{y1}}{\partial z} = \frac{1}{n_2^2}\frac{\partial H_{y2}}{\partial z}. \tag{1.40b}$$

The second condition follows from substituting Ohm's law $\mathbf{J} = \sigma\mathbf{E}$ in Maxwell's Equation (1.15d), using the complex index of refraction (1.34) and the continuity of E_x. From these boundary conditions it follows that $A_1 = A_2$ and $-\frac{\kappa_1}{n_1^2} = \frac{\kappa_2}{n_2^2}$.

These relations can be satisfied simultaneously with Equation (1.38) provided that the following condition is met:

$$k_{\mathrm{sw}}^2 = \omega^2 \mu_0 \varepsilon_0 \frac{n_1^2 n_2^2}{n_1^2 + n_2^2}. \tag{1.41}$$

This is the dispersion equation for electromagnetic surface waves [5].

Now, suppose medium 1 is vacuum and medium 2 is aluminum. Let us consider two cases: the first with a frequency in the visible part of the electromagnetic spectrum and the second with a frequency in the terahertz region. The indices of refraction of aluminum for these wavelengths are:

$$n_{\mathrm{Al,650nm}} = 1.47 + 7.79i, \tag{1.42}$$

$$n_{\mathrm{Al,300}\mu\mathrm{m}} = 552 + 581i, \tag{1.43}$$

For a wavelength of 650 nm the index of refraction was taken from reference [6]. For 300 μm we used Equation (1.35) and reference [7] for the values for the plasma frequency and the damping frequency. For the wave number of the surface wave we then find:

$$k_{\mathrm{sw,\ Al,650nm}} = k_0(1.008 + 0.003i), \tag{1.44}$$

$$k_{\mathrm{sw,\ Al,300}\mu\mathrm{m}} = k_0(1.00000004 + 0.0000008i), \tag{1.45}$$

with k_0 the corresponding wave number in vacuum. We see that the real part of the wave number is slightly larger than the wave number in vacuum. This is the case for most dielectric metal interfaces. Hence, a propagating wave that is incident on the interface, can not excite the surface wave. However, for evanescent waves, the component of the wave vector that is parallel to the interface can be larger than the wave number and, in this way, a surface wave can be excited. In general, diffraction from sub-wavelength structures leads to evanescent waves and as a consequence, in the case of P-polarization, to surface waves.

The penetration depth of the surface wave in both media is given by κ_1^{-1} and κ_2^{-1}. For a wavelength of 650 nm, the penetration depth in the vacuum is 829 nm and the penetration depth in the aluminum is 13.2 nm, so the wave is really tied to the surface. For a wavelength of 300 μm, the penetration depth in the vacuum is 5.28 cm and the penetration depth in the aluminum is 82.2 nm. Hence, the terahertz wave stretches approximately 200 wavelengths into the vacuum whereas it only penetrates into the metal over a distance that is a factor 4000 smaller than the wavelength.

If the metal is a perfect conductor, the derivation of the dispersion relation (1.41) is still valid. The wave number of the surface wave is then just the wave vector of the light. The penetration depth inside the metal is zero and the charges inside the metal oscillate only in the plane of the interface between the metal and the dielectric. In the half space above the metal the electromagnetic surface wave then has a constant field strength.

In the literature, it is often stated that perfect metals do not support surface plasmons. We believe that the expression *surface plasmon* (or *surface plasmon polariton*) is confusing. The ending -*on* suggests a sort of localization. We saw in the two examples that the extent to which the surface wave is bound to the interface is determined by the index of refraction. The existence and the physical nature of the phenomenon, however, are the same for both a conductor with finite conductivity and an idealized perfect conductor. The only difference is the finite decay length and absorption caused by the finite conductivity.

1.8 A short history of electromagnetic scattering problems

Electromagnetic scattering problems deal with the diffraction of electromagnetic radiation by objects or apertures.[7] The effects of diffraction are mostly noticeable when the wavelength of the radiation is of the same order of magnitude as the feature sizes of the diffracting objects or apertures. As discussed in the first section, classical electrodynamics is the appropriate theory to describe electromagnetic scattering problems.

For a rigorous solution of a scattering problem, one has to solve, for a given incident field, the Maxwell equations, including the appropriate boundary conditions for the total field at the boundaries of the scattering bodies and taking account of the Sommerfeld radiation condition for the scattered field. However, only for relatively few diffracting objects and apertures it is possible to give an analytical solution.

The oldest rigorous solution is the one for the diffraction by an infinitely thin, perfectly conducting half plane, derived by Sommerfeld in 1896.[8] Its solution is written in terms of Fresnel integrals. Another famous solution is the diffraction from a sphere by Mie in 1908. A notable aspect of this theory is that it is valid not only for a perfectly conducting sphere, but also for spheres with finite conductivity and a finite dielectric constant. A description of this diffraction problem and its solution is given in reference [4]. The third rigorous solution that we mention here is the scattering from a perfectly conducting, infinitely thin circular disc, by Meixner

---

[7] The electromagnetic radiation is usually assumed to originate from an unspecified source at infinity, such that the field that is incident on the scattering object can be expanded in plane waves. If, however, the radiating source is located near the scattering object, the term radiation problem is often used instead of scattering problem. In this thesis, either type of incident field is treated. We will nevertheless use the term scattering problem for both cases.

[8] For a comprehensive review, see references [8] and [9].

and Andrejewski in 1950 [10]. Because of the electromagnetic analogue of Babinet's principle [8], this solution automatically yields the solution of the scattering from a perfectly conducting, infinitely thin screen with a circular aperture.

The method for solving these diffraction problems is as follows. A suitable orthogonal coordinate system is chosen, such that the surface of the diffracting object is perpendicular to one of the coordinates. In this way, boundary conditions are easily prescribed. The solution is then expanded into an infinite series of eigenfunctions that are the solutions of Maxwell's equations separated in these coordinates.

For the case of the half plane, the separation can be done in semi-parabolical coordinates. For the case of the sphere, spherical coordinates are used and vector spherical wave functions are the solutions of the separated wave function. Finally, for the infinitely thin disc, the separation into oblate or prolate spheroidal coordinates leads to spheroidal wave functions as eigenfunctions.

For most diffraction problems, however, it is very hard to find a suitable set of coordinates, let alone to find coordinates for which the vector Helmholtz equation separates. A way to solve this problem is to use distinct sets of eigenfunctions for distinct regions in space. Then, of course, an additional problem is created in that the set of expansion coefficients for the eigenfunctions in one region must somehow be related to the set of expansion coefficients for the eigenfunctions in another region. This leads to overlap integrals that relate the eigenfunctions in one region to the eigenfunctions in another region.

Roberts, in 1987, used this method to solve the problem of the diffraction by a circular aperture in a perfectly conducting layer with finite thickness [11]. The electric and magnetic fields within the aperture are expanded into circular waveguide modes, and above and below the layer, the fields are expanded into plane waves.

The method employed in this thesis resembles the one of Roberts. The main difference is that here the perfectly conducting layer is not restricted to contain only a single hole, but can have a finite number as well as an infinite number of holes. The occurrence of pits, with a depth that is smaller than the thickness of the metal layer, is also possible. Furthermore, we also consider the radiation problem, where a dipole source is placed near the layer or inside a pit or hole. In the next section, we will give the details of the scattering problem under consideration.

1.9 This thesis

In this section, we will define the scattering problems that are studied in this thesis. First, we will specify the geometry of the scattering objects and the sources of electromagnetic radiation. Then we will briefly outline the analytical approach that is used, followed by some words on the organisation of this thesis.

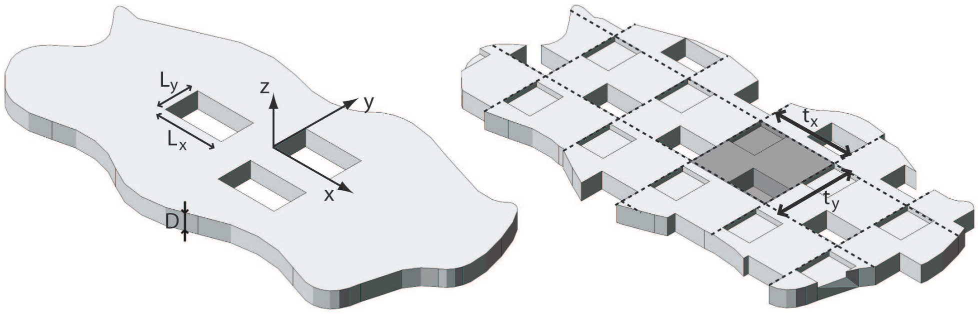

Figure 1.1: Scattering geometries considered in this thesis. All pits and holes are rectangular. The conducting layer has a finite thickness D. Left: a finite number of pits or holes. Right: a periodic array of pits and holes. The shaded area denotes a unit cell.

1.9.1 Scattering objects and incident field

The geometry of our scattering problem is as follows. Let (x, y, z) be a rectangular cartesian coordinate system. Perpendicular to the z-axis we have a perfectly conducting layer with finite thickness D. In this layer we either have a finite number of rectangular holes and pits or we have a periodic setup, which consists of a two-dimensional array of holes and pits. See Figure 1.1. A hole is a rectangular cylinder that is open on both sides and is as long as the thickness of the layer; a pit has an open end at one side, either at $z = D/2$ or at $z = -D/2$, and a depth $d_p < D$. The sub- or superscript p denotes the index of the pit or hole. The lengths in the x- and y-direction are L_x^p and L_y^p, respectively. The cross-section of a hole or a pit p is given by $\Omega_p = \left\{ (x, y) \,\middle|\, x_0^p < x < x_0^p + L_x^p,\ y_0^p < y < y_0^p + L_y^p \right\}$. For the periodic setup, we have a two-dimensional rectangular lattice with periodicity t_x in the x-direction and t_y in the y-direction.

The halfspaces $z > D/2$ and $z < -D/2$ are filled with homogeneous dielectrics with index of refraction n_u and n_ℓ, respectively. Every hole and pit is filled with a homogeneous dielectric with index of refraction n_p.[9] The corresponding relative permeabilities are $\varepsilon_u = n_u^2$, $\varepsilon_\ell = n_\ell^2$ and $\varepsilon_p = n_p^2$. The magnetic permeability is μ_0 everywhere.

The electromagnetic field that is incident on the scattering structure can be a monochromatic plane wave originating from infinity, either from above and/or below the conducting layer. A more complex field such as a spot is also possible. The incident field can also originate from one or more sources near the conducting layer or inside a pit or hole (see Figure 1.2 on the next page). The wavelength of the field in free space is given by λ. The local wavelengths are $\lambda_u = \lambda/n_u$, $\lambda_\ell =$

---

[9] Although in this thesis n_p is always real, in principle, it can be complex.

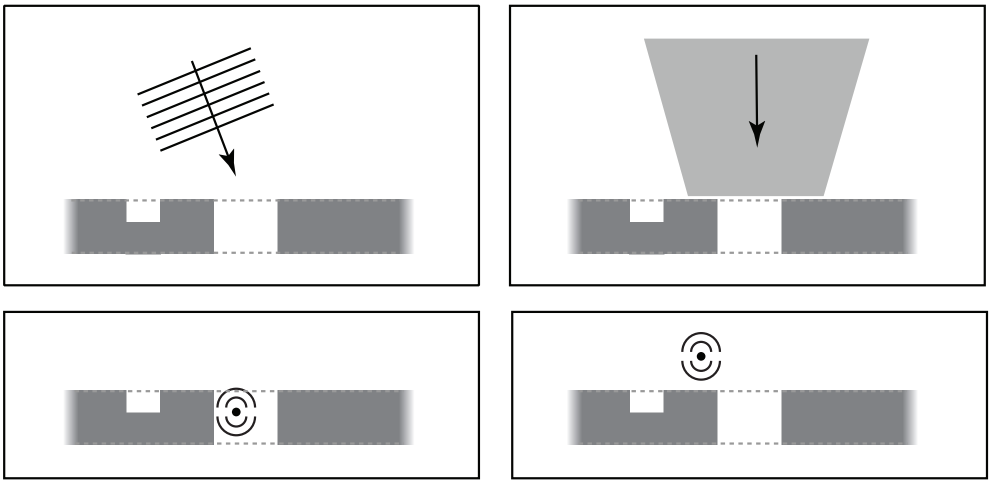

Figure 1.2: The source of electromagnetic radiation can be a plane wave (upper left), a integral or sum of plane waves such as a spot (upper right), a dipole inside a hole or pit (lower left) or a dipole above or below the perfectly conducting layer.

λ/n_ℓ and $\lambda_p = \lambda/n_p$. The corresponding wave vectors are $k_u = 2\pi/\lambda_u$, $k_\ell = 2\pi/\lambda_\ell$ and $k_p = 2\pi/\lambda_p$. As stated before, the harmonic time dependence of the electromagnetic field is given by the factor $\exp(-i\omega t)$, with $\omega > 0$, and will be omitted throughout this thesis.

1.9.2 The analytical approach

We use a mode expansion method to calculate the diffraction problem that was introduced in the previous section. The electric and magnetic fields within the rectangular pits and holes are expanded into an infinite sum of waveguide modes. These waveguide modes are the eigenfunctions of the Helmholtz equation for the pits and holes at the given frequency. A waveguide mode is either propagating or evanescent in the z-direction, depending on whether the z-component of the wave vector of the mode is real or imaginary.[10] All waveguide modes together form a complete set. Above and below the layer, the eigenfunctions are simply plane waves and, thus, the fields are expanded into a continuum of propagating or evanescent plane waves.

Once we have these expansions for the fields, we need to determine the expansion coefficients. This is done by applying the appropriate boundary conditions at the interfaces $z = D/2$ and $z = -D/2$. By using the orthonormality of the two sets of eigenfunctions, we derive a system of linear equations in which the expansion

---

[10] In the case that the pit or hole is filled with an absorbing dielectric (complex n_p), the so-called propagating modes are damped in the z-direction, but much less so than the so-called evanescent modes.

coefficients are the unknowns. It will be shown that the coefficients of the plane waves can be eliminated, such that a relatively small system of equations remains.

So far, although we have to truncate the expansions for numerical implementation, the approach to describe the scattering problem is analytical. However, in the system of equations, the elements of the coefficient matrix contain so-called interaction integrals. Physically speaking, these integrals describe the interaction of one waveguide mode, via the scattered field above or below the layer with another waveguide mode. Because the integrands of the interaction integrals contain rapidly oscillating factors as well as singular factors due to the presence of surface waves, they should be calculated with care. To our knowledge, it is not possible to calculate these integrals analytically. Nevertheless, the expansion of the electromagnetic field in eigenfunctions allows us to get a firm grip on the physics of our scattering problem.

1.9.3 Organisation of this thesis

This thesis is organised as follows. In the next chapter, we will treat the case of a non-periodic setup, with the incident field originating from infinity. Chapter 3, 4 and 5 all deal with results based on this theory. Chapter 3 compares calculations with measurements on terahertz pulses. Chapter 4 deals with the transmission of energy through multiple holes and Chapter 5 deals with the transmission of angular momentum through a single hole. In Chapter 6 the theory for the periodic setup is treated. This part of the theory is not implemented in a computer code. The subject of Chapter 7 is the theory for a dipole source near or inside a pit or hole, for a non-periodic setup. In Chapter 8 this theory is applied to spontaneous emission calculations. Finally, the conclusions can be found in Chapter 9.

Chapter 2

Mode expansion theory for multiple holes and pits

In this chapter, we will introduce the mode expansion theory that is used to solve the diffraction problem of multiple rectangular holes and pits in a perfectly conducting layer with finite thickness. This chapter is organized as follows. In Sections 2.1 and 2.2, we will describe the field inside the holes, and above and below the layer by mode expansions. Section 2.3 is about matching these expressions to derive the system of equations that needs to be solved. Section 2.4 is devoted to the possible singular behaviour of the electromagnetic fields near a rim of a hole or pit. In Section 2.5 we will briefly treat the main numerical considerations.

2.1 Mode expansion inside the holes and pits

In each pit or hole, the electromagnetic field is expanded in a set of propagating or evanescent modes. These modes are characterized by the geometry of the pit or hole they live in. See Figure 1.1 on page 15. Furthermore, the modes are characterized by their polarization, by their spatial frequency and by their direction of propagation.

Solving Maxwell's equations inside the pits and holes means finding solutions of the wave equation (1.21) for every cartesian component of the electromagnetic field. As stated in Section 1.6, the boundary conditions imply that, at a perfect conductor, the tangential electric field as well as the normal magnetic field vanish. We then find solutions that are called waveguide modes. These are propagating or evanescent in the z-direction:

$$\begin{bmatrix} \mathbf{E}_{\boldsymbol{\alpha}}(\mathbf{r}) \\ \mathbf{H}_{\boldsymbol{\alpha}}(\mathbf{r}) \end{bmatrix} = \begin{bmatrix} \mathbf{E}_{\boldsymbol{\alpha}}(x,y) \\ \mathbf{H}_{\boldsymbol{\alpha}}(x,y) \end{bmatrix} e^{\pm i\gamma_z z}, \tag{2.1}$$

with propagation constant γ_z given by[1]:

$$\gamma_z = \sqrt{k_p^2 - \gamma_x^2 - \gamma_y^2}, \tag{2.2}$$

where γ_x and γ_y determine the spatial behavior in x and y-direction:

$$\gamma_x = \frac{m_x \pi}{L_x^p},\ \gamma_y = \frac{m_y \pi}{L_y^p}, \tag{2.3}$$

with m_x and m_y integers. The bold subscript $\boldsymbol{\alpha} = (\alpha_1, \alpha_2, \alpha_3, \alpha_4)$ is a multi-index that describes four discrete variables: α_1 (or p) denotes the pit number, α_2 indicates the polarization (TE or TM), α_3 is determined by m_x and m_y and α_4 specifies whether the mode is traveling upwards or downwards. Evanescent waveguide modes (for which γ_z is purely imaginary) are below cutoff. In the accidental case that the widths of the hole or pit is such that a waveguide mode has a propagation constant equal to zero, this mode is said to be at cutoff.

Because the matching conditions at the interfaces $z = \pm D/2$ only involve the x- and y-component of the fields, it is convenient to introduce the following notation:

$$\mathbf{e}(x,y,z) \equiv \hat{\boldsymbol{\imath}}_z \times \left[\hat{\boldsymbol{\imath}}_z \times \mathbf{E}(x,y,z)\right] = \begin{pmatrix} -E_x \\ -E_y \\ 0 \end{pmatrix}, \tag{2.4a}$$

$$\mathbf{h}(x,y,z) \equiv \hat{\boldsymbol{\imath}}_z \times \mathbf{H}(x,y,z) = \begin{pmatrix} -H_y \\ H_x \\ 0 \end{pmatrix}, \tag{2.4b}$$

with $\hat{\boldsymbol{\imath}}_z$ the unit vector in the z-direction. In this way, the lower case $\mathbf{e}$ and $\mathbf{h}$ are the rotated transverse components of the electric and magnetic field. Furthermore, we split the transverse components of the modes into a real part that depends on x and y and a complex part that depends on z:

$$\mathbf{e}_{\boldsymbol{\alpha}}(x,y,z) = \boldsymbol{v}_{\boldsymbol{\alpha}}(x,y)\,\eta_{\boldsymbol{\alpha}}(z), \tag{2.5a}$$

$$\mathbf{h}_{\boldsymbol{\alpha}}(x,y,z) = \boldsymbol{v}_{\boldsymbol{\alpha}}(x,y)\,\zeta_{\boldsymbol{\alpha}}(z), \tag{2.5b}$$

where the subscript $\bar{\boldsymbol{\alpha}} = (\alpha_1, \alpha_2, \alpha_3)$ does not contain the index α_4 and, hence, the transverse vector field $\boldsymbol{v}_{\bar{\boldsymbol{\alpha}}}$ does not depend on the direction of propagation of the mode.

We normalize the modes by [1]:

$$\left\langle \boldsymbol{v}_{\bar{\boldsymbol{\alpha}}} \middle| \boldsymbol{v}_{\bar{\boldsymbol{\alpha}}} \right\rangle_{\Omega_p} \equiv \iint\limits_{\Omega_p} \left[v_{\bar{\boldsymbol{\alpha}},x}(x,y)\, v_{\bar{\boldsymbol{\alpha}},x}(x,y)^* + v_{\bar{\boldsymbol{\alpha}},y}(x,y)\, v_{\bar{\boldsymbol{\alpha}},y}(x,y)^* \right] \mathrm{d}x\, \mathrm{d}y = 1, \tag{2.6}$$

---

[1] The square root of a complex number z is defined such that for real $z > 0$ we have $\sqrt{z} > 0$ and $\sqrt{-z} = +i\sqrt{z}$, with the branch cut along the negative real axis.

with Ω_p the area of the pit or hole and the superscript $*$ denotes complex conjugation.[2] Furthermore, the modes are orthogonal such that for different modes $\bar{\boldsymbol{\alpha}}$ and $\bar{\boldsymbol{\alpha}}'$:

$$\left\langle \boldsymbol{v}_{\bar{\boldsymbol{\alpha}}} \middle| \boldsymbol{v}_{\bar{\boldsymbol{\alpha}}'} \right\rangle_{\Omega_{p'}} = 0, \qquad \text{if } \bar{\boldsymbol{\alpha}} \neq \bar{\boldsymbol{\alpha}}'. \tag{2.7}$$

Note that the time averaged Poynting vector in the z-direction of a mode is given by:

$$S_{\boldsymbol{\alpha},z} = \frac{1}{2}\,\mathrm{Re}\left(E_{\boldsymbol{\alpha},x}\,H^*_{\boldsymbol{\alpha},y} - E_{\boldsymbol{\alpha},y}\,H^*_{\boldsymbol{\alpha},x}\right) = \frac{1}{2}\,\mathrm{Re}\left(\eta_{\boldsymbol{\alpha}}\,\zeta^*_{\boldsymbol{\alpha}}\right)\left(\boldsymbol{v}_{\bar{\boldsymbol{\alpha}},x}\,\boldsymbol{v}^*_{\bar{\boldsymbol{\alpha}},x} + \boldsymbol{v}_{\bar{\boldsymbol{\alpha}},y}\,\boldsymbol{v}^*_{\bar{\boldsymbol{\alpha}},y}\right), \tag{2.8}$$

and, hence, the scalar product $\langle \boldsymbol{v}_{\bar{\boldsymbol{\alpha}}} | \boldsymbol{v}_{\bar{\boldsymbol{\alpha}}} \rangle_{\Omega_p}$ of a mode $\bar{\boldsymbol{\alpha}}$ with itself is proportional to the flow of energy of this mode through a plane of constant z.

We have now introduced the necessary notation for the waveguide mode functions $(\mathbf{E}_{\boldsymbol{\alpha}}, \mathbf{H}_{\boldsymbol{\alpha}})$. A complete listing of all functions is given below, but first we make the following important remark. The set of waveguide modes is complete in the following sense: any time harmonic electromagnetic field with frequency ω satisfying the source-free Maxwell equations inside the holes and pits can be expressed as a linear combination of these mode functions. Hence, for z in between $D/2$ and $-D/2$, we have:

$$\mathbf{E}^{\mathrm{pit}}(\mathbf{r}) = \sum_{\boldsymbol{\alpha}} a_{\boldsymbol{\alpha}}\,\mathbf{E}_{\boldsymbol{\alpha}}(\mathbf{r}), \tag{2.9a}$$

$$\mathbf{H}^{\mathrm{pit}}(\mathbf{r}) = \sum_{\boldsymbol{\alpha}} a_{\boldsymbol{\alpha}}\,\mathbf{H}_{\boldsymbol{\alpha}}(\mathbf{r}), \tag{2.9b}$$

for some expansion coefficients $a_{\boldsymbol{\alpha}}$ that will be determined by matching the field inside the holes and pits to the field above and below the conducting layer.

2.1.1 Listing of waveguide mode functions

With:

$$\Gamma_{\boldsymbol{\alpha}} = \sqrt{\gamma_x^2 + \gamma_y^2}, \tag{2.10}$$

and

$$\Lambda_{\boldsymbol{\alpha}} = \begin{cases} 2\left(L_x^p L_y^p\right)^{-1/2}, & \text{if } m_x \neq 0 \text{ and } m_y \neq 0, \\ \sqrt{2}\left(L_x^p L_y^p\right)^{-1/2}, & \text{if } m_x = 0 \text{ or } m_y = 0, \end{cases} \tag{2.11}$$

we first define the following auxiliary functions:

$$\boldsymbol{v}_{\bar{\boldsymbol{\alpha}}}(\bar{x}_p, \bar{y}_p) = \begin{cases} \dfrac{\Lambda_{\boldsymbol{\alpha}}}{\Gamma_{\boldsymbol{\alpha}}}\,\Pi(\bar{x}_p, \bar{y}_p) \begin{bmatrix} \gamma_y \cos(\gamma_x \bar{x}_p)\sin(\gamma_y \bar{y}_p) \\ -\gamma_x \sin(\gamma_x \bar{x}_p)\cos(\gamma_y \bar{y}_p) \end{bmatrix}, & \alpha_2 = \mathrm{TE}, \\[2ex] \dfrac{\Lambda_{\boldsymbol{\alpha}}}{\Gamma_{\boldsymbol{\alpha}}}\,\Pi(\bar{x}_p, \bar{y}_p) \begin{bmatrix} \gamma_x \cos(\gamma_x \bar{x}_p)\sin(\gamma_y \bar{y}_p) \\ \gamma_y \sin(\gamma_x \bar{x}_p)\cos(\gamma_y \bar{y}_p) \end{bmatrix}, & \alpha_2 = \mathrm{TM}, \end{cases} \tag{2.12}$$

---

[2] Although $\boldsymbol{v}_{\bar{\boldsymbol{\beta}}}(x, y)$ is real, we include the conjugation for consistency of the notation.

$$\vartheta_{\bar{\boldsymbol{\alpha}},z}(\bar{x}_p,\bar{y}_p)=\begin{cases}-i\Lambda_{\boldsymbol{\alpha}}\Gamma_{\boldsymbol{\alpha}}\Pi(\bar{x}_p,\bar{y}_p)\cos(\gamma_x\bar{x}_p)\cos(\gamma_y\bar{y}_p), & \alpha_2=\mathrm{TE},\\ i\Lambda_{\boldsymbol{\alpha}}\Gamma_{\boldsymbol{\alpha}}\Pi(\bar{x}_p,\bar{y}_p)\sin(\gamma_x\bar{x}_p)\sin(\gamma_y\bar{y}_p), & \alpha_2=\mathrm{TM},\end{cases}\tag{2.13}$$

where we have introduced local coordinates for every pit or hole: $\bar{x}_p \equiv x - x_0^p, \bar{y}_p \equiv y - y_0^p$. Furthermore, the function $\Pi(\bar{x}_p,\bar{y}_p)$ is a rectangle function that indicates that the mode functions are identical to zero outside the cross-sectional area of the p-th hole:

$$\Pi(\bar{x}_p,\bar{y}_p)\equiv\left[\mathrm{H}(\bar{x}_p)-\mathrm{H}(\bar{x}_p-L_x^p)\right]\left[\mathrm{H}(\bar{y}_p)-\mathrm{H}(\bar{y}_p-L_y^p)\right],\tag{2.14}$$

where $\mathrm{H}(x)$ is the Heaviside step function. By using (2.12) it is easy to see that two different modes are orthogonal in the sense:

$$\langle\boldsymbol{v}_{\bar{\boldsymbol{\alpha}}}|\boldsymbol{v}_{\bar{\boldsymbol{\alpha}}'}\rangle_{\Omega_{p'}}\equiv\iint\limits_{\Omega_{p'}}\left(v_{\bar{\boldsymbol{\alpha}},x}v^*_{\bar{\boldsymbol{\alpha}}',x}+v_{\bar{\boldsymbol{\alpha}},y}v^*_{\bar{\boldsymbol{\alpha}}',y}\right)\mathrm{d}x\,\mathrm{d}y=0,\qquad\bar{\boldsymbol{\alpha}}\neq\bar{\boldsymbol{\alpha}}'.\tag{2.15}$$

Hence, $\{\boldsymbol{v}_{\bar{\boldsymbol{\alpha}}}\}$ is an orthonormal system with respect to the scalar product (2.15).

The following auxiliary functions are needed for the z-dependent parts $\eta_{\boldsymbol{\alpha}}$ and $\zeta_{\boldsymbol{\alpha}}$ in Equation (2.5):

$$f_{\boldsymbol{\alpha}}(z)=\begin{cases}-\exp[-i\gamma_z(z-z_1^p)], & |\gamma_z/k_p|\geq\epsilon,\ \alpha_4=-,\\ \exp[i\gamma_z(z-z_2^p)], & |\gamma_z/k_p|\geq\epsilon,\ \alpha_4=+,\\ -ik_p\gamma_z^{-1}\cos(\gamma_z z), & |\gamma_z/k_p|<\epsilon,\ \alpha_4=-,\\ i\sin(\gamma_z z), & |\gamma_z/k_p|<\epsilon,\ \alpha_4=+,\end{cases}\tag{2.16}$$

$$g_{\boldsymbol{\alpha}}(z)=\begin{cases}\exp[-i\gamma_z(z-z_1^p)], & |\gamma_z/k_p|\geq\epsilon,\ \alpha_4=-,\\ \exp[i\gamma_z(z-z_2^p)], & |\gamma_z/k_p|\geq\epsilon,\ \alpha_4=+,\\ k_p\gamma_z^{-1}\sin(\gamma_z z), & |\gamma_z/k_p|<\epsilon,\ \alpha_4=-,\\ \cos(\gamma_z z), & |\gamma_z/k_p|<\epsilon,\ \alpha_4=+,\end{cases}\tag{2.17}$$

The constants z_1^p and z_2^p are the z-coordinates of the upper and lower end of the pit or hole, respectively. Hence, for holes we have $z_1^p = D/2$ and $z_2^p = -D/2$, for pits we either have $z_1^p = D/2$ and $z_2^p = D/2 - d_p$ or we have $z_1^p = -D/2 + d_p$ and $z_2^p = -D/2$. We have introduced the constant factors like $\exp(i\gamma_z z_1^p)$ to make sure that, for imaginary γ_z, the moduli of the exponents are always equal to or smaller than unity. In Equations (2.16) and (2.17) we use the sine and cosine functions instead of the exponential function if the propagation constant γ_z is very small as compared to k_p, with smallness parameter ϵ.[3] If we would not do

---

[3] Although the ± for β_4 now does not have anything to do with the propagation direction, for consistency, we stick to this notation.

this, for $\gamma_z = 0$ for some mode, we would miss the mode function that is linear in z and our set of modes would not be complete.[4] In our implementation, we take $\epsilon = 10^{-5}$. For the z-dependent parts we now have:

$$\eta_{\boldsymbol{\alpha}}(z) = \begin{cases} \omega\mu_0\, g_{\boldsymbol{\alpha}}(z), & \alpha_2 = \text{TE}, \\ \gamma_z \sqrt{\frac{\mu_0}{\varepsilon_p\varepsilon_0}}\, f_{\boldsymbol{\alpha}}(z), & \alpha_2 = \text{TM}, \end{cases} \tag{2.18}$$

$$\zeta_{\boldsymbol{\alpha}}(z) = \begin{cases} \gamma_z\, f_{\boldsymbol{\alpha}}(z), & \alpha_2 = \text{TE}, \\ k_p\, g_{\boldsymbol{\alpha}}(z), & \alpha_2 = \text{TM}. \end{cases} \tag{2.19}$$

Note that the modes are propagating in the z-direction if $\Gamma_{\boldsymbol{\alpha}} < k_p$, while for $\Gamma_{\boldsymbol{\alpha}} > k_p$ the modes are evanescent. For a square pit or hole ($L_x = L_y$) with $L_x < \lambda_p/2$ all modes are evanescent.

The z-component of the electric and magnetic field of the waveguide modes are given by:

$$E_{\boldsymbol{\alpha},z}(x,y,z) = \begin{cases} 0, & \alpha_2 = \text{TE}, \\ \sqrt{\frac{\mu_0}{\varepsilon_p\varepsilon_0}}\, \vartheta_{\bar{\boldsymbol{\alpha}},z}(x,y)\, g_{\boldsymbol{\alpha}}(z), & \alpha_2 = \text{TM}, \end{cases} \tag{2.20a}$$

$$H_{\boldsymbol{\alpha},z}(x,y,z) = \begin{cases} \vartheta_{\bar{\boldsymbol{\alpha}},z}(x,y)\, g_{\boldsymbol{\alpha}}(z), & \alpha_2 = \text{TE}, \\ 0, & \alpha_2 = \text{TM}. \end{cases} \tag{2.20b}$$

We note here that the normalization of the waveguide modes involves only $\boldsymbol{v}_{\bar{\boldsymbol{\alpha}}}$, which is the part of the transverse field that does not depend on z. This means that the above z-dependent part is only defined up to a constant. We have chosen this constant such that for both TE and TM polarization the waveguide modes have the same order of magnitude.

2.2 Mode expansion above and below the layer

In this section, we describe the electromagnetic field above and below the conducting layer. This field is expanded in propagating and evanescent plane waves, that are characterized by their polarization and their direction of propagation.

The total electric and magnetic field above and below the conducting layer consist of the (known) incident field, its corresponding reflected field (that results from

---

[4] The reader might wonder why we do not use the sine and cosine form always instead of using the exponential form only for $|\beta_z/k_p| < \epsilon$. However, for large and purely imaginary β_z, the functions $\cos(\beta_z z)$ and $\sin(\beta_z z)$ increase exponentially with $|z|$, which is not very convenient for numerical implementation.

the incident field when the conducting layer does not contain any pits or holes) and the scattered field (caused by the presence of the pits and holes):

$$\begin{bmatrix} \mathbf{E}(\mathbf{r}) \\ \mathbf{H}(\mathbf{r}) \end{bmatrix} = \begin{bmatrix} \mathbf{E}^i(\mathbf{r}) \\ \mathbf{H}^i(\mathbf{r}) \end{bmatrix} + \begin{bmatrix} \mathbf{E}^r(\mathbf{r}) \\ \mathbf{H}^r(\mathbf{r}) \end{bmatrix} + \begin{bmatrix} \mathbf{E}^s(\mathbf{r}) \\ \mathbf{H}^s(\mathbf{r}) \end{bmatrix}. \tag{2.21}$$

The reflected field can easily be calculated from the incident field and we therefore consider the sum of the incident and reflected field to be known. The scattered field can be written as:

$$\begin{bmatrix} \mathbf{E}^s(\mathbf{r}) \\ \mathbf{H}^s(\mathbf{r}) \end{bmatrix} = \sum_{\beta_1} \int_{-\infty}^{\infty} b_{\boldsymbol{\beta}} \begin{bmatrix} \mathbf{E}_{\boldsymbol{\beta}}(\mathbf{r}) \\ \mathbf{H}_{\boldsymbol{\beta}}(\mathbf{r}) \end{bmatrix} \mathrm{d}\beta_2, \tag{2.22}$$

where the coefficients $b_{\boldsymbol{\beta}}$ are still to be determined and $\left(\mathbf{E}_{\boldsymbol{\beta}}, \mathbf{H}_{\boldsymbol{\beta}}\right)$ are plane waves with wave vector $\mathbf{k}_u$ above the layer and $\mathbf{k}_\ell$ below the layer. The tangential components (k_x, k_y) of the wave vector are real whereas the z-component is given by:

$$k_z^u = +\sqrt{k_u^2 - k_x^2 - k_y^2}, \tag{2.23a}$$

$$k_z^\ell = -\sqrt{k_\ell^2 - k_x^2 - k_y^2}. \tag{2.23b}$$

The sign before the square root follows from the assumed time dependence, which is $\exp(-i\omega t)$ with $\omega > 0$, and from the Sommerfeld radiation condition introduced in Section 1.6. The subscript $\boldsymbol{\beta} = (\beta_1, \beta_2)$ is a short notation for the polarization, denoted by β_1, and the x- and y-component of the wave vector ($\beta_2 = (k_x, k_y)$). The polarization can either be S or P. S-polarized means that the z-component of the electric field is zero (and thus corresponds to TE polarization inside the holes and pits), while for P-polarization the z-component of the magnetic field is zero (TM polarization). Note that the integral $\int \mathrm{d}\beta_2$ is a shorthand notation for $\iint \mathrm{d}k_x \mathrm{d}k_y$.

We use Equation (2.4) to obtain the transverse components of the plane waves and, as before, we split these into a factor that depends on x and y and a factor that depends on z:

$$\mathbf{e}_{\boldsymbol{\beta}}(x, y, z) = \boldsymbol{v}_{\boldsymbol{\beta}}(x, y)\, \eta_{\boldsymbol{\beta}}(z), \tag{2.24a}$$

$$\mathbf{h}_{\boldsymbol{\beta}}(x, y, z) = \boldsymbol{v}_{\boldsymbol{\beta}}(x, y)\, \zeta_{\boldsymbol{\beta}}(z). \tag{2.24b}$$

These are given in the next section.

Analogous to the normalization of the waveguide mode functions, we normalize $\boldsymbol{v}_{\boldsymbol{\beta}}$ such that:

$$\langle \boldsymbol{v}_{\boldsymbol{\beta}} | \boldsymbol{v}_{\boldsymbol{\beta}'} \rangle_{\mathbb{R}^2} \equiv \iint_{\mathbb{R}^2} \left(v_{\boldsymbol{\beta},x} v^*_{\boldsymbol{\beta}',x} + v_{\boldsymbol{\beta},y} v^*_{\boldsymbol{\beta}',y} \right) \mathrm{d}x\, \mathrm{d}y = \delta_{\beta_1 \beta_1'}\, \delta\left(\beta_2 - \beta_2'\right). \tag{2.25}$$

Note that the integration is over an entire plane. The first δ is the Kronecker delta and the second is the two-dimensional Dirac delta function:

$$\delta(\beta_2) = \frac{1}{4\pi^2} \int_{-\infty}^{\infty} \int_{-\infty}^{\infty} e^{i(k_x x + k_y y)}\, \mathrm{d}x \mathrm{d}y, \qquad \beta_2 = (k_x, k_y). \tag{2.26}$$

Analogous to the scalar product for the waveguide mode functions, the scalar product of two identical plane waves $\langle \boldsymbol{v}_{\boldsymbol{\beta}} | \boldsymbol{v}_{\boldsymbol{\beta}} \rangle_{\mathbb{R}^2}$ is related to the flow of energy of the plane wave through a plane of constant z.

The definition of rotated transverse electric and magnetic fields $\mathbf{e}_{\boldsymbol{\beta}}$ and $\mathbf{h}_{\boldsymbol{\beta}}$ and Maxwell's equations (1.15c) and (1.15d) on page 6 imply the following convenient relations between the transverse components of the electric and the magnetic field of the plane waves:

$$\mathbf{h}_{\boldsymbol{\beta}}(x,y,z) = \frac{k_z}{\omega\mu_0} \mathbf{e}_{\boldsymbol{\beta}}(x,y,z), \qquad \text{if } \beta_1 = \mathrm{S}, \tag{2.27a}$$

$$\mathbf{h}_{\boldsymbol{\beta}}(x,y,z) = \frac{\omega\varepsilon\varepsilon_0}{k_z} \mathbf{e}_{\boldsymbol{\beta}}(x,y,z), \qquad \text{if } \beta_1 = \mathrm{P}. \tag{2.27b}$$

Furthermore, every time-harmonic solution of the Maxwell equations in the half spaces $z > D/2$ and $z < -D/2$ having frequency ω, that propagates away from the conducting layer can be expanded in terms of the plane waves $(\mathbf{E}_{\boldsymbol{\beta}}, \mathbf{H}_{\boldsymbol{\beta}})$. In particular, we have, for the scattered transverse electric field:

$$\mathbf{e}^s(x,y,z) = \sum_{\beta_1} \int_{-\infty}^{\infty} b_{\boldsymbol{\beta}}\, \mathbf{e}_{\boldsymbol{\beta}}(x,y,z)\, \mathrm{d}\beta_2, \tag{2.28}$$

where, as before, the integration over β_2 is a short-hand notation for integrating over k_x and k_y.

By using Equation (2.25) and (2.27) we define an operator $\mathscr{A}$ that maps any two-dimensional vector field $\mathbf{f} : \mathbb{R}^2 \to \mathbb{C}^2$ onto another such vector field:

$$\mathscr{A}(\mathbf{f}) \equiv \int_{-\infty}^{\infty} \frac{k_z}{\omega\mu_0} \left\langle \mathbf{f} \middle| \boldsymbol{v}^{\mathrm{S}}_{\beta_2} \right\rangle_{\mathbb{R}^2} \boldsymbol{v}^{\mathrm{S}}_{\beta_2}\, \mathrm{d}\beta_2 + \int_{-\infty}^{\infty} \frac{\omega\varepsilon\varepsilon_0}{k_z} \left\langle \mathbf{f} \middle| \boldsymbol{v}^{\mathrm{P}}_{\beta_2} \right\rangle_{\mathbb{R}^2} \boldsymbol{v}^{\mathrm{P}}_{\beta_2}\, \mathrm{d}\beta_2, \tag{2.29}$$

where the superscript S or P naturally means that $\beta_1 = \mathrm{S}$ or $\beta_1 = \mathrm{P}$. This operator is basically the integral version of the operator $\frac{\mathbf{k}}{\omega\mu_0}\times$ that can be applied to the electric field of a plane wave to calculate the corresponding magnetic field. Note that the factor $\frac{\omega\varepsilon\varepsilon_0}{k_z}$ in the second integral is singular for $k_x^2 + k_y^2 = \omega^2\varepsilon\varepsilon_0\mu_0$. This is the fingerprint of the electromagnetic surface wave. Although the integrand is integrable, in the numerical implementation prudence is essential.

In any plane z is constant and in particular for $z = \pm D/2$, the scattered transverse magnetic field can now be expressed in terms of the electric field:

$$\mathbf{h}^s(x, y, \pm D/2) = \mathscr{A}\left[\mathbf{e}^s(x, y, \pm D/2)\right], \tag{2.30}$$

where for $z = D/2$ we have $k_z = k_z^u$ and for $z = -D/2$ we have $k_z = k_z^\ell$ in the definition of operator $\mathscr{A}$. The above equation holds for all (x, y) with $-\infty < x, y < \infty$.

2.2.1 Listing of plane wave functions

With:

$$\Gamma_{\boldsymbol{\beta}} = \sqrt{k_x^2 + k_y^2}, \tag{2.31}$$

and

$$\Lambda_{\boldsymbol{\beta}} = -\frac{1}{2\pi}, \tag{2.32}$$

we define the following functions that are independent of z:

$$\boldsymbol{v}_{\boldsymbol{\beta}}(x, y) = \begin{cases} \dfrac{\Lambda_{\boldsymbol{\beta}}}{\Gamma_{\boldsymbol{\beta}}} e^{i(k_x x + k_y y)} \begin{pmatrix} k_y \\ -k_x \end{pmatrix}, & \beta_1 = \mathrm{S},\ k_x^2 + k_y^2 > 0, \\ \Lambda_{\boldsymbol{\beta}} \begin{pmatrix} 0 \\ -1 \end{pmatrix}, & \beta_1 = \mathrm{S},\ k_x^2 + k_y^2 = 0, \\ \dfrac{\Lambda_{\boldsymbol{\beta}}}{\Gamma_{\boldsymbol{\beta}}} e^{i(k_x x + k_y y)} \begin{pmatrix} k_x \\ k_y \end{pmatrix}, & \beta_1 = \mathrm{P},\ k_x^2 + k_y^2 > 0, \\ \Lambda_{\boldsymbol{\beta}} \begin{pmatrix} 1 \\ 0 \end{pmatrix}, & \beta_1 = \mathrm{P},\ k_x^2 + k_y^2 = 0, \end{cases} \tag{2.33}$$

$$\vartheta_{\boldsymbol{\beta},z}(x, y) = \Lambda_{\boldsymbol{\beta}} \Gamma_{\boldsymbol{\beta}}\, e^{i(k_x x + k_y y)}, \tag{2.34}$$

For the z-dependent part we have the following auxiliary function:

$$f_{\boldsymbol{\beta}}(z) = \begin{cases} \exp[i k_z^u (z - D/2)], & z > D/2, \\ \exp[i k_z^\ell (z + D/2)], & z < -D/2, \end{cases} \tag{2.35}$$

and the actual z-dependent parts:

$$\eta_{\boldsymbol{\beta}}(z) = \begin{cases} \omega\mu_0 f_{\boldsymbol{\beta}}(z), & \beta_1 = \mathrm{S}, \\ k_z \sqrt{\frac{\mu_0}{\varepsilon\varepsilon_0}}\, f_{\boldsymbol{\beta}}(z), & \beta_1 = \mathrm{P}, \end{cases} \tag{2.36}$$

$$\zeta_{\boldsymbol{\beta}}(z) = \begin{cases} k_z f_{\boldsymbol{\beta}}(z), & \beta_1 = \mathrm{S}, \\ k f_{\boldsymbol{\beta}}(z), & \beta_1 = \mathrm{P}. \end{cases} \tag{2.37}$$

Note that k, k_z and ε in the above equations are either k_u, k_z^u and ε_u or k_ℓ, k_z^ℓ and ε_ℓ, depending on z. The z-components of the plane waves are given by:

$$E_{\boldsymbol{\beta},z}(x,y,z) = \begin{cases} 0, & \beta_1 = \mathrm{S}, \\ \sqrt{\frac{\mu_0}{\varepsilon\varepsilon_0}}\,\vartheta_{\boldsymbol{\beta},z}(x,y)\, f_{\boldsymbol{\beta}}(z), & \beta_1 = \mathrm{P}, \end{cases} \tag{2.38a}$$

$$H_{\boldsymbol{\beta},z}(x,y,z) = \begin{cases} \vartheta_{\boldsymbol{\beta},z}(x,y)\, f_{\boldsymbol{\beta}}(z), & \beta_1 = \mathrm{S}, \\ 0, & \beta_1 = \mathrm{P}. \end{cases} \tag{2.38b}$$

Note that we did not take special precautions for the case that $k_z = 0$. For the waveguide modes in the previous section, we made sure that, when it happens that $\gamma_z = 0$, the set of mode functions is still complete. The plane waves in the upper and lower half spaces, however, form a continuous set that is parametrized by $-\infty < k_x, k_y < \infty$. The plane waves with $k_z = 0$ are only a set of measure zero in the space of all plane waves and are therefore irrelevant for the completeness.

2.3 Matching at the interfaces

At the interfaces $z = \pm D/2$, we have the following relations for the tangential electric and the tangential magnetic field:

$$\mathbf{e}^{\mathrm{pit}} = \mathbf{e}^i + \mathbf{e}^r + \mathbf{e}^s, \qquad \forall (x,y),\ z = \pm D/2, \tag{2.39a}$$

$$\mathbf{h}^{\mathrm{pit}} = \mathbf{h}^i + \mathbf{h}^r + \mathbf{h}^s, \qquad (x,y) \in \bigcup_{\alpha_1} \Omega_{\alpha_1},\ z = \pm D/2. \tag{2.39b}$$

Here, Ω_{α_1} is, as before, the cross-section of the pit or hole that is labeled by index α_1. In Equation (2.39a), because the layer is perfectly conducting, the sum of the incident and reflected tangential electric field vanishes at $z = \pm D/2$, hence:

$$\mathbf{e}^{\mathrm{pit}} = \mathbf{e}^s, \qquad \forall (x,y),\ z = \pm D/2. \tag{2.40}$$

Using this together with Equation (2.30), we have for Equation (2.39b):

$$\mathbf{h}^{\mathrm{pit}} = \mathbf{h}^i + \mathbf{h}^r + \mathscr{A}\left(\mathbf{e}^{\mathrm{pit}}\right), \tag{2.41}$$

which is valid for all $(x, y, \pm D/2)$ within the holes and pits. The waveguide modes that constitute $\mathbf{e}^{\mathrm{pit}}$ and $\mathbf{h}^{\mathrm{pit}}$ are zero outside the pits and holes, as indicated by the rectangle function Π in Equations (2.12) and (2.13) on page 22.

In order to obtain a system of equations that is suitable for numerical implementation, we project this equation on the function $\boldsymbol{v}_{\tilde{\boldsymbol{\alpha}}'}$ by using the scalar product defined by the left-hand side of Equation (2.6) and by using (2.7):

$$\sum_{\alpha_4} a_{\boldsymbol{\alpha}'}\,\zeta_{\boldsymbol{\alpha}'}(\pm D/2) - \sum_{\boldsymbol{\alpha}} a_{\boldsymbol{\alpha}}\,\eta_{\boldsymbol{\alpha}}(\pm D/2)\left\langle \mathscr{A}\left(\boldsymbol{v}_{\tilde{\boldsymbol{\alpha}}}\right) \middle| \boldsymbol{v}_{\tilde{\boldsymbol{\alpha}}'} \right\rangle_{\Omega_{p'}} = \left\langle \mathbf{h}^i + \mathbf{h}^r \middle| \boldsymbol{v}_{\tilde{\boldsymbol{\alpha}}'} \right\rangle_{\Omega_{p'}}, \tag{2.42}$$

where the summation over α_4 is a summation over the two directions of propagation (α_4 is not contained in $\bar{\boldsymbol{\alpha}}$). This equation is valid for all $\bar{\boldsymbol{\alpha}}'$, hence for all α_1 (counting the number of holes and pits), for all α_2 (TE and TM polarization) and for all α_3 (the mode numbers, m_x and m_y). Consequently, solving the system of Equation (2.42) for all $\bar{\boldsymbol{\alpha}}'$ and for $z = \pm D/2$ gives the waveguide mode expansion coefficients $a_{\boldsymbol{\alpha}}$. Note that the term on the right acts as a source term. The factor $\left\langle \mathscr{A}\left(\boldsymbol{v}_{\bar{\boldsymbol{\alpha}}}\right) \middle| \boldsymbol{v}_{\bar{\boldsymbol{\alpha}}'} \right\rangle_{\Omega_{p'}}$ is called the interaction integral. Physically speaking, it describes the interaction of a waveguide mode $\bar{\boldsymbol{\alpha}}$, via the scattered plane waves through operator $\mathscr{A}$, with another mode $\bar{\boldsymbol{\alpha}}'$ in the same or in another pit or hole. In Appendix A we will discuss some of its properties and a method to compute it numerically.

To obtain an expression for the scattered field, we use the orthonormality of the plane waves with respect to the scalar product defined by the left-hand side of Equation (2.25) to project Equation (2.40) for the tangential electric field on the mode function $\boldsymbol{v}_{\boldsymbol{\beta}'}$:

$$b_{\boldsymbol{\beta}'} = \sum_{\boldsymbol{\alpha}} a_{\boldsymbol{\alpha}} \frac{\eta_{\boldsymbol{\alpha}}(\pm D/2)}{\eta_{\boldsymbol{\beta}'}(\pm D/2)} \left\langle \boldsymbol{v}_{\boldsymbol{\alpha}} \middle| \boldsymbol{v}_{\boldsymbol{\beta}'} \right\rangle_{\mathbb{R}^2}. \tag{2.43}$$

In this way, the tangential scattered field can be expressed in the amplitudes of the modes of the pits and holes:

$$\mathbf{e}^s(\mathbf{r}) = \sum_{\beta_1} \sum_{\boldsymbol{\alpha}} \int_{-\infty}^{\infty} a_{\boldsymbol{\alpha}} \frac{\eta_{\boldsymbol{\alpha}}(\pm D/2)}{\eta_{\boldsymbol{\beta}}(\pm D/2)} \left\langle \boldsymbol{v}_{\boldsymbol{\alpha}} \middle| \boldsymbol{v}_{\boldsymbol{\beta}'} \right\rangle_{\mathbb{R}^2} \boldsymbol{v}_{\boldsymbol{\beta}}(x, y)\, \eta_{\boldsymbol{\beta}}(z)\, \mathrm{d}\beta_2, \tag{2.44a}$$

$$\mathbf{h}^s(\mathbf{r}) = \sum_{\beta_1} \sum_{\boldsymbol{\alpha}} \int_{-\infty}^{\infty} a_{\boldsymbol{\alpha}} \frac{\eta_{\boldsymbol{\alpha}}(\pm D/2)}{\eta_{\boldsymbol{\beta}}(\pm D/2)} \left\langle \boldsymbol{v}_{\boldsymbol{\alpha}} \middle| \boldsymbol{v}_{\boldsymbol{\beta}'} \right\rangle_{\mathbb{R}^2} \boldsymbol{v}_{\boldsymbol{\beta}}(x, y)\, \zeta_{\boldsymbol{\beta}}(z)\, \mathrm{d}\beta_2. \tag{2.44b}$$

The z-components of the scattered electric and magnetic field are derived by differentiation of the transverse electric and magnetic field with respect to x and y, with Maxwell' equations (1.15c) and (1.15d).

With Equation (2.42) and (2.43) we have formulated our three-dimensional vectorial scattering problem as a linear system for the amplitudes of the waveguide modes only. Since these modes are parametrized by a countable set of two parameters (γ_x and γ_y), we have thus reduced the three-dimensional scattering problem to a two-dimensional numerical problem.

2.4 Singularities at the edges

It can be shown that the integrands in Equation (2.44) are integrable everywhere, except, possibly, at the edges of the holes and pits. The occurrence of infinite fields near infinitely sharp, conducting wedges is well-known [12]. For a protruding,

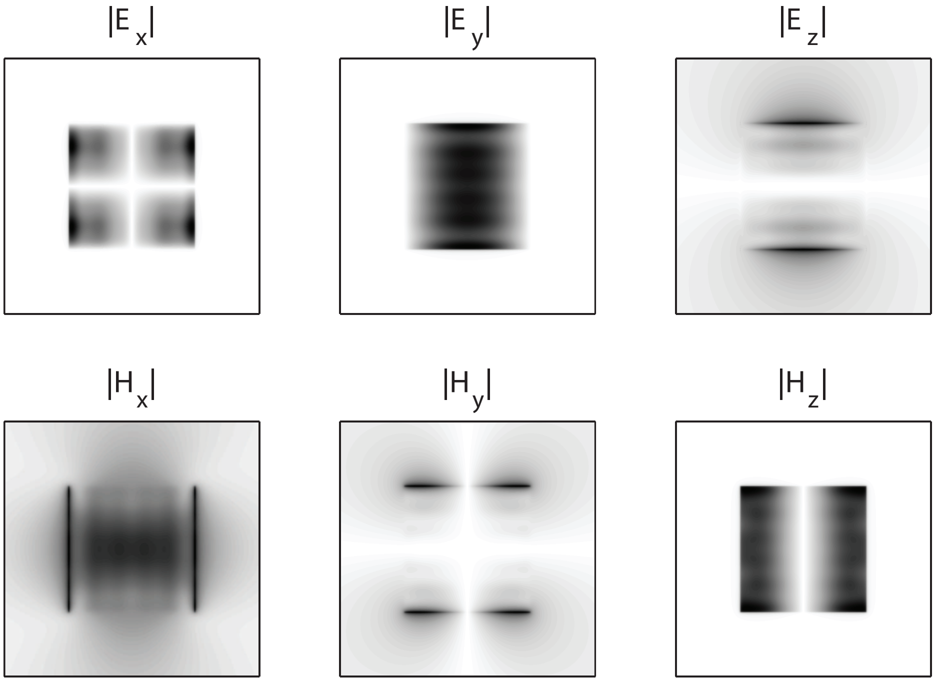

Figure 2.1: The absolute value of the electric and magnetic field strength in a plane with constant z, at a distance of $\lambda/300$ below a layer with thickness 0.27λ. Fields are taken at the shadow side of a square hole with $L_x = L_y = 2/3\lambda$, which is illuminated by a perpendicular incident plane wave that is polarized in the y-direction. White denotes zero field strength and black maximum field strength. The six graphs have different scales.

right angle, perfectly conducting wedge, the field components perpendicular to the sharp edge may become infinite as $r^{-1/3}$, where r is the distance to the edge. The field components parallel to the edge remain finite. Furthermore, the charge density always remains finite. At an intruding wedge, such as the inner part of the pits and holes, all field components remain finite.

Figure 2.1 shows a gray scale picture of the electric and magnetic field strength at the shadow side of a square hole. The plane of the figure is the (x, y)-plane, at a distance of $\lambda/300$ below the perfectly conducting layer. The incident field is polarized in the y-direction. All field components have their maximum near an edge. If a field component is parallel to a certain edge, its strength is zero. The components E_x, H_x and H_y are sharply peaked at the edges to which they are perpendicular.

Figure 2.2 on the next page shows the absolute value of the z-component of the electric field as a function of the distance to the edge. This distance ranges between $\lambda/300$ and $\lambda/30$ and corresponds to different planes with constant z. The behaviour of E_z indeed resembles the function $r^{-1/3}$.

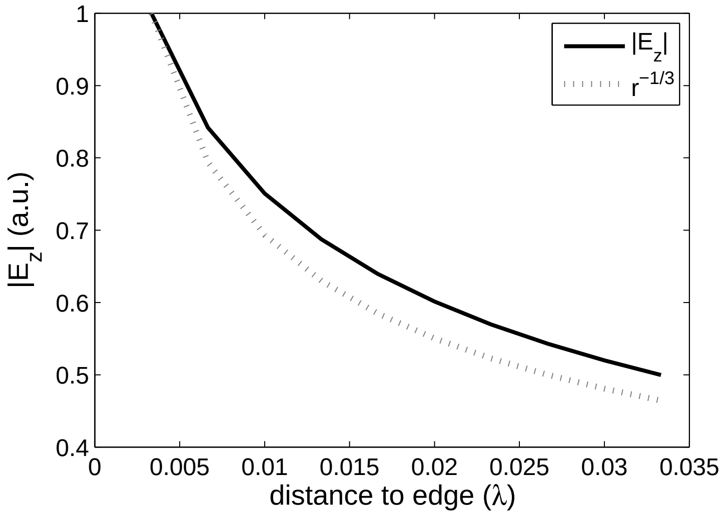

Figure 2.2: The absolute value of E_z as a function of the distance to the edge. The setup is the same as described in Figure 2.1 on the preceding page. As a reference, the function $r^{-1/3}$ is also given.

2.5 Numerical considerations

Of course, when implementing our diffraction problem into a computer code we will have to truncate the infinite series of waveguide modes. For large γ_x and γ_y, and depending on the size L_x^p and L_y^p, the mode of concern will be evanescent in the z-direction. For large imaginary γ_z, the mode will only penetrate into the hole or pit a very small distance. It is therefore reasonable to expect that only the modes with a small imaginary γ_z will contribute to the total result. Roberts [11] used 168 modes, while García-Vidal and coworkers [13] used only one. To compare the results of two calculations, one with a number N and the second with a smaller number $\widetilde{N}$, we define the following measure:

$$F_{N\widetilde{N}} = \frac{\iiint\limits_{V_p} \left(\varepsilon_0 |\mathbf{E}_{\widetilde{N}} - \mathbf{E}_N|^2 + \mu_0 |\mathbf{H}_{\widetilde{N}} - \mathbf{H}_N|^2\right) \mathrm{d}x\,\mathrm{d}y\,\mathrm{d}z}{\iiint\limits_{V_p} \left(\varepsilon_0 |\mathbf{E}_{\widetilde{N}}|^2 + \mu_0 |\mathbf{H}_{\widetilde{N}}|^2\right) \mathrm{d}x\,\mathrm{d}y\,\mathrm{d}z}, \tag{2.45}$$

where the integration is over the volume V_p of the hole (or pit). Here, $\left(\mathbf{E}_{\widetilde{N}}, \mathbf{H}_{\widetilde{N}}\right)$ is the electromagnetic field inside the hole for which the series are truncated after $\widetilde{N}$ waveguide modes and $(\mathbf{E}_N, \mathbf{H}_N)$ is the electromagnetic field inside the hole obtained by truncation after N waveguide modes. Hence, this measure corresponds to the relative error in the energy.

Figure 2.3 on the facing page shows this error as a function of the number of unknowns for a few typical setups. It is clear that several hundreds of unknowns per

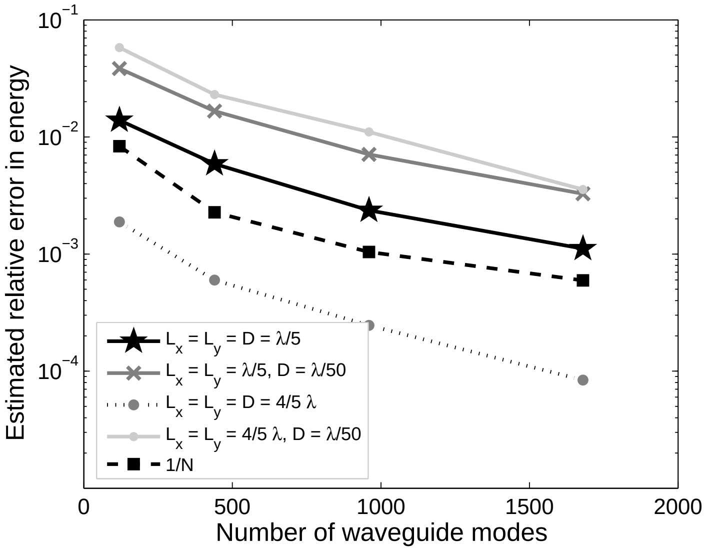

Figure 2.3: Relative error $F_{N\tilde{N}}$ with $N = 2600$ as a function of the number of waveguide modes ($\tilde{N} = 120, 440, 960, 1680$). Setup is a single hole with a perpendicular incident, linearly polarized plane wave. As a reference, $1/N$ is also plotted.

hole or pit are enough to model our three-dimensional problem accurately, provided that the thickness of the layer is not too small.

Figure 2.4 on the next page shows a line scan of the electric field inside a single hole, for various numbers of waveguide modes. Figure 2.4(a) shows the field at the entrance of the hole, whereas Figure 2.4(b) shows the field in the middle of the hole. Large numbers of waveguide modes are needed to show the singular behavior at the rim of the hole, as is clear from Figure 2.4(a). Inside the hole, where the fields are smooth and regular, the difference with respect to the electric field between 120 waveguide modes and as much as 2600 waveguide modes is not much more than 1 percent. Hence, if the singular behavior of the fields dominates the solution, as is the case when the conducting layer is thin as compared to the wavelength, our mode expansion technique is probably not the most suitable method.

A small system of equations with only several hundreds of unknowns is solved on a regular desk top computer in only a few seconds. Consequently, most computation time is spent on calculating the interaction integrals, which, with the present version of the code, takes a few hours. As discussed in Appendix A, these integrals contain an exponential factor that oscillates violently when mode $\bar{\boldsymbol{\alpha}}$ and $\bar{\boldsymbol{\alpha}}'$ live in pits or holes that are far apart. Moreover, the integral contains the factor $1/k_z$ that is singular on the circle given by $k_x^2 + k_y^2 = k^2$. As stated before, this is the fingerprint of the electromagnetic surface wave. The integrand is still integrable, but a careful implementation is required.

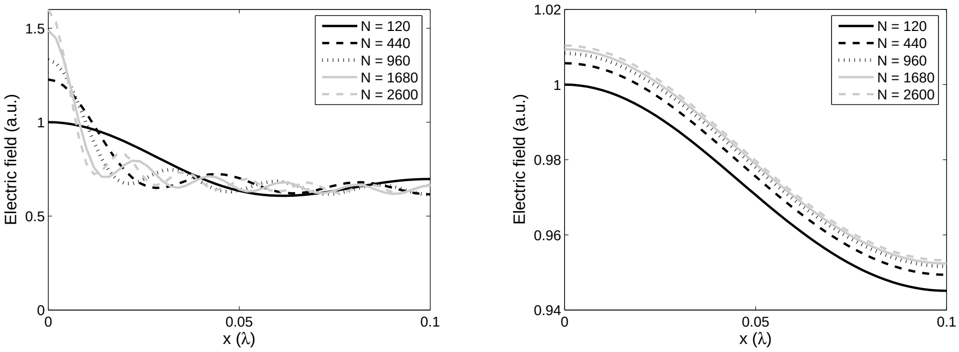

(a) $z = D/2$ **(b)** $z = 0$

Figure 2.4: Line scan of the absolute value of the x-component of the electric field in a plane with constant z, through the center of the hole, for various numbers of waveguide modes. Setup is a single hole, $L_x = L_y = D = \lambda/5$, with a perpendicular incident, linearly polarized plane wave. Note the different scales.

However, because the interaction integral only involves the plane $z = \pm D/2$, it does not depend on the following important parameters: the thickness D of the conducting layer; the index of refraction n_p inside the pit or hole; whether the scatterer is a pit or a hole and, in case of a pit, its depth d_p. Consequently, once the interaction integrals are calculated for a certain setup, we can vary these parameters with negligible computational effort. This is a great advantage of our method. The possibility to construct a library of interaction integrals is also beneficial.

Chapter 3

Calculations and measurements of a terahertz pulse

3.1 Introduction

In this chapter, the results obtained with the mode expansion theory, as explained in Chapter 2, will be compared with measurements done on a pulse with its frequency spectrum in the terahertz (THz) region. Although the measurements were not done by the author, the experimental setup will be briefly discussed.

The left hand part of Figure 3.1 on the following page shows the experimental setup. A linearly polarized terahertz pulse illuminates a metal sample which is placed on top of a GaP electro-optic detection crystal. The length of the pulse is about 5 ps. From below, a linearly polarized probe laser pulse is focused on the top surface of the crystal. The length of this probe pulse is 20 fs. When a terahertz electric field is present in the crystal, the electro-optic effect changes the probe polarization from linear to elliptical. The top surface of the crystal is coated such that the probe pulse is reflected, however, the coating has a negligible effect on the terahertz field. The reflected probe pulse is sent to a differential detection setup. It can be shown that the signal of the differential detection setup is linearly proportional to the instantaneous terahertz electric field [14]. As the probe beam can be optically delayed with respect to the terahertz beam, it is possible to obtain the terahertz electric field as a function of time. Furthermore, the probe beam can be translated in the x and y-direction, such that a two-dimensional scan of the electric field can be made. More elaborate discussions of the experimental setup can be found in references [15–17].

As the electro-optic effect changes the index of refraction of the crystal only along a single axis, the orientation of the electro-optic crystal determines the component of the electric field that is measured. In the results shown in the next section,

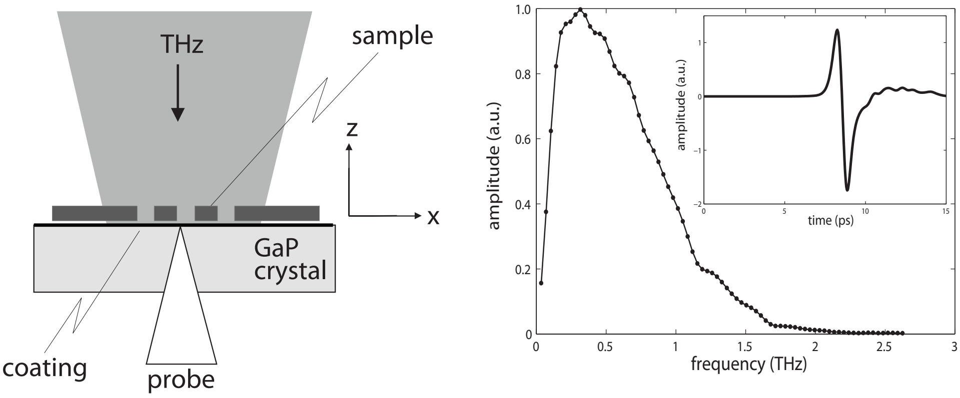

Figure 3.1: Left: The setup used to measure the THz near field at the shadow side of a aluminum foil with square holes. Right: Terahertz power spectrum of the dominant polarization, calculated from a typical incident field as a function of delay shown in the inset.

a (001) oriented crystal is used to measure the z-component, whereas a (110) oriented crystal is used to measure the x-component. This latter crystal is rotated 90° with respect to the z-axis to measure the y-component. As the two crystals have different coatings, it is not possible to compare the results for the z-component with the results for the x and y-components quantitatively.

The signal that is obtained from the differential setup is, strictly speaking, not proportional to the terahertz electric field in a point, but, rather, related to the terahertz electric field in the volume occupied by the probe beam inside the crystal. The diameter of the probe beam is smaller than $7\,\mu$m over a considerable distance inside the crystal [16], hence in terms of the wavelengths of the THz pulse, this volume is not very large in the transverse directions. In the z-direction, however, the measured signal certainly is a spatial integral over the thickness of the crystal. Especially for the components of the terahertz electric field that are propagating in the z-direction, this will constitute a deviation from the ideal of a point-like measurement. However, for evanescent components, that decrease exponentially in the z-direction, the result will be closer to the ideal.

The measurements were done on aluminum foils, either with a thickness of $80\,\mu$m or $200\,\mu$m. Results are shown for foils with a finite number of square holes with a size of $200 \times 200\,\mu\text{m}^2$. The electric field of the incident terahertz pulse and its spectrum are shown in the right hand part of Figure 3.1. The dominant polarization of the THz pulse is in the y-direction. The diameter of the focus of the THz pulse is approximately 1 mm and the numerical aperture is 0.24. The thickness of the electro-optic crystal was $80\,\mu$m. The penetration depth of THz radiation in aluminum is estimated to be a few tens of nanometers [17], which is about three orders of magnitude smaller than the wavelength. The perfect conductor assumption is thus valid. In the calculations, we took into account 440 waveguide modes per hole. The terahertz pulse was represented by 75 perpendicular plane waves with frequencies and amplitude denoted by the markers in Figure 3.1. Hence, no focusing effects of the THz pulse were considered in the calculations.

3.2 Results

Figure 3.2 on the following page shows calculations for a terahertz pulse that is incident from above on a metal layer with a single square hole. The three time frames that are shown correspond to the three vertical dashed lines in Figure 3.3. The y and z-component of the electric field are calculated in the (y,z)-plane, that is the plane parallel to the optical axis and the direction of polarization of the incident pulse. The x-coordinate coincides with the center of the hole. As the incident field is y-polarized, no E_z component is present in the incident terahertz field. Due to diffraction at the edges of the hole, an E_z component is created. The y-component of the electric field is mainly propagating in the z-direction, whereas the z-component propagates along the metal-air interface.

Figure 3.3 on page 37 shows calculations of the y-component of the electric field as a function of time, and its frequency spectrum, for three points that are indicated in Figure 3.2 by the black crosses. For the point above the layer, at the illuminated side, the time signal clearly shows the incident and the reflected pulse. In the frequency spectrum, this leads to constructive or destructive interference between the incident and the reflected pulse (and anything in between), depending on the frequency. For the electric field at the center of the hole, we can see a broadening of the pulse in time, which is caused by the attenuation of the lower frequencies. The hole in fact acts as a high pass filter. All frequencies below the cutoff of the hole are attenuated. The main feature of the y-component of the electric field below the layer is its decreased amplitude, which demonstrates the scattering of the field by the hole in all directions, as was seen in the previous figure.

Figure 3.4 on page 38 shows a comparison between measurements and calculations of the z-component of the electric field below a layer with multiple square holes, for a single frequency of 1 THz. The layer has a thickness of $80\,\mu$m and the holes have a width of $200\,\mu$m. The incident field is polarized in the direction denoted by the arrow in the upper left figure. The calculations were done in a plane $10\,\mu$m below the perfect conductor, on the shadow side. To indicate the location of the holes, squares are drawn in the figures of the measurements. However, these are just added as a guide to the eye and need not be precisely at the right position. Their size is correct, though. Apart from an electric field in the z-direction at the edges of the holes, the second and fourth setup also show lobes in between the holes. The wavelength corresponding to 1 THz is $300\,\mu$m, which is

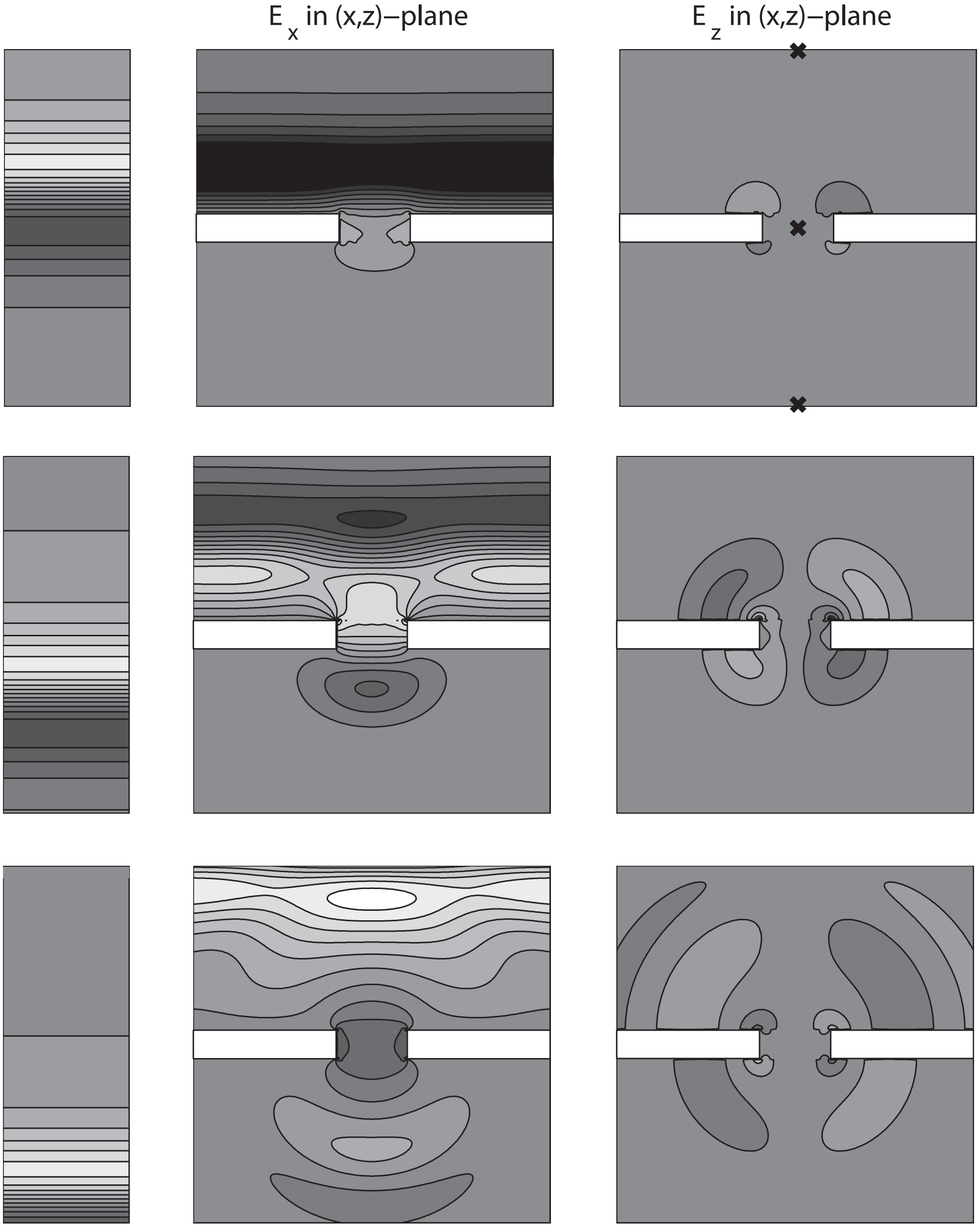

Figure 3.2: Gray-scale plots of three time frames of the y-component and the z-component of the electric field in the (y,z)-plane, for a THz pulse incident from above on a square hole with size $200\,\mu$m in a layer with a thickness of $80\,\mu$m. Black means a positive value of the electric field and white denotes a negative value, except for the metal layer, in which the electric field is zero. The size of the windows is 1 mm by 1 mm. In the small figures on the left the y-component of the electric field is shown for a freely propagating pulse. Time frames are taken at the vertical lines in the upper graph of Figure 3.3.

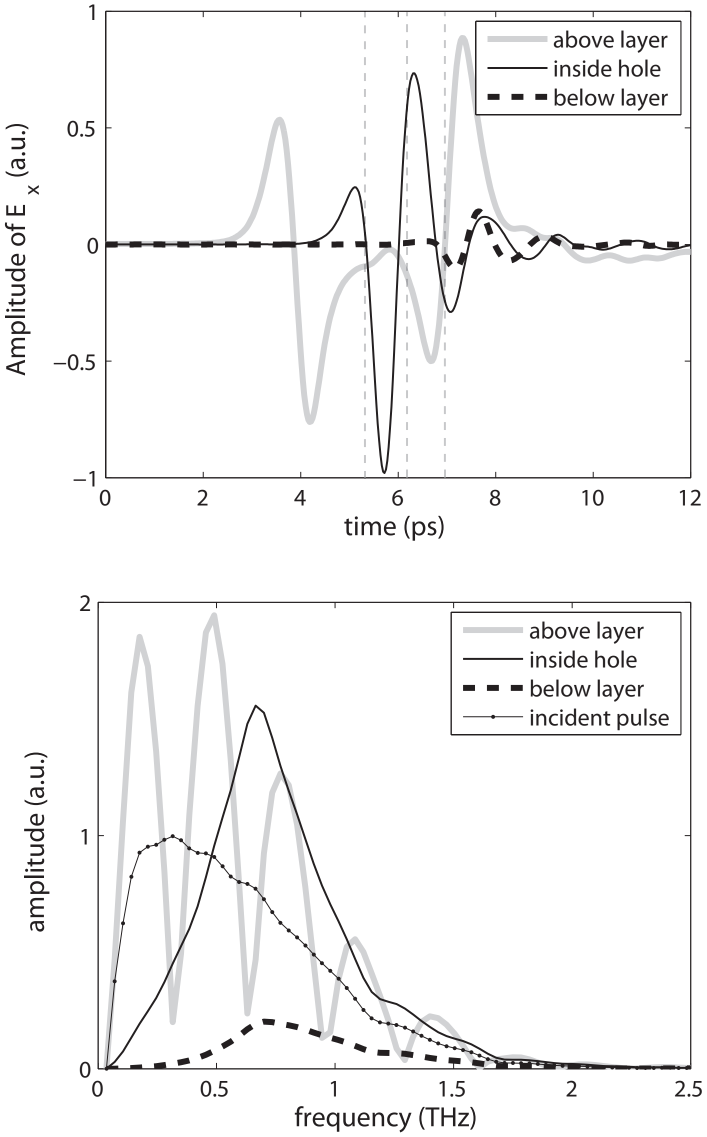

Figure 3.3: The amplitude of the y-component of the electric field as a function of time (top) and frequency (bottom), for a THz pulse incident on a square hole with size 200 μm in a layer with a thickness of 80 μm. The points at which these values are calculated are denoted by the crosses in Figure 3.2 on the facing page, upper right figure (z at 500, 0 and $-500\,\mu$m). In the frequency plot, also the spectrum of the incident pulse is shown.

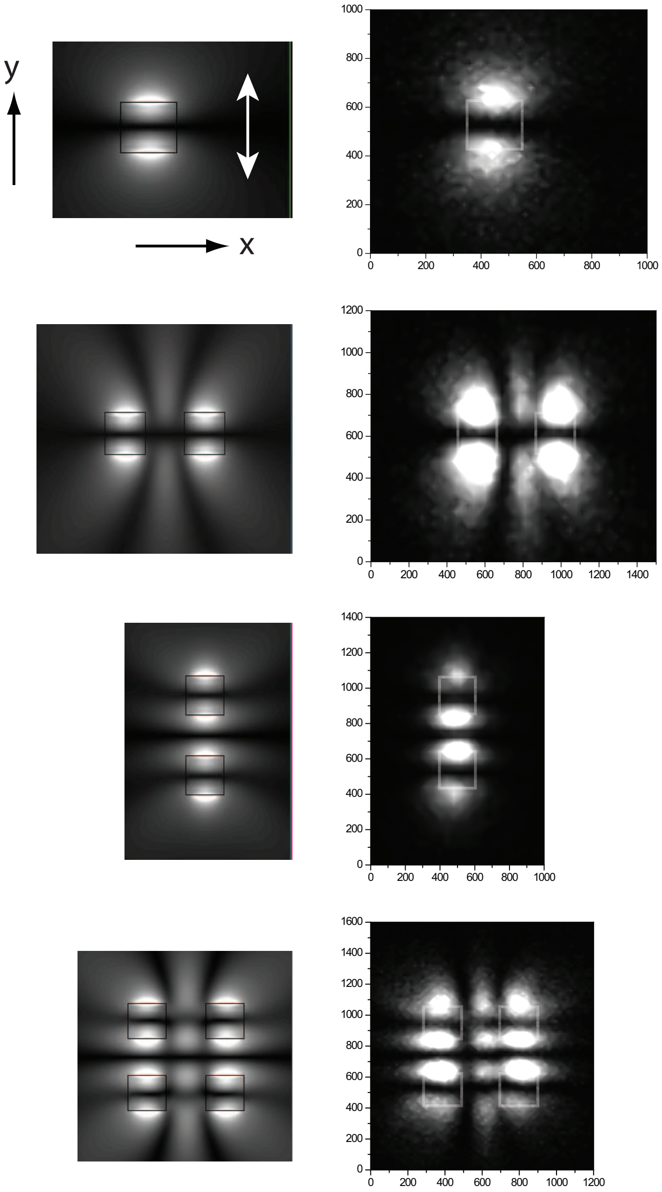

Figure 3.4: Gray-scale plots of measurements (right column) and calculations (left column) of the z-component of the electric field in the (x, y)-plane, on the shadow side of a layer with a thickness of 80 μm with one, two or four square holes of size 200 μm. The distance between the holes (center to center) is 400 μm. Data is for a single frequency: 1 THz. White denotes maximum amplitude and black means zero amplitude. The incident field is linearly polarized; the electric field points along the arrow depicted in the upper left figure.

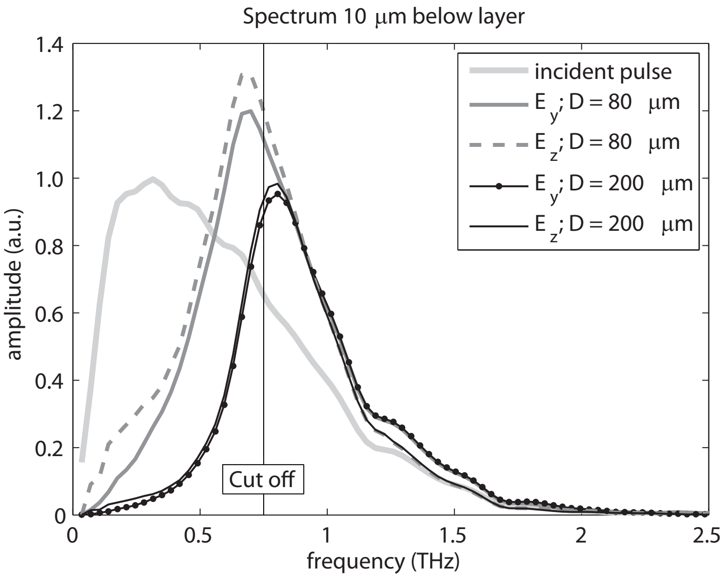

Figure 3.5: Calculated spectrum of the scattered field of a THz pulse, at the shadow side of a perfectly conducting layer with a single, square hole, at a distance of 10 μm below the layer. Size of the hole is 200 μm and the thickness of the layer is either 80 μm or 200 μm. The incident field is linearly polarized in the y-direction. Spectra are shown of the incident pulse, as well as of the y-component (taken at the projected center of the hole) and the z-component (taken at the projected edge of the hole) of the electric field.

smaller than the center to center distance between neighboring holes. Although gray-scale figures like these do not allow for a quantitative comparison between the calculation and the measurements, it is clear that the qualitative agreement is excellent.

Figure 3.5 and Figure 3.6 on the following page show the calculated and measured spectra, respectively, of E_y and E_z at the shadow side of a single hole. The spectra of the incident pulses are also given. Results are shown for a layer of 80 μm and 200 μm thickness. Spectra for the y-component of the electric field are taken at the projected center of the hole and spectra for the z-component of the electric field are taken at the projected edge of the hole, as indicated by the crosses in Figure 3.7, at a distance of 10 μm below the layer. The cutoff frequency of a $200 \times 200\,\mu\text{m}^2$ hole is 0.75 THz (or a wavelength of 400 μm), as indicated by the vertical lines. For the calculations as well as for the measurements, the peak amplitude of the transmitted field is just below cutoff for a layer thickness of 80 μm and just above cutoff for a thickness of 200 μm. Also, it is clear that the thicker metal filters the lower frequencies better than the thinner metal, as is expected because the modes below cutoff are exponentially decaying in the z-direction. Another feature that both the measurements and the calculations show, is that the ampli-

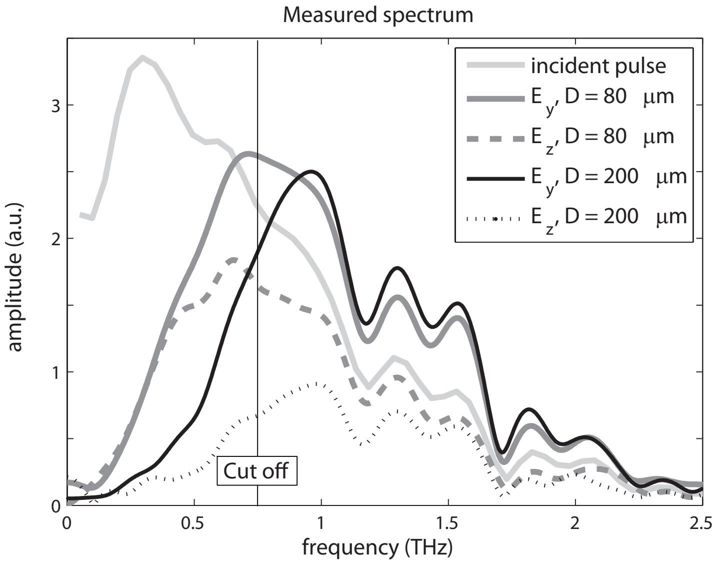

Figure 3.6: Measured spectrum of the scattered field of a THz pulse, at the shadow side of a aluminum layer with a single, square hole. Size of the hole is 200 μm and the thickness of the layer is either 80 μm or 200 μm. The incident field is linearly polarized in the y-direction. Spectra are shown for the incident pulse, as well as for the y-component (taken at the projected center of the hole) and z-component (taken at the projected edge of the hole) of the electric field. The scales for incident pulse and the y-component of the electric field are the same, but different from the scale of the z-component of the electric field.

tudes of the transmitted frequencies above cutoff are larger than the amplitudes of the corresponding frequencies in the incident field. Furthermore, considering the difference between the spectra for the y and the z-component, we observe an increase in the transmitted spectrum around 0.2 THz for E_z as compared to E_y for the calculations. For the measurements, this is not immediately obvious, because the scales for the y and z-component are not the same. However, the transmitted spectrum does indeed show a bump around 0.4 and 0.3 THz for 80 μm and 200 μm thickness, respectively, for the z-component. Apparently, these low frequencies tend to escape from the hole mainly in the directions along the interface.

Figure 3.7 on the next page shows the amplitude of the three components of the electric field at a frequency of 0.7 THz. The setup is the same as for Figures 3.5 and 3.6. The top row shows the calculations and the lower row the measurements. For the x-component the difference between the calculation and the measurement is the largest. Both figures show four lobes near the edges of the hole, but for the measurements, the lower left and upper right lobe seem connected. However, an asymmetry like that is not expected for a symmetric setup as we have here. An explanation could be that the electro-optic crystal was not perfectly aligned, such that, apart from a x-component, also an y-component was measured. Qual-

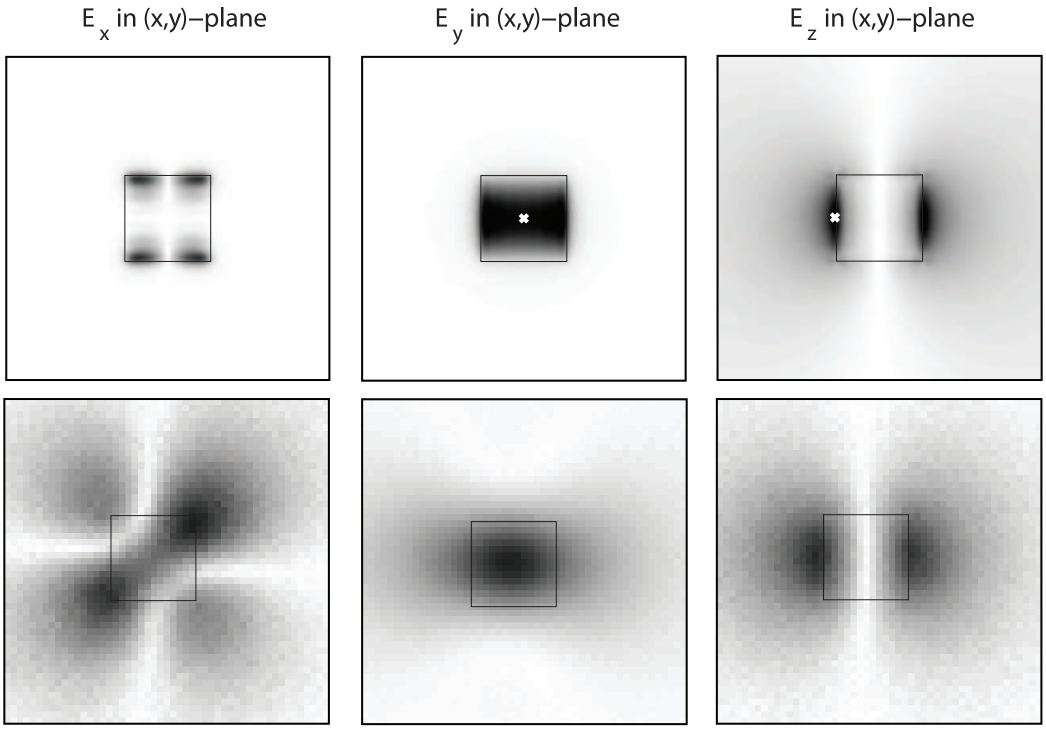

Figure 3.7: Gray scale figure of the x, y and z-components of the amplitude of the electric field at a frequency of 0.7 THz. White means zero amplitude and black means maximum amplitude. The figures are all normalized separately. The top row shows results from calculations, the bottom row are measurements. The metal layer has a thickness of 80 μm and the size of the hole is 200 μm. The calculations were done in the (x, y)-plane at 10 μm below the layer, at the shadow side. The white crosses in the upper left and upper right figure denote the position at which the spectra of Figure 3.5 and 3.6 are taken.

itatively, the calculations agree with the measurements, although the features are smaller for the calculations than for the measurements. Probably the air gap between the metal foil and the electro-optic crystal is larger than 10 μm. Furthermore, the measured terahertz electric field is not the electric field in a point, but, rather, proportional to the electric field that is integrated over a volume, as stated in the introduction.

Because the deviations between experiment and theory are small, the results in this section show that we can have confidence in the mode expansion theory and its implementation.

Chapter 4

Transmission of energy through multiple holes

4.1 Introduction

Recently, the transmission of electromagnetic energy through small holes in metal layers have received a lot of attention. In the past, the scattering from a single, sub-wavelength, circular hole in a conducting metal layer was already modeled in the 1940s and 1950s [10, 18–21]. Apart from the assumption that the metal is perfectly conducting, the metal layer was also assumed to be infinitely thin; these assumptions made it possible to calculate the diffraction analytically. To explain the so-called enhanced transmission through sub-wavelength hole arrays, as first reported in reference [22] in 1998, these assumptions are probably not justified. It is believed that the excitation of surface plasmons by neighboring holes plays an important role in the enhanced transmission.

To model this collective effect and to determine its importance, a lot of geometries have been studied and a lot of methods have been used. To name just a few: infinitely long, single slits [23, 24] and double slits [25] in metals with finite conductivity were modeled with the Green's function approach; coupled-wave analysis has been used to study gratings of slits (see, for example, [26–28]); gratings that are periodic in two dimensions were studied with a modal method [29] and with the finite-difference time-domain method [30]; the modal method [13] and the boundary element method [31] were used for a single rectangular hole in a perfect conductor.

However, the specific case of two holes and their mutual interaction has not received much attention. This is remarkable, because it is a fundamental system and building block of a hole array. Yet, especially when the two holes are a wavelength or more apart, as the corresponding computational domain is then also large, this system is not easy to calculate.

For two-dimensional structures, such as infinite slits or circular symmetric setups, or for periodic systems in which the computational domain is only as large as one unit cell, current computer power suffices to obtain acceptable accuracy. For a finite number of three-dimensional holes that are far apart, however, a clever computational scheme is needed to prevent computation times of days or even weeks.

In this chapter, we use our mode expansion method that was described in Chapter 2 to calculate the transmission through one, two and three holes. We determine the influence that a second and third hole have on the transmission through the first. Parameters such as size of the hole, distance between two holes and thickness of the conducting layer are varied.

For the modal method that we use, the perfect conductor assumption is essential. Hence, our method is of quantitative value when the imaginary part of the index of refraction is so large, that the skin depth of the metal is small compared to the typical length scales of the geometry. This is for example the case in the terahertz and microwave frequency regimes, where also a lot of research is done in subwavelength hole arrays [32, 33]. However, we stress that, apart from absorption of energy in the metal, all relevant physics is present in our model. That also includes the surface plasmon equivalent of a perfect conductor: an electromagnetic surface wave. Thus, the understanding we gain from our results will also help us to understand extraordinary transmission in the optical regime.

For all calculations, we took into account a number of 440 waveguide modes, such that the relative error in the electromagnetic energy in the holes or pits (Equation (2.45)) is less than 1 percent. All holes and pits are square ($L_x = L_y = L$) and the index of refraction above and below the layer as well as inside the pits and holes is taken to be unity.

In the following we (among other things) calculate the energy flux through a hole for various setups. This energy flux through a plane with $z = z_0$ is calculated directly from the coefficients of the waveguide modes in the following way:

$$\iint\limits_{\Omega_p} S_z \,\mathrm{d}x\,\mathrm{d}y = \sum_{\bar{\boldsymbol{\alpha}}} \sum_{\alpha_4} \sum_{\alpha'_4} \tfrac{1}{2} \,\mathrm{Re}\left[a_{\bar{\boldsymbol{\alpha}}}^{\alpha_4} \, a_{\bar{\boldsymbol{\alpha}}}^{\alpha'_4 *} \, \eta_{\bar{\boldsymbol{\alpha}}}^{\alpha_4}(z_0) \, \zeta_{\bar{\boldsymbol{\alpha}}}^{\alpha'_4}(z_0)^* \right], \tag{4.1}$$

where α_4 denotes the direction of propagation of the waveguide mode. Note that two waveguide modes that have an opposite direction of propagation but that are otherwise identical together produce a non-zero energy flux. This is not only true for propagating waveguide modes, but also for evanescent waveguide modes. In quantum mechanics, this phenomenon is called *tunneling*. It is an effect of the nonlinearity of the Poynting vector.

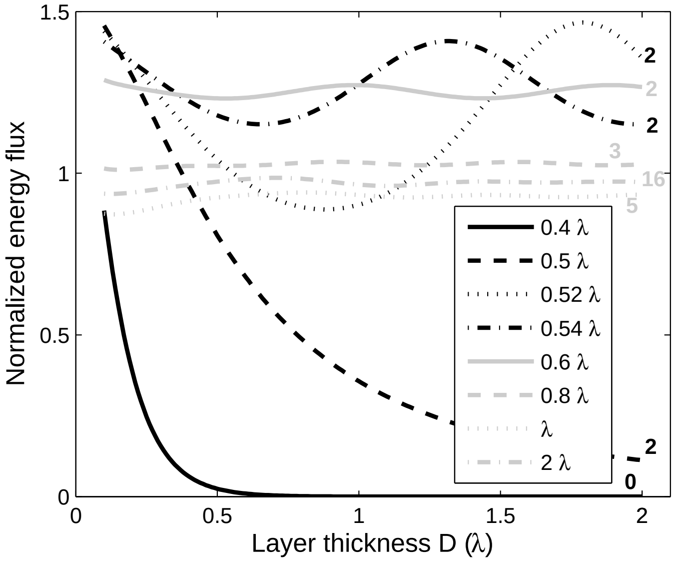

Figure 4.1: Energy flux through single hole as a function of layer thickness, normalized by the energy that is incident on the area of the hole. The incident field is a perpendicular, linearly polarized plane wave, with its polarization parallel to an edge of the hole. The hole is square: $L_x = L_y = L$ with different values of L for every curve, as listed in the legend. The number at the right of each curve is the number of waveguide modes above cutoff.

4.2 Extraordinary transmission through a single hole

Figure 4.1 shows the energy flux through a single hole as a function of the layer thickness. The energy flux is normalized by the energy that is incident on the area of the hole (the scalar optics normalization). Results are shown for various sizes of the hole. For sizes where all waveguide modes are below or at cutoff, the amount of energy coming through the hole decreases exponentially with the layer thickness, as expected. When the lowest order modes are just above cutoff a strong modulation of the energy flux with layer thickness is seen. The period of this modulation is half of the effective wavelength ($2\pi/\gamma_z$) of the propagating mode, indicating that the interference of this mode with its own reflection is responsible for the increased and decreased transmission. See the tables in Appendix B for the propagation constants of the various modes. It follows from Figure 4.1 that if the lowest order mode is just above cutoff, extraordinary transmission of a factor of about 1.5 seems possible. If the size of the hole is increased further, more and more modes are propagating and the normalized energy flux decreases below unity. Going from $L = \lambda$ to $L = 2\lambda$, the energy flux increases to just below unity. For large holes, one expects an energy flux of unity, of course. The energy flux that is shown, is calculated directly from the coefficients found for the waveguide

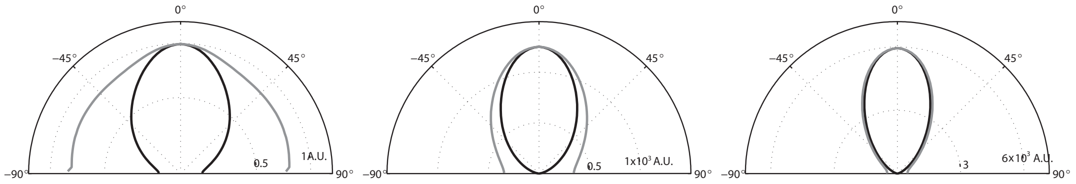

(a) $L_x = L_y = 0.2\lambda$ **(b)** $L_x = L_y = 0.6\lambda$ **(c)** $L_x = L_y = \lambda$

Figure 4.2: Polar plot of the near field scattering from a single square pit with a depth $d = \lambda/4$. For different sizes, the Poynting vector in the radial direction is shown, at a half circle with radius λ, with its x and y-coordinate coinciding with the center of the pit, and $z = D/2$, which is the upper interface. Black line is for the (y,z)-plane, gray for the (x,z)-plane. Incident field is a perpendicular plane wave, with its electric field linearly polarized along the x-direction. The radial scale is arbitrary, but equal for all three figures.

modes and hence, it is not necessarily the energy that will travel along the z-axis and, possibly, arrive at a far field detector. A part of this energy might travel along the interface. However, because of the perfect conductor assumption, none of this energy is absorbed.

Figure 4.2 gives information on the direction along which most energy is scattered. It shows polar plots of the energy, scattered from a single pit with a depth of $\lambda/4$. Shown is the Poynting vector in the radial direction along a half circle with radius of one wavelength, hence the scattering in the near field. The scattering in the plane in which the incident electric field is polarized can be non-zero along the interface, because the corresponding electric field then points in the z-direction. This is an electromagnetic surface wave. The scattering in the perpendicular plane can not be along the z-direction, for the tangential field at a perfect conductor must be zero. For a pit with size $L = \lambda/5$ the scattering is like that of a dipole, whereas for larger pits the scattering is mainly along the optical axis (the z-axis).

4.3 Extraordinary transmission through two and three holes

In Figure 4.3 on the facing page, we show the effect that the presence of a second and third hole or pit has on the energy flux through the first hole, as calculated with Equation (4.1). As a function of the distance between the centers of the two or three scatterers, the energy flux through one hole is calculated. This energy flux is normalized by the energy flux through an identical, but single hole. With this special normalization, we are able to isolate the effect that the presence of the second and third scatterer have on the transmission through the first. The incident field

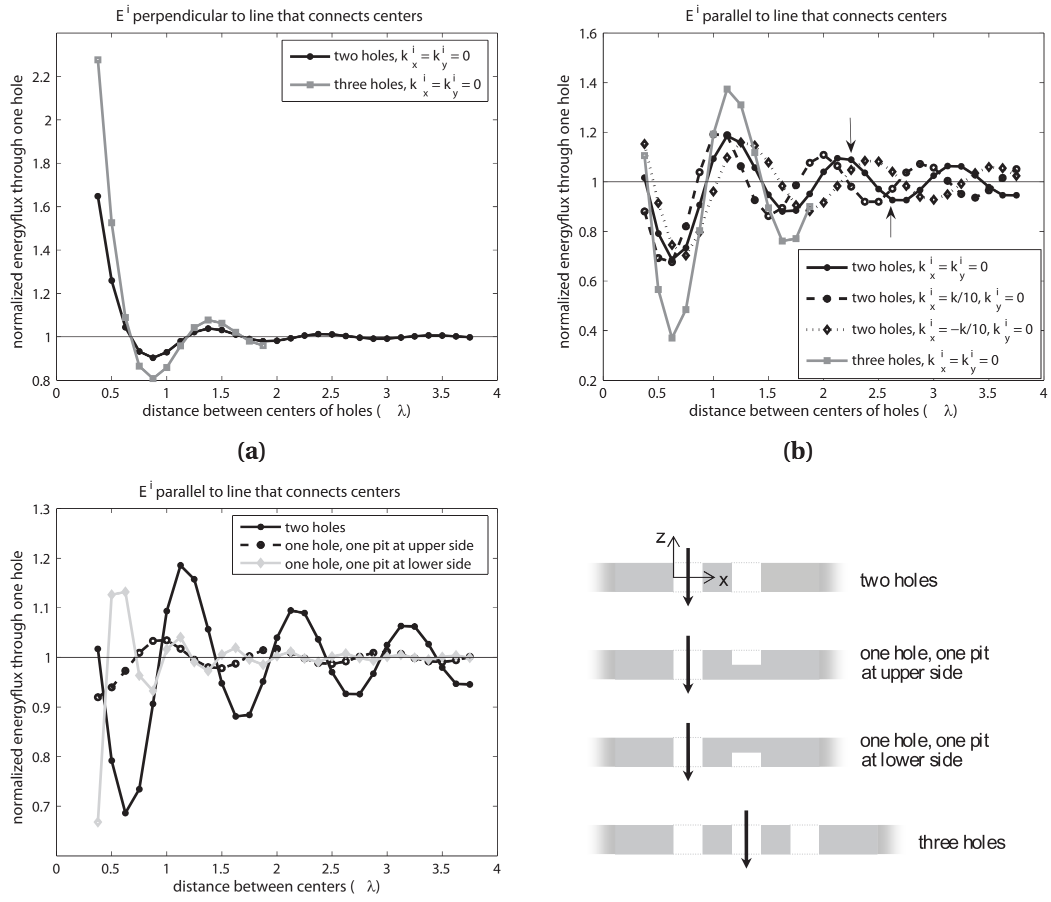

(a) **(b)**

(c) **(d)**

Figure 4.3: Energy flux through a hole, normalized by the energy flux through an identical single hole, as a function of the distance between two holes (or one hole and one pit). Pits and holes are all square, with $L_x = L_y = L = \lambda/4$. Incident field is a linearly polarized plane wave, with polarization as stated at the top of the figures. Incidence is always perpendicular, except for the dashed and dotted lines in Figure 4.3(b). Here, $k_x^i \neq 0$ means that the plane of incidence is the (x, z)-plane. Figure 4.3(d) shows cross-sections of the four used geometries. The bold arrows denote where the energy flux is calculated. The thickness of the layer is $\lambda/2$ and the depth of the pits is $\lambda/4$.

is again a linearly polarized plane wave. To distinguish the two basic directions of polarization we define a reference plane through the line that connects the centers of the scatterers and the z-axis. The electric field of the incident plane wave is either directed perpendicular to this plane or else parallel to this plane. Figure 4.3(a) shows the normalized energy flux through one of two holes and through one of three holes for perpendicular polarization. A modulation of the energy flux as a function of distance between the centers of the holes only occurs for holes that are less than two wavelengths apart. We believe that enhanced or decreased transmission in this case is caused by the coupling of evanescent fields scattered from one hole to the other and/or by polarization rotation at the corners of the hole. The solid lines in Figure 4.3(b) show the same calculations, but now for parallel polarization. The modulation of the energy flux is now also present for large distances between the holes. Its period is equal to the wavelength of the incident field. Its amplitude for three holes is twice the amplitude for two holes. Furthermore, the amplitude is proportional to the inverse of the distance between the centers of the holes, as expected for a cylindrical wave. If the propagation direction of the incident plane wave is slightly tilted (dashed and dotted line in Figure 4.3(b)) then a phase shift occurs that is equal to the delay that the incident field experiences in reaching the farthest hole as compared to the nearest hole. Figure 4.3(c) shows, for the incident field polarized parallel, the normalized energy flux through a hole in the presence of a pit. This pit has its open end at the upper side (dashed, black line) or at the lower side (solid, gray line). The field is incident from above. The modulation period for the a pit at the lower side is half of the period for a pit at the upper side. Furthermore, the amplitude for both cases is much smaller than for the case of two holes (solid, black line).

Figure 4.4 on the next page shows a comparison of the usual scalar optics normalization, where the transmission is normalized by the energy that is incident on the area of the hole, with the normalization used in Figure 4.3. The setup is two square holes, at varying distance of each other. The incident field is a parallel incident plane wave. Shown is, again, the transmission through one of these two holes. The transmission, when normalized by the transmission through an identical but single hole, always varies around unity. Hence, the presence of the second hole can lead to an increase as well as a decrease in transmission. However, when the scalar optics normalization is used, we already know from Figure 4.1 that the layer thickness has an influence on the transmission. This influence is of another nature. For holes that are so small that all modes are evanescent (shown in black), the transmission decreases exponentially with layer thickness. When the size of the holes is such that at least one mode is propagating (shown in gray) the Fabry-Perot effect can cause enhanced transmission for a single hole.

We think that, for the cases in which the incident electric field is polarized parallel to the reference plane, the enhanced and reduced transmission that occurs when the single hole normalization is used, is mainly caused by waves with $k_z = 0$

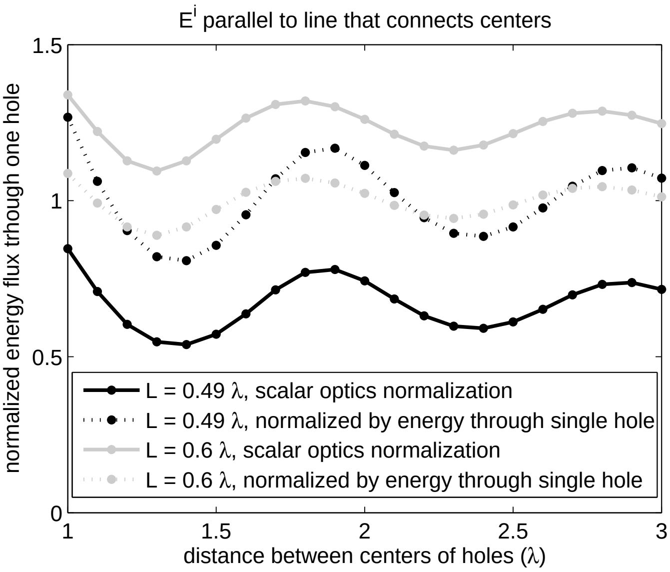

Figure 4.4: Comparison between the scalar optics normalization (solid line) and the single hole normalization (dashed line). The vertical axis shows the energy flux through one of two holes, the horizontal axis the distance between the centers of the two holes. The holes are square, with $L = 0.49\lambda$ (black) and $L = 0.6\lambda$ (gray). The thickness of the conducting layer is $\lambda/2$.

that are scattered along the metal surface. These scattered waves cause a periodicity of a wavelength when two scatterers at the same side of the metal layer contribute and a periodicity of half the wavelength when there is only one source, as is the case when one hole is accompanied by a pit with its open end at the non-illuminated side. In this case, the surface wave that is excited at the exit of the hole travels to the pit. It there excites another surface wave that travels back to the hole and interferes. This results in a phase shift that corresponds to twice the distance between the hole and the pit. See also reference [25]. The doubling of the amplitude for three holes as compared to two holes also fits nicely in the picture of the interfering surface waves.

Chapter 5

Angular momentum and topological charge

5.1 Introduction

In the previous chapter, we studied the transmission of energy through holes. In this chapter we will look at the transmission of angular momentum. Hence, in the previous chapter we calculated the Poynting vector **S** and in this chapter we will focus on the time averaged angular momentum flux tensor $\overleftrightarrow{\mathbf{K}}$, for time-harmonic fields given by:

$$\overleftrightarrow{\mathbf{K}} = \mathbf{r} \times \overleftrightarrow{\mathbf{T}}, \tag{5.1}$$

with **r** the coordinate vector from the reference point and $\overleftrightarrow{\mathbf{T}}$ the momentum flux tensor, whose components are given by:

$$T_{\alpha\beta} = \tfrac{1}{2}\,\mathrm{Re}\left[\left(\frac{\varepsilon_0\varepsilon}{2}\,|\mathbf{E}|^2 + \frac{\mu_0}{2}\,|\mathbf{H}|^2\right)\delta_{\alpha\beta} - \varepsilon_0\varepsilon\,E_\alpha E_\beta^* - \mu_0\,H_\alpha H_\beta^*\right]. \tag{5.2}$$

For studying the transmission of energy flux, we had a plane wave as incident field. Now we will use a beam as an incident field. For the x-component of the electric field of the beam we take a Laguerre-Gaussian mode. This mode is a solution of the paraxial wave equation in cylindrical coordinates (r, φ, z)

$$x = r\cos\varphi, \tag{5.3a}$$

$$y = r\sin\varphi. \tag{5.3b}$$

The mode is characterized by two integers m and p. The index m is the azimuthal mode index and $p \geq 0$ is the radial mode index. We let the focus of the field of the Laguerre-Gauss coincide with the upper interface of the conducting layer $z = D/2$. The x-component of the electric field is then proportional to [34]:

$$E_x^{m,p}(r,\varphi,D/2) \propto r^m\, L_p^m\left(\frac{kr^2}{b}\right) e^{-\frac{kr^2}{2b}}\, e^{im\varphi}, \tag{5.4}$$

with k the local wavenumber. The parameter b determines the beam waist. The function L_p^m is the associated Laguerre polynomial. The first exponential factor is responsible for the finite extend of the beam in the radial direction. For $|m| > 0$, the second exponential factor gives the field a so-called phase singularity at $r = 0$.

A phase singularity occurs for a certain electric field component when the amplitude of that component is zero. The phase is then undefined. Integrating the phase of E_x around a path that encloses the point $r = 0$ in a plane that is perpendicular to the z-axis, yields $2m\pi$, where the integer m is called the topological charge of the beam. The points that have a phase singularity together form a line in space. This line may be curved. The total topological charge of a field in a plane is a conserved quantity, as can be proved by degree theory [35]. In words, the property of conservation of topological charge implies the following. We seek all points (x_0, y_0) in a region $\Omega \in \mathbb{R}^2$ that are mapped on the point $(0,0)$ in $\mathbb{C}^2$ and we determine the total topological charge of this region. Hence, the complex electric field component in these points is equal to zero and the total topological charge is calculated by integrating the phase around each point and summing all contributions. Now, the conservation of topological charge states that if these points (x_0, y_0) do not lie on the boundary of the domain Ω, then the total topological charge in Ω is stable with respect to any continuous change of some kind of parameter p. For example, we can choose Ω to be the (x, y)-plane and the parameter equal to the z-coordinate: $p = z$. Then for any continuous change of the parameter z, the total topological charge in Ω will not change or else a zero has disappeared through the boundary of Ω. The individual zeros are unstable: they can change position inside Ω with changing p. Within the boundary of Ω, they can also emerge or disappear for certain values of p, but this can happen only in pairs of zeros that have opposite charge. Otherwise the conservation of topological charge would be violated.

A Laguerre-Gauss beam with $|m| > 0$ has a helical phase front. The sign of m gives the handedness of the helical phase front. The Poynting vector is perpendicular to the wavefront and, thus, has a nonzero component in the azimuthal direction. Therefore, a Laguerre-Gauss beam with $|m| > 0$ has angular momentum with respect to the axis $r = 0$. Because the energy is spiraling around this axis, the Laguerre-Gauss beam is said to have an optical vortex at its center [36].

In this chapter, a Laguerre-Gauss beam is incident on a square hole in a perfectly conducting layer. We will study the angular momentum of the beam and the topological charge. The parameters that are changed are the thickness of the layer and the width of the hole.

The x-component of the incident electric field is given by Equation (5.4), and we impose that the y-component is zero everywhere in the plane $z = D/2$. We use the

Fourier transform with respect to k_x and k_y to expand E_x in plane waves:

$$E_x(x,y,D/2) = \frac{1}{4\pi^2} \iint \hat{E}_x(k_x,k_y,D/2)\, e^{i(k_x x + k_y y)}\, \mathrm{d}x\, \mathrm{d}y, \tag{5.5}$$

with

$$\hat{E}_x(k_x,k_y,D/2) = \iint E_x(x,y,D/2)\, e^{-i(k_x x + k_y y)}\, \mathrm{d}k_x\, \mathrm{d}k_y. \tag{5.6}$$

Then, the z-component of the incident electric field follows easily from Maxwell's equation $\nabla \cdot \mathbf{E} = 0$ for plane waves, which is $\mathbf{k} \cdot \mathbf{E} = 0$. The incident magnetic field can be derived from Maxwell's equation $\nabla \times \mathbf{E} = i\omega\mu_0\mathbf{H}$ for plane waves, which gives $\mathbf{H} = \frac{\mathbf{k}}{\omega\mu_0} \times \mathbf{E}$. We represent the incident beam by 800 plane waves.

5.2 Optical vortices

Figure 5.1 on the following page shows the amplitude and phase of the x-component of the electric field, in the (x,y)-plane. The x-component of the electric field of the incident beam is a Laguerre-Gaussian mode with $(m,p) = (1,0)$. This means that E_x is zero at the beam axis and the phase increases in the counter-clockwise direction. The y-component of the incident electric field is zero. The beam is incident on a square hole in a layer with thickness λ. The beam axis coincides with the center of the hole. Results are shown for four sizes of the hole, as indicated in the captions. The parameter b, that determines the beam waist in the Laguerre-Gaussian mode (5.4) is chosen to be $2\pi\lambda$. For this value, the beam fits well within the hole of width 6λ. The iso-phase lines point radially outward.[1] For a hole width of 4λ (Figure 5.1(b)) the beam is influenced more by the hole and the iso-phase lines curl more near the wall of the hole. Still, the phase increases in the counter-clockwise direction. When the width of the hole is 2λ, E_x is zero at three points instead of one.[2] The phase of the vortex in the center now increases in the clockwise direction, while the phases of the two side vortices increase in the counter-clockwise direction. We will investigate this case in more detail below. For a hole width of λ only one vortex is present in the lower interface, whose phase increases in the clockwise direction, which is *inverted* with respect to the incident beam.

Figure 5.2 on page 55 shows the amplitude and phase of E_x for a hole with a width of 2λ and a layer thickness of λ. The field is shown in the (x,y)-plane, for various

---

[1] Among the iso-phase lines, there is always one that is thicker than the others. This is a numerical artifact. The phase is defined between $\varphi = -\pi$ and $\varphi = \pi$. Because the numerical program can not handle multivalued functions, between $+\pi$ and $-\pi$ all intermediate phases are drawn. These together form a thick line.

[2] As is clear from Figure 5.1, E_x is not only zero at the phase singularities, but also at the perfectly conducting wall for the case that this wall is parallel to the x-axis.

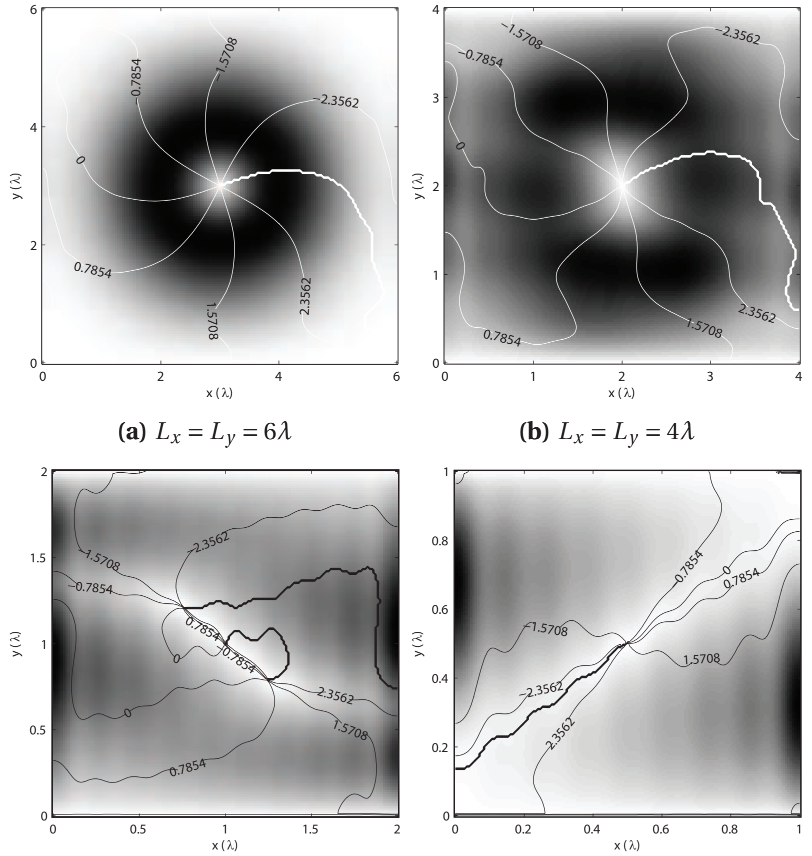

(a) $L_x = L_y = 6\lambda$ **(b)** $L_x = L_y = 4\lambda$

(c) $L_x = L_y = 2\lambda$ **(d)** $L_x = L_y = \lambda$

Figure 5.1: Gray scale figures of the amplitude of the x-component of the electric field, inside a square hole, for four sizes of the hole. White means zero amplitude, black means maximum amplitude. The size of the hole is given in the captions. The thickness of the layer is λ for all figures. The plane in which the field is given is the (x, y)-plane with $z = -D/2$, which is the lower interface. The white or black isolines indicate the phase of E_x, in radians. The E_x of the incident field is a Laguerre-Gaussian beam with $(m, p) = (1, 0)$.

values of the z-coordinate, all within the hole. The circular arrows denote the direction in which the phase is increasing. Going from $z = 0.4\lambda$ to $z = 0.3\lambda$, two vortices move out of the hole area (as indicated by the gray arrows). A careful study (not shown here) shows that these vortices move out via the wall that is parallel to the y-axis. From $z = 0.3\lambda$ to $z = 0.2\lambda$, two vortices appear from the walls. They move around until $z = -0.2\lambda$ and then leave the hole area via the wall. According to Degree Theory, the total topological charge in a two-dimensional domain can only change, as a function of the parameter z, if the vortices are crossing the boundaries of the domain. In our case, the walls of the hole are the boundaries,

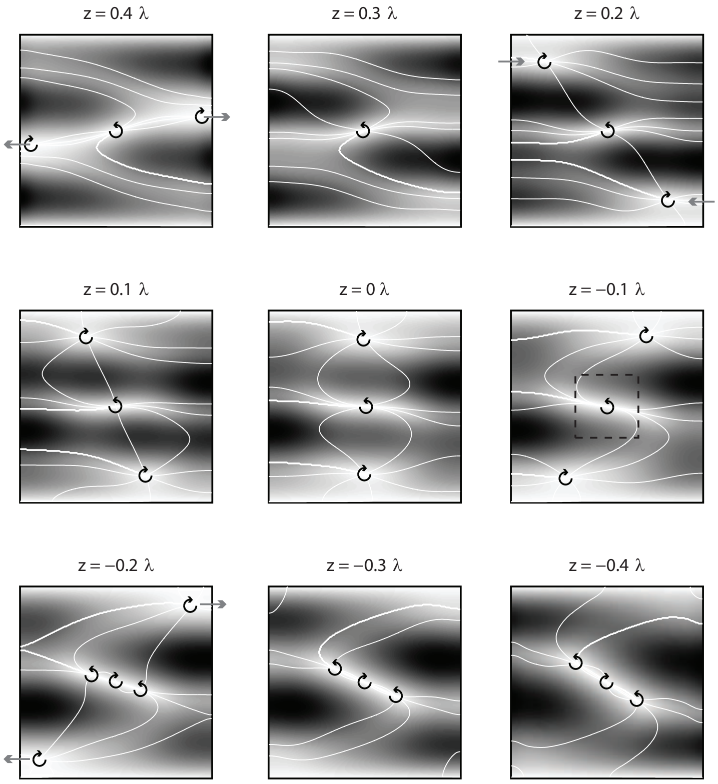

Figure 5.2: Gray scale figures of the amplitude of the x-component of the electric field, inside a square hole, with $L_x = L_y = 2\lambda$, for various (x, y)-planes. The z-coordinate is given at the top of each graph. White means zero amplitude, black means maximum amplitude. The thickness of the layer is λ. The isolines indicate the phase of E_x, with intervals of $\pi/4$. For each zero in the field, the arrow points in the direction of increasing phase. The E_x of the incident field is a Laguerre-Gaussian beam with $(m, p) = (1, 0)$.

and, indeed, the total topological charge for $z = 0.4\lambda$ is not the same as the total topological charge for $z = 0.3\lambda$. When z decreases from $z = -0.1\lambda$ to $z = -0.2\lambda$, two additional vortices appear and the handedness of the vortex at the center is changed. However, the total topological charge is not changed. In the next figure, this phenomenon is studied in more detail.

Figure 5.3(a) on the following page shows the dashed square of Figure 5.2 in more detail and for an additional number of z-coordinates. The iso-phase lines are now plotted in black and a standard phase unwrapping algorithm is used to show the exact location of the phase singularities. It is clear from the figures, for decreasing z, that the three phase singularities spring from the location where there was only one phase singularity. This phenomenon may be explained as follows. As is shown in Figure 5.3(b), a line of zero electric field strength can be curved such

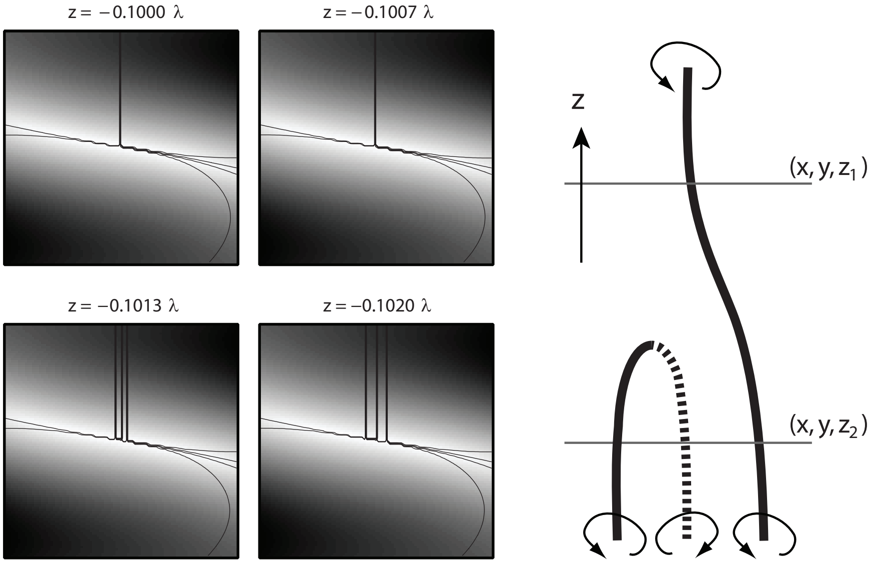

(a) **(b)**

Figure 5.3: (a): enlargement of dashed square in Figure 5.2, for four (x, y)-planes with closely spaced z-coordinate. (b): schematic view of the birth of a vortex pair.

that it skims a certain plane with constant z-coordinate. For larger z, the plane contains no vortices, while, for smaller z, the plane has two vortices with opposite handedness. When another vortex line is added, such as shown in the figure, a situation occurs in which the total topological charge is constant for all values of the z-coordinate, while the number of vortices changes from one to three.

5.3 The transmission of angular momentum

In Section 4.2 the transmission of energy through a single hole was studied. In this section we will examine the transmission of angular momentum through a single hole. We choose the incident beam such that its axis coincides with the center of the hole. This means that the angular momentum is determined with respect to the center of the hole. The angular momentum through a plane with constant z-coordinate has three components. However, because we choose the Laguerre-Gauss beam to have its axis parallel to the z-axis, only the component K_{zz} of the angular momentum flux tensor of the incident field is non-zero. In general, this component is given by:

$$K_{zz}(x, y, z) = r_x\, T_{yz}(x, y, z) - r_y\, T_{xz}(x, y, z), \tag{5.7}$$

with r_x (r_y) the x-component (y-component) of the vector that points from the center of the hole to the point (x, y, z) in which the angular momentum flux is evaluated. The components T_{xz} and T_{yz} of the momentum flux tensor are given by:

$$T_{xz} = -\tfrac{1}{2}\,\mathrm{Re}\left[\varepsilon_0\varepsilon E_x E_z^* + \mu_0 H_x H_z^*\right], \tag{5.8a}$$

$$T_{yz} = -\tfrac{1}{2}\,\mathrm{Re}\left[\varepsilon_0\varepsilon E_y E_z^* + \mu_0 H_y H_z^*\right]. \tag{5.8b}$$

To obtain the angular momentum that is transmitted through a hole, we integrate the angular momentum flux over the area of the hole, at the lower interface $z = -D/2$.

Inside the holes and pits, the electric and magnetic fields are sums of waveguide modes. A waveguide mode $\boldsymbol{\alpha}$ is TE or TM polarized and is propagating (or evanescent) in the positive or in the negative z-direction. With respect to the x and y-coordinate the waveguide mode is a trigonometric function, with spatial frequency given by the integer numbers m_x and m_y. Consequently, the angular momentum through the area of the hole yields an integral over a sum of trigonometric functions times another sum of trigonometric functions. This can be written as a sum of integrals over one waveguide mode $\boldsymbol{\alpha}$ times another waveguide mode $\tilde{\boldsymbol{\alpha}}$. For the calculation of the total energy through a hole, a similar result was obtained. In that case, all integrals over one waveguide mode $\boldsymbol{\alpha}$ with another $\tilde{\boldsymbol{\alpha}}$ are zero if $\tilde{m}_x \neq m_x$ or $\tilde{m}_y \neq m_y$. Hence, two modes with different spatial frequencies together do not give an energy flux. Furthermore, two modes with different polarization also give no energy flux. It turns out that, for the angular momentum, these cross terms can give a non-zero contribution, even for modes with different polarization. To give an example: for $\tilde{m}_x = m_x$ and $\tilde{m}_y = m_y \pm 1, m_y \pm 3, m_y \pm 5, \ldots$ the contribution of the angular momentum is non-zero.

Another difference between the energy and angular momentum should be noted here. The perfectly conducting layer can not absorb energy. The term $\mathbf{E}\cdot\mathbf{J}^*$ in the energy conservation law (1.16a) is zero. However, angular momentum can be transferred to the perfectly conducting layer: in general, the term $\rho\mathbf{E}^* + \mu_0\mathbf{J}\times\mathbf{H}^*$ in the angular momentum conservation law (1.16c) is nonzero. Hence, whereas the amount of energy that flows into a hole is equal to the amount of energy that flows out of the hole, the amount of angular momentum leaving the hole may not be equal to the amount of angular momentum entering the hole. The difference is then transferred to the charges and currents at the surface of the perfect conductor.

Figure 5.4 on the next page shows the transmission of the zz-component of angular momentum through a square hole, as a function of the layer thickness. The angular momentum is normalized by the angular momentum that flows into the hole. As in the previous section, E_x is given by Equation (5.4) and E_y is zero. The axis of the beam coincides with the center of the hole and the beam waist parameter b is chosen to be $2\pi\lambda$. For a width of 4λ, the beam hardly interacts with the walls of the hole, such that all incident angular momentum is transmitted.

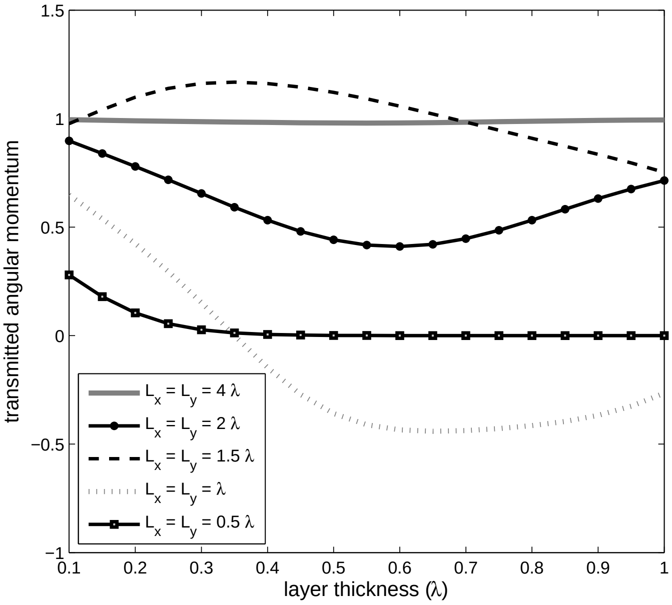

Figure 5.4: The angular momentum that is transmitted by a hole as a function of the thickness of the conducting layer, for various widths of the hole. The transmitted angular momentum is normalized by the angular momentum that flows into the hole. The E_x of the incident field is a Laguerre-Gaussian beam with $(m, p) = (1, 0)$. The axis of the beam coincides with the center of the hole, like in Figure 5.1(a).

In contrast, for a width of $\lambda/2$, no angular momentum is transmitted when the hole thickness is larger than 0.3λ. For this width, only the lowest order waveguide modes with $(m_x, m_y) = (1, 0)$ and $(0, 1)$ are propagating. However, these are not excited by the Laguerre-Gauss mode. The Laguerre-Gauss mode is zero at the center of the hole, where these lowest order modes are maximum. Although other modes that have a maximum at the center, such as the $(1, 1)$ mode, are excited, all of these are evanescent for this hole width. For a width of 2λ, the flow of angular momentum into the hole is larger than the flow out of the hole. For $3/2\lambda$ and a layer thickness around 0.4λ, the flow of angular momentum out of the hole is larger than what flows in. Finally, for a width of λ and a layer thickness larger than 0.35λ angular momentum flows in from the upper interface as well as the lower interface. This agrees with Figure 5.1(d), which shows that the handedness of the vortex at the lower interface is opposite with respect to the handedness of the incident beam.

Chapter 6

Mode expansion theory for a two-dimensional array

6.1 Introduction

In Chapter 2 we have treated the case of the scattering from a finite number of pits and holes. In this chapter, we adapt the mode expansion technique for the case of scattering from a periodic array of pits and holes.

We recall the setup: there is again a perfectly conducting metal layer with thickness D, perpendicular to the z-axis. Instead of a finite number of pits and holes, we now have a two-dimensional periodic array of identical unit cells. These unit cells make up a rectangular lattice with periodicity t_x in the x-direction and t_y in the y-direction. A unit cell contains a finite number of rectangular pits and holes. We assume that the origin of our x- and y-axis coincide with the lower left corner of the fundamental unit cell. The area of this unit cell is denoted by $\Omega_t = \left\{ (x, y) \,\middle|\, 0 < x < t_x,\, 0 < y < t_y \right\}$, see Figure 1.1 on page 15. Any translation over a vector

$$\mathbf{t_n} = n_x t_x \hat{\boldsymbol{\imath}}_x + n_y t_y \hat{\boldsymbol{\imath}}_y, \tag{6.1}$$

with n_x and n_y integers and $\hat{\boldsymbol{\imath}}_x$ and $\hat{\boldsymbol{\imath}}_y$ the unit vectors in the x- and y-direction, leaves the structure invariant.

It is possible, of course, to allow the unit cell to be tilted and leaning. Then, the two fundamental translation vectors are not parallel to the x- and y-axis, and, furthermore, are not mutually orthogonal. Although the mathematical expressions will then be somewhat lengthier, the physics is not substantially more difficult. See for example reference [37] for a discussion. Here, we will limit our discussion to a rectangular lattice, not rotated with respect to our cartesian axes.

The lattice vectors $t_x \hat{\boldsymbol{\imath}}_x$ and $t_y \hat{\boldsymbol{\imath}}_y$ have their reciprocal lattice vectors in Fourier space given by $u_x \hat{\boldsymbol{\imath}}_x$ and $u_y \hat{\boldsymbol{\imath}}_y$ with:

$$u_x = \frac{2\pi}{t_x}, \tag{6.2a}$$

$$u_y = \frac{2\pi}{t_y}. \tag{6.2b}$$

The convex hull of the reciprocal lattice vectors is the so-called Brillouin zone, which is the Fourier or reciprocal counterpart of the unit cell.

Suppose now that for our scattering problem, we have an incident plane wave in the upper half space with wave vector

$$\mathbf{k}^{\text{in}} = \left(k_x^{\text{in}}, k_y^{\text{in}}, -\sqrt{k_u^2 - \left(k_x^{\text{in}}\right)^2 - \left(k_y^{\text{in}}\right)^2} \right). \tag{6.3}$$

Then, because of the periodicity, the total electromagnetic field is quasi-periodic, which means that every field component f satisfies:

$$f(\mathbf{r} + \mathbf{t_n}) = e^{i\mathbf{k}^{\text{in}} \cdot \mathbf{t_n}} f(\mathbf{r}), \tag{6.4}$$

where $\mathbf{r}$ is of course the coordinate vector (x, y, z) and the translation vector $\mathbf{t_n}$ has no component in the z-direction. Hence, f can be expanded in a Fourier series:

$$f(x, y, z) = \sum_{\mathbf{k} \in \mathscr{U}^{\text{in}}} F(k_x, k_y, z) e^{i(k_x x + k_y y)}, \tag{6.5}$$

with the Fourier coefficient:

$$F(k_x, k_y, z) = \frac{1}{t_x t_y} \iint\limits_{\Omega_t} f(x, y, z)\, e^{-i(k_x x + k_y y)} \mathrm{d}x \mathrm{d}y, \tag{6.6}$$

with $\mathscr{U}^{\text{in}}$ the following set of transverse components of the wave vectors:

$$\mathscr{U}^{\text{in}} = \left\{ \mathbf{k}_\parallel = (k_x, k_y) \;\middle|\; k_x = k_x^{\text{in}} + n_x u_x,\ k_y = k_y^{\text{in}} + n_y u_y \right\}. \tag{6.7}$$

Hence, whereas in the previous non-periodic case, the electric and magnetic fields above and below the layer could be decomposed into a continuum of plane waves, now in the periodic case, the electromagnetic fields consist of an infinite sum over discrete directions. This is the mathematical background of the physical phenomenon of a grating that scatters the incident light only in discrete orders.

We will now review the mode expansion theory and point out the differences between the periodic and the non-periodic case.

6.2 Mode expansions

As before, we treat the half spaces $z > D/2$ and $z < D/2$ separately from the intermediate layer. We will see that the differences with the non-periodic case occur mainly in these upper and lower half spaces.

6.2.1 Inside the holes and pits

The field inside a pit or hole is expanded in propagating and evanescent waveguide modes:

$$\begin{bmatrix} \mathbf{E}^{\text{pit}}(\mathbf{r}) \\ \mathbf{H}^{\text{pit}}(\mathbf{r}) \end{bmatrix} = \sum_{\boldsymbol{\alpha}} a_{\boldsymbol{\alpha}} \begin{bmatrix} \mathbf{E}_{\boldsymbol{\alpha}}(\mathbf{r}) \\ \mathbf{H}_{\boldsymbol{\alpha}}(\mathbf{r}) \end{bmatrix}, \tag{6.8}$$

with $a_{\boldsymbol{\alpha}}$ the expansion coefficients. The index $\boldsymbol{\alpha}$ denotes the pit number (α_1), the polarization of the mode (α_2), its spatial frequency (α_3) and its direction of propagation (α_4). The waveguide modes and their normalization are identical to the non-periodic case. The quasi-periodicity, as described in Equation (6.4), implies that the expansion coefficient of a certain waveguide mode with the index $\boldsymbol{\alpha}'$ in a unit cell that is translated with respect to the fundamental unit cell by a translation vector $\mathbf{t}'_{\mathbf{n}}$ differs by a phase factor from the coefficient $\boldsymbol{\alpha}$ of the corresponding waveguide mode in the fundamental unit cell:

$$a_{\boldsymbol{\alpha}'} = e^{i\,\mathbf{k}^{\text{in}}\cdot\mathbf{t}'_{\mathbf{n}}}\, a_{\boldsymbol{\alpha}}. \tag{6.9}$$

Therefore, once we know the expansion coefficients of the waveguide modes inside the fundamental unit cell, the field inside every hole and pit is known.

6.2.2 Above and below the layer

The field in the upper and lower half spaces consists of the given incident field, the reflected field, and the field scattered by the periodic configuration of pits or holes. The incident field does not need to be restricted to a single plane wave. A continuum of incident spatial frequencies can simply be decomposed into plane waves and the calculation can be done for each plane wave separately. An improvement in efficiency can then be reached by decomposing the incident field not into single plane waves but in sets of plane waves that are each others orders with respect to the periodicity of the lattice. The calculation then only needs to be done for each of these sets. We will not incorporate this into the equations below. For an account of this the reader is referred to reference [38].

The scattered fields in the upper and lower half spaces are expanded in propagating and evanescent plane waves. The expansion now takes the form of an infinite sum instead of a continuum:

$$\begin{bmatrix} \mathbf{E}^{s}(\mathbf{r}) \\ \mathbf{H}^{s}(\mathbf{r}) \end{bmatrix} = \sum_{\boldsymbol{\beta}} b_{\boldsymbol{\beta}} \begin{bmatrix} \mathbf{E}_{\boldsymbol{\beta}}(\mathbf{r}) \\ \mathbf{H}_{\boldsymbol{\beta}}(\mathbf{r}) \end{bmatrix}, \tag{6.10}$$

with $b_{\boldsymbol{\beta}}$ the expansion coefficients. In the subscript $\boldsymbol{\beta} = (\beta_1, \beta_2)$ we have β_1 for the polarization and β_2 for the transverse part of the wave vector of the plane wave. The set of plane waves is discrete: $\beta_2 \in \mathscr{U}^{\text{in}}$.

We again use lower case letters to denote tangential fields and we split the plane waves into a part that depends on x and y and a part that depends on z:

$$\mathbf{e}_{\boldsymbol{\beta}}(x,y,z) = \boldsymbol{v}_{\boldsymbol{\beta}}(x,y)\,\eta_{\boldsymbol{\beta}}(z), \tag{6.11a}$$

$$\mathbf{h}_{\boldsymbol{\beta}}(x,y,z) = \boldsymbol{v}_{\boldsymbol{\beta}}(x,y)\,\zeta_{\boldsymbol{\beta}}(z). \tag{6.11b}$$

The normalization of the plane waves is given by:

$$\langle \boldsymbol{v}_{\boldsymbol{\beta}} | \boldsymbol{v}_{\boldsymbol{\beta}'} \rangle_{\Omega_t} \equiv \iint\limits_{\Omega_t} \left[v_{\boldsymbol{\beta},x}(x,y)\, v_{\boldsymbol{\beta}',x}(x,y)^* + v_{\boldsymbol{\beta},y}(x,y)\, v_{\boldsymbol{\beta}',y}(x,y)^* \right] \mathrm{d}x\,\mathrm{d}y = \delta_{\boldsymbol{\beta}\boldsymbol{\beta}'}, \tag{6.12}$$

with δ the Kronecker delta. Note that the integration is over the area of the unit cell, whereas in the non-periodic case the integration was over the entire (x,y)-plane. For a listing of the functions $\boldsymbol{v}_{\boldsymbol{\beta}}$, $\eta_{\boldsymbol{\beta}}$ and $\zeta_{\boldsymbol{\beta}}$ the reader is refered to Section 2.2.1 on page 26. The only difference is in the normalization constant $\Lambda_{\boldsymbol{\beta}}$, which is now given by:

$$\Lambda_{\boldsymbol{\beta}} = \left(t_x t_y\right)^{-1/2}, \tag{6.13}$$

with t_x and t_y the sizes of the unit cell.

The transverse magnetic field of the plane waves is related to the transverse electric field:

$$\mathbf{h}_{\boldsymbol{\beta}}(\mathbf{r}) = \frac{k_z}{\omega\mu_0}\mathbf{e}_{\boldsymbol{\beta}}(\mathbf{r}), \qquad \beta_1 = \mathrm{S}, \tag{6.14a}$$

$$\mathbf{h}_{\boldsymbol{\beta}}(\mathbf{r}) = \frac{\omega\varepsilon\varepsilon_0}{k_z}\mathbf{e}_{\boldsymbol{\beta}}(\mathbf{r}), \qquad \beta_1 = \mathrm{P}. \tag{6.14b}$$

However, for the special case that $k_z = 0$ and for P-polarization, we can not use this relation to calculate the magnetic field from the electric field. The transverse electric field of this plane wave is zero, because it is propagating along the interface. The order for which $k_z = 0$ is a so-called *grazing order* of the grating, on the border between propagating and evanescent. It is the electromagnetic surface wave, that we came across earlier.

Due to these grazing orders, we are now not able anymore to express the total transverse magnetic field in terms of the total transverse electric field. Therefore, we split the set of transverse wave vectors $\mathscr{U}^{\mathrm{in}}$ into a set $\mathscr{U}_0^{\mathrm{in}}$ that only contains the grazing wave vectors and its complementary set $\mathscr{U}_c^{\mathrm{in}}$:

$$\mathscr{U}_0^{\mathrm{in}} = \left\{ \mathbf{k}_\parallel \,\middle|\, k_x = k_x^{\mathrm{in}} + n_x u_x,\ k_y = k_y^{\mathrm{in}} + n_y u_y,\ k_x^2 + k_y^2 = k_u^2 \right\}, \tag{6.15a}$$

$$\mathscr{U}_c^{\mathrm{in}} = \mathscr{U}^{\mathrm{in}} \backslash \mathscr{U}_0^{\mathrm{in}}. \tag{6.15b}$$

A similar procedure is then followed for the set of plane waves:

$$\mathscr{B}_0 = \left\{ (\beta_1,\beta_2) \,\middle|\, \beta_1 = \mathrm{P},\ \beta_2 \in \mathscr{U}_0^{\mathrm{in}} \right\}, \tag{6.16a}$$

$$\mathscr{B}_c = \left\{ (\beta_1,\beta_2) \,\middle|\, \beta_1 = \mathrm{S} \text{ or } \mathrm{P},\ \beta_2 \in \mathscr{U}^{\mathrm{in}} \right\} \backslash \mathscr{B}_0, \tag{6.16b}$$

such that $\mathscr{B}_0$ is the set of P-polarized grazing plane waves and $\mathscr{B}_c$ is the set of all other plane waves. The scattered tangential electric and magnetic fields are then written as a sum over these two sets:

$$\mathbf{e}^s(\mathbf{r}) = \sum_{\boldsymbol{\beta}\in\mathscr{B}_0} b_{\boldsymbol{\beta}}\,\mathbf{e}_{\boldsymbol{\beta}}(\mathbf{r}) + \sum_{\boldsymbol{\beta}\in\mathscr{B}_c} b_{\boldsymbol{\beta}}\,\mathbf{e}_{\boldsymbol{\beta}}(\mathbf{r}) = \sum_{\boldsymbol{\beta}\in\mathscr{B}_c} b_{\boldsymbol{\beta}}\,\mathbf{e}_{\boldsymbol{\beta}}(\mathbf{r}), \tag{6.17a}$$

$$\mathbf{h}^s(\mathbf{r}) = \sum_{\boldsymbol{\beta}\in\mathscr{B}_0} b_{\boldsymbol{\beta}}\,\mathbf{h}_{\boldsymbol{\beta}}(\mathbf{r}) + \sum_{\boldsymbol{\beta}\in\mathscr{B}_c} b_{\boldsymbol{\beta}}\,\mathbf{h}_{\boldsymbol{\beta}}(\mathbf{r}), \tag{6.17b}$$

where, in fact, the electric field of the grazing orders is equal to zero.

In the non-periodic case, we defined an integral operator to map the scattered electric field onto the scattered magnetic field. See Equation (2.29) on page 25. The contribution of $k_z = 0$ to this integral over (k_x, k_y) has measure zero. Therefore taking special precautions for the case of grazing P-polarized waves is not necessary for the non-periodic case.

We now define an operator $\mathscr{A}$ that is not a integral operator but, instead, a summation operator. It maps any two-dimensional vector field $\mathbf{f} : \Omega_t \to \mathbb{C}^2$ onto another such vector field:

$$\mathscr{A}(\mathbf{f}) \equiv \sum_{\beta_2\in\mathscr{U}^{\mathrm{in}}} \frac{k_z}{\omega\mu_0} \left\langle \mathbf{f} \,\middle|\, \boldsymbol{v}^{\mathrm{S}}_{\beta_2} \right\rangle_{\Omega_t} \boldsymbol{v}^{\mathrm{S}}_{\beta_2} + \sum_{\beta_2\in\mathscr{U}^{\mathrm{in}}_c} \frac{\omega\varepsilon\varepsilon_0}{k_z} \left\langle \mathbf{f} \,\middle|\, \boldsymbol{v}^{\mathrm{P}}_{\beta_2} \right\rangle_{\Omega_t} \boldsymbol{v}^{\mathrm{P}}_{\beta_2}. \tag{6.18}$$

As the second summation is only over the non-grazing P-polarized plane waves, this operator is well-defined.

Similar to the non-periodic case, we use the operator $\mathscr{A}$ to express the scattered tangential magnetic field in terms of the scattered tangential electric field. In any plane z is constant and in particular in $z = \pm D/2$, we have:

$$\mathbf{h}^s(x, y, \pm D/2) - \sum_{\boldsymbol{\beta}\in\mathscr{B}_0} b_{\boldsymbol{\beta}}\,\mathbf{h}_{\boldsymbol{\beta}}(x, y, \pm D/2) = \mathscr{A}\left[\mathbf{e}^s(x, y, \pm D/2)\right]. \tag{6.19}$$

This equation holds for all (x, y) with $-\infty < x, y < \infty$. Comparing this expression to Equation (2.30) on page 26, we see that the tangential magnetic field of the grazing orders is subtracted from the scattered tangential magnetic field.

6.3 Matching at the interfaces

At the interfaces $z = \pm D/2$, the tangential electric and magnetic fields must of course be continuous. Because of the quasi-periodicity, it suffices to require that the tangential components are continuous in the part of $z = \pm D/2$ that is within the fundamental unit cell:

$$\mathbf{e}^{\mathrm{pit}} = \mathbf{e}^s, \qquad \forall (x, y) \in \Omega_t,\ z = \pm D/2, \tag{6.20a}$$

$$\mathbf{h}^{\mathrm{pit}} = \mathbf{h}^{\mathrm{in}} + \mathbf{h}^r + \mathbf{h}^s, \qquad (x, y) \in \bigcup_{\alpha_1} \left(\Omega_{\alpha_1} \cap \Omega_t\right),\ z = \pm D/2, \tag{6.20b}$$

where we have incorporated that the sum of the incident and reflected tangential electric field is zero at the interfaces. With $\bigcup_{\alpha_1}\left(\Omega_{\alpha_1}\cap\Omega_t\right)$ we denote the set of hole areas Ω_{α_1} that are in the fundamental unit cell Ω_t.

Substituting Equations (6.19) and (6.20a) in Equation (6.20b), we can eliminate all expansion coefficients of the plane waves, except for the expansion coefficients of the grazing P-polarized plane waves:

$$\mathbf{h}^{\text{pit}} - \mathscr{A}\left(\mathbf{e}^{\text{pit}}\right) - \sum_{\boldsymbol{\beta}\in\mathscr{B}_0} b_{\boldsymbol{\beta}}\mathbf{h}_{\boldsymbol{\beta}}(x,y,\pm D/2) = \mathbf{h}^{\text{in}} + \mathbf{h}^{r}. \tag{6.21}$$

Just as in the non-periodic case, we project this equation on the functions $\boldsymbol{v}_{\bar{\boldsymbol{\alpha}}'}$ by using the scalar product defined in Equation (2.15) on page 22:

$$\begin{aligned}\sum_{\alpha_4} a_{\boldsymbol{\alpha}'}\zeta_{\boldsymbol{\alpha}'}(\pm D/2) - \sum_{\boldsymbol{\alpha}} a_{\boldsymbol{\alpha}}\eta_{\boldsymbol{\alpha}}(\pm D/2)\left\langle\mathscr{A}\left(\boldsymbol{v}_{\bar{\boldsymbol{\alpha}}}\right)\middle|\boldsymbol{v}_{\bar{\boldsymbol{\alpha}}'}\right\rangle_{\Omega_{p'}}&\\ - \sum_{\boldsymbol{\beta}\in\mathscr{B}_0} b_{\boldsymbol{\beta}}\zeta_{\boldsymbol{\beta}}(\pm D/2)\left\langle\boldsymbol{v}_{\boldsymbol{\beta}}\middle|\boldsymbol{v}_{\bar{\boldsymbol{\alpha}}'}\right\rangle_{\Omega_{p'}} &= \left\langle\mathbf{h}^{\text{in}} + \mathbf{h}^{r}\middle|\boldsymbol{v}_{\bar{\boldsymbol{\alpha}}'}\right\rangle_{\Omega_{p'}},\end{aligned} \tag{6.22}$$

where the summation over α_4 is a summation over the two directions of propagation (α_4 is not contained in $\bar{\boldsymbol{\alpha}}$). This equation is valid for all $\bar{\boldsymbol{\alpha}}'$, hence for all α_1 (counting the number of holes and pits in the unit cell), for all α_2 (TE and TM polarization) and for all α_3 (denoting the spatial frequency).

The interaction integral in the above equation is given by:

$$\begin{aligned}\left\langle\mathscr{A}\left(\boldsymbol{v}_{\bar{\boldsymbol{\alpha}}}\right)\middle|\boldsymbol{v}_{\bar{\boldsymbol{\alpha}}'}\right\rangle_{\Omega_{p'}} = &\sum_{\beta_2\in\mathscr{U}^{\text{in}}}\frac{k_z}{\omega\mu_0}\left\langle\boldsymbol{v}_{\bar{\boldsymbol{\alpha}}}\middle|\boldsymbol{v}^{\text{S}}_{\beta_2}\right\rangle_{\Omega_p}\left\langle\boldsymbol{v}^{\text{S}}_{\beta_2}\middle|\boldsymbol{v}_{\bar{\boldsymbol{\alpha}}'}\right\rangle_{\Omega_{p'}}\\ &+ \sum_{\beta_2\in\mathscr{U}^{\text{in}}_c}\frac{\omega\varepsilon\varepsilon_0}{k_z}\left\langle\boldsymbol{v}_{\bar{\boldsymbol{\alpha}}}\middle|\boldsymbol{v}^{\text{P}}_{\beta_2}\right\rangle_{\Omega_p}\left\langle\boldsymbol{v}^{\text{P}}_{\beta_2}\middle|\boldsymbol{v}_{\bar{\boldsymbol{\alpha}}'}\right\rangle_{\Omega_{p'}},\end{aligned} \tag{6.23}$$

where in the last term the grazing orders are not contained in the summation. The factor $\langle\boldsymbol{v}_{\bar{\boldsymbol{\alpha}}}\,|\,\boldsymbol{v}_{\boldsymbol{\beta}}\rangle_{\Omega_p}$ can be calculated analytically and is specified in Equations (A.2) and (A.3) in Appendix A.1.

Another set of equations is obtained by projecting the matching condition for the electric field (6.20a) onto the functions $\boldsymbol{v}_{\boldsymbol{\beta}}$ of the grazing orders:

$$\sum_{\alpha_4} a_{\boldsymbol{\alpha}'}\eta_{\boldsymbol{\alpha}'}(\pm D/2)\left\langle\boldsymbol{v}_{\bar{\boldsymbol{\alpha}}}\middle|\boldsymbol{v}_{\boldsymbol{\beta}}\right\rangle_{\Omega_t} = 0, \qquad \text{with } \boldsymbol{\beta}\in\mathscr{B}_0. \tag{6.24}$$

Together with Equation (6.22) we have our system of equations complete.

To obtain the remaining expansion coefficients of the plane waves, we project Equation (6.20a) onto the function $\boldsymbol{v}_{\boldsymbol{\beta}}$:

$$b_{\boldsymbol{\beta}} = \frac{1}{\eta_{\boldsymbol{\beta}}(\pm D/2)}\sum_{\boldsymbol{\alpha}} a_{\boldsymbol{\alpha}}\eta_{\boldsymbol{\alpha}}\left\langle\boldsymbol{v}_{\bar{\boldsymbol{\alpha}}}\middle|\boldsymbol{v}_{\boldsymbol{\beta}}\right\rangle_{\Omega_t}, \qquad \text{with } \boldsymbol{\beta}\in\mathscr{B}_c, \tag{6.25}$$

which is valid for all plane waves except for the grazing ones.

In conclusion, we have found that the theory for the periodic case is quite similar to the non-periodic case. There are three maior differences. The first difference is in the plane waves and their normalization. Secondly, the operator $\mathscr{A}$ that relates the tangential magnetic field to the tangential electric field is now not an integral operator but a summation. As a consequence, also the interaction integral is different. Finally, if one of the orders is grazing, we can not eliminate all plane waves from the system of equations anymore. The coefficients of the plane waves that correspond to a grazing order of the grating give rise to a small number of additional equations.

Chapter 7

Mode expansion theory for a nearby dipole source

7.1 Introduction

In this chapter, we apply the mode expansion theory for the case that the incident field originates from a dipole source that is placed near the perfectly conducting layer or inside an aperture.

We will shortly review the scattering problem considered. We assume a finite number of rectangular pits and holes in a perfectly conducting layer with finite thickness D. The sub- or superscript p denotes the number of the pit or hole. The lengths in the x- and y-direction are L_x^p and L_y^p, respectively. The cross-section of a hole or a pit p is given by $\Omega_p = \left\{ (x, y) \,\middle|\, x_0^p < x < x_0^p + L_x^p,\ y_0^p < y < y_0^p + L_y^p \right\}$. The depth of a pit p is $d_p < D$. The half spaces $z > D/2$ and $z < -D/2$ are filled with homogeneous dielectrics with index of refraction n_u and n_ℓ, respectively. Every hole and pit is filled with a homogeneous dielectric with index of refraction n_p. The corresponding relative permeabilities are $\varepsilon_u = n_u^2$, $\varepsilon_\ell = n_\ell^2$ and $\varepsilon_p = n_p^2$. The magnetic permeability is μ_0 everywhere.

In the theory discussed in Chapters 2 and 6 we assumed the incident field to be

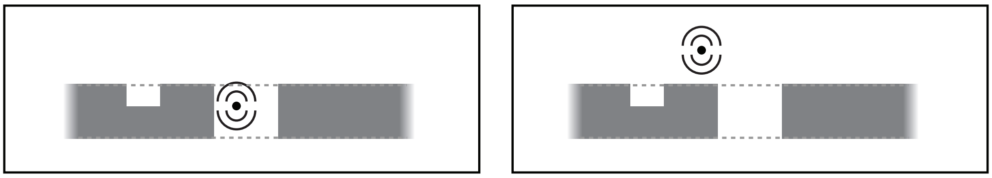

Figure 7.1: Whereas in Chapters 2 and 6 the incident field originated from an unspecified source at infinity, now, a harmonically oscillating dipole source is located inside or near a hole or pit.

given, without specifying the sources that caused them. The incident field could be decomposed into plane waves propagating toward the conducting layer. This field was (and is) monochromatic with a wavelength λ in free space. The local wavelengths are $\lambda_u = \lambda / n_u$, $\lambda_\ell = \lambda / n_\ell$ and $\lambda_p = \lambda / n_p$. The corresponding wave numbers are $k_u = 2\pi/\lambda_u$, $k_\ell = 2\pi/\lambda_\ell$ and $k_p = 2\pi/\lambda_p$.

We now assume a dipole to be the source of the electromagnetic radiation of the diffraction problem. This dipole has a fixed angular frequency ω and is undamped. Let the dipole be located at the point (x_0, y_0, z_0). See Figure 7.1 on the preceding page. The current density $\mathbf{J}$ is then given by:

$$\mathbf{J}(x,y,z) = -i\omega\mathbf{p}\,\delta(x-x_0)\,\delta(y-y_0)\,\delta(z-z_0), \tag{7.1}$$

with $\mathbf{p}$ the electric dipole moment.

As in the case of an incident field originating from infinity, the method to solve this problem consists of three steps. These were discussed extensively in Chapter 2 and we will summarize them here shortly.

First, we consider the field inside the holes and pits, of which one can have a dipole inside. As the space inside the holes is homogeneous (in the sense that ε_p does not depend on the space coordinate), the electromagnetic field has to satisfy the non-homogeneous Helmholtz Equation (1.20) on page 7, which means that the dipole is the source term. After applying the appropriate boundary conditions, we find two discrete sets of solutions for the homogeneous (source-free) Helmholtz equation: waveguide modes that are either propagating (or evanescent) in the positive direction or in the negative direction. These waveguide modes are labeled by the bold subscript $\boldsymbol{\alpha} = (\alpha_1, \alpha_2, \alpha_3, \alpha_4)$ which is a multi-index that describes four discrete variables: α_1 (or p) denotes the pit number, α_2 indicates the polarization (TE or TM), α_3 is determines the spatial frequency and α_4 specifies whether the mode is propagating upwards or downwards. The solution for the homogeneous Helmholtz equation is a linear combination of all waveguide modes, with expansion coefficients $a_{\boldsymbol{\alpha}}$. We then have to find a particular solution of the non-homogeneous problem. The sum of the waveguide modes and the particular solution yields the total field inside the hole.

Second, we find expressions for the field above and below the layer. This electromagnetic field is split into three parts: the (known) incident field, its corresponding reflected field (that results from the incident field when the conducting layer does not contain any pits or holes) and the scattered field (that results from the presence of the pits and holes). If the incident field is a plane wave (or a sum of plane waves) then its corresponding reflected field is easily calculated from the boundary conditions, as discussed in Section 1.6. If, however, the incident field originates from a dipole with vector (p_x, p_y, p_z), located at, say, (x_0, y_0, z_0) with $z_0 > D/2$, we can calculate the sum of incident and corresponding reflected field by putting a mirror dipole with vector $(-p_x, -p_y, p_z)$ at $(x_0, y_0, D - z_0)$. The sum of the incident and its corresponding reflected field anywhere in the half space is the sum of the free space fields of the two dipoles. The scattered field, which results from the presence of the holes and pits, is expanded into plane waves (that are either propagating or evanescent in the z-direction). These plane waves are labeled by the bold subscript $\boldsymbol{\beta} = (\beta_1, \beta_2)$. This is a short notation for the polarization (β_1) and the x- and y-component of the wave vector ($\beta_2 = (k_x, k_y)$). The polarization can either be S or P. S-polarized means that the z-component of the electric field is zero (and thus corresponds to TE polarization inside the holes and pits), while for P-polarization the z-component of the magnetic field is zero (TM polarization). The expansion coefficients of the scattered field $b_{\boldsymbol{\beta}}$ together with the expansion coefficients $a_{\boldsymbol{\alpha}}$ of the waveguide modes describe our scattering problem.

Third, we will determine these expansion coefficients by matching the expressions for the electric and magnetic field at the interfaces $z = \pm D/2$. These matching equations only involve the tangential parts of the electric and magnetic fields, for which we use lower case letters:

$$\mathbf{e}(x,y,z) \equiv \hat{\boldsymbol{\imath}}_z \times \left[\hat{\boldsymbol{\imath}}_z \times \mathbf{E}(x,y,z)\right] = \begin{pmatrix} -E_x \\ -E_y \\ 0 \end{pmatrix}, \tag{7.2a}$$

$$\mathbf{h}(x,y,z) \equiv \hat{\boldsymbol{\imath}}_z \times \mathbf{H}(x,y,z) = \begin{pmatrix} -H_y \\ H_x \\ 0 \end{pmatrix}, \tag{7.2b}$$

with $\hat{\boldsymbol{\imath}}_z$ the unit vector in the z-direction. By using a Fourier operator, we can eliminate the coefficients of the plane waves from the system of (matching) equations. Hence, we are left with a relatively small system for the coefficients of the waveguide modes only.

In Sections 7.2 and 7.3 we will determine the electromagnetic field inside the pits and holes and above and below the conducting layer, respectively. Section 7.4 deals with the matching of the expressions at the interfaces. Section 7.5 is devoted to the far field expressions.

7.2 The field inside the holes and pits

As stated in the introduction, the field inside the holes is the sum of a solution of the homogeneous Helmholtz equation and a particular solution:

$$\begin{pmatrix} \mathbf{e} \\ \mathbf{h} \end{pmatrix} = \begin{pmatrix} \mathbf{e}^{\text{hom}} \\ \mathbf{h}^{\text{hom}} \end{pmatrix} + \begin{pmatrix} \mathbf{e}^{\text{part}} \\ \mathbf{h}^{\text{part}} \end{pmatrix}, \tag{7.3}$$

where we are interested in the tangential parts, because only these will appear in the matching equations, later on.

The solution of the homogeneous Helmholtz equation consists of a infinite number of waveguide modes. These were introduced in Chapter 2. We will repeat the main aspects of these waveguide modes and then we will determine the particular solution of the non-homogeneous equation, resulting from the dipole source.

7.2.1 Homogeneous solution inside the holes and pits

The transverse components of the modes are split into a real part that depends on x and y and a complex part that depends on z:

$$\mathbf{e}_{\boldsymbol{\alpha}}(x,y,z) = \boldsymbol{v}_{\boldsymbol{\alpha}}(x,y)\,\eta_{\boldsymbol{\alpha}}(z), \tag{7.4a}$$

$$\mathbf{h}_{\boldsymbol{\alpha}}(x,y,z) = \boldsymbol{v}_{\boldsymbol{\alpha}}(x,y)\,\zeta_{\boldsymbol{\alpha}}(z), \tag{7.4b}$$

where the subscript $\bar{\boldsymbol{\alpha}} = (\alpha_1, \alpha_2, \alpha_3)$ and thus the transverse vector field $\boldsymbol{v}_{\bar{\boldsymbol{\alpha}}}$ do not depend on the direction of propagation of the mode. A complete listing of the functions $\boldsymbol{v}_{\bar{\boldsymbol{\alpha}}}$, $\eta_{\boldsymbol{\alpha}}$ and $\zeta_{\boldsymbol{\alpha}}$ can be found in Section 2.1.1.

The real parts of the modes are normalized by [1]:

$$\left\langle \boldsymbol{v}_{\bar{\boldsymbol{\alpha}}} \middle| \boldsymbol{v}_{\bar{\boldsymbol{\alpha}}} \right\rangle_{\Omega_p} \equiv \iint\limits_{\Omega_p} \left[v_{\bar{\boldsymbol{\alpha}},x}(x,y)\, v_{\bar{\boldsymbol{\alpha}},x}(x,y)^* + v_{\bar{\boldsymbol{\alpha}},y}(x,y)\, v_{\bar{\boldsymbol{\alpha}},y}(x,y)^* \right] \mathrm{d}x\,\mathrm{d}y = 1, \tag{7.5}$$

where the integration domain Ω_p is the cross-section of hole p. Furthermore, the modes are orthogonal such that:

$$\left\langle \boldsymbol{v}_{\bar{\boldsymbol{\alpha}}} \middle| \boldsymbol{v}_{\bar{\boldsymbol{\alpha}}'} \right\rangle_{\Omega_{p'}} = 0, \qquad \text{if } \bar{\boldsymbol{\alpha}} \neq \bar{\boldsymbol{\alpha}}', \tag{7.6}$$

for different modes $\bar{\boldsymbol{\alpha}}$ and $\bar{\boldsymbol{\alpha}}'$.

The solution of the homogeneous Helmholtz equation for the tangential electric and magnetic field is thus given by:

$$\mathbf{e}^{\text{hom}}(x,y,z) = \sum_{\boldsymbol{\alpha}} a_{\boldsymbol{\alpha}}\, \boldsymbol{v}_{\bar{\boldsymbol{\alpha}}}(x,y)\,\eta_{\boldsymbol{\alpha}}(z), \tag{7.7a}$$

$$\mathbf{h}^{\text{hom}}(x,y,z) = \sum_{\boldsymbol{\alpha}} a_{\boldsymbol{\alpha}}\, \boldsymbol{v}_{\bar{\boldsymbol{\alpha}}}(x,y)\,\zeta_{\boldsymbol{\alpha}}(z), \tag{7.7b}$$

with $a_{\boldsymbol{\alpha}}$ the afore-mentioned expansion coefficients.

7.2.2 Particular solution inside the holes and pits

In order to derive the particular solution, we consider the Helmholtz equation for the magnetic field inside the hole:

$$\left(\Delta + k_p^2\right)\mathbf{H}(x,y,z) = -\nabla \times \mathbf{J}(x,y,z), \tag{7.8}$$

with $k_p = \omega\sqrt{\varepsilon_0\varepsilon_p\mu_0}$ the wave vector inside the hole. We combine the tangential parts and separate the z-component of the magnetic field:

$$\left(\Delta + k_p^2\right)\mathbf{h}(x,y,z) = \mathbf{q}(x,y,z), \tag{7.9a}$$

$$\left(\Delta + k_p^2\right)H_z(x,y,z) = Q_z(x,y,z), \tag{7.9b}$$

with

$$\mathbf{q} = \begin{pmatrix} q_x \\ q_y \end{pmatrix} = \begin{pmatrix} -\dfrac{\partial J_z}{\partial x} + \dfrac{\partial J_x}{\partial z} \\[2ex] -\dfrac{\partial J_z}{\partial y} + \dfrac{\partial J_y}{\partial z} \end{pmatrix}, \tag{7.10a}$$

$$Q_z = -\frac{\partial J_y}{\partial x} + \frac{\partial J_x}{\partial y}. \tag{7.10b}$$

We now assume that the particular solution of Equation (7.9a) is of the following form:

$$\mathbf{h}^{\text{part}}(x,y,z) = \sum_{\bar{\boldsymbol{\alpha}}} \boldsymbol{v}_{\bar{\boldsymbol{\alpha}}}(x,y)\, h_{\bar{\boldsymbol{\alpha}}}^{\text{part}}(z). \tag{7.11}$$

According to Fourier theory, this kind of expansion with $\boldsymbol{v}_{\bar{\boldsymbol{\alpha}}}$ as basis functions is always possible for any field inside the hole concerned, in a fixed plane perpendicular to the z-axis. Hence, our goal is now to find the function $h_{\bar{\boldsymbol{\alpha}}}^{\text{part}}(z)$.

We substitute Equation (7.11) into Helmholtz Equation (7.9a) and perform the double differentiation with respect to the x- and y-coordinate:

$$\sum_{\bar{\boldsymbol{\alpha}}} \boldsymbol{v}_{\bar{\boldsymbol{\alpha}}}(x,y)\left(\frac{d^2}{dz^2} + \gamma_z^2\right) h_{\bar{\boldsymbol{\alpha}}}^{\text{part}}(z) = \mathbf{q}(x,y,z), \tag{7.12}$$

where we have found the z-component of the propagation constant:

$$\gamma_z = \sqrt{k_p^2 - \left(\frac{m_x\pi}{L_x}\right)^2 - \left(\frac{m_y\pi}{L_y}\right)^2}. \tag{7.13}$$

With the help of the scalar product in Equation (7.5), we obtain the following set of differential equations:

$$\left(\frac{d^2}{dz^2} + \gamma_z^2\right) h_{\bar{\boldsymbol{\alpha}}}^{\text{part}}(z) = \left\langle \boldsymbol{q} \middle| \boldsymbol{v}_{\bar{\boldsymbol{\alpha}}} \right\rangle_{\Omega_p}. \tag{7.14}$$

The right-hand side $\langle \boldsymbol{q} | \boldsymbol{v}_{\tilde{\boldsymbol{\alpha}}} \rangle_{\Omega_p}$ consists of a sum of a term with $\delta(z)$ and a term with the derivative $\frac{d}{dz}\delta(z)$. For details, see Appendix C.1. To solve (7.14), we thus need particular solutions of:

$$\left(\frac{d^2}{dz^2} + \gamma_z^2\right) u(z) = \delta(z), \tag{7.15a}$$

$$\left(\frac{d^2}{dz^2} + \gamma_z^2\right) v(z) = \frac{d}{dz}\delta(z), \tag{7.15b}$$

for which we choose:

$$u(z) = \begin{cases} (2i\gamma_z)^{-1}\, e^{i\gamma_z |z|}, & |\gamma_z / k_p| \geq \epsilon, \\ (2\gamma_z)^{-1}\, \sin\{\gamma_z |z|\}, & |\gamma_z / k_p| < \epsilon, \end{cases} \tag{7.16a}$$

$$v(z) = \frac{d}{dz} u(z) = \begin{cases} \left[\mathrm{H}(z) - \frac{1}{2}\right] e^{i\gamma_z |z|}, & |\gamma_z / k_p| \geq \epsilon, \\ \left[\mathrm{H}(z) - \frac{1}{2}\right] \cos\left(\gamma_z z\right), & |\gamma_z / k_p| < \epsilon, \end{cases} \tag{7.16b}$$

with $\mathrm{H}(z)$ the Heaviside function, defined by:

$$\mathrm{H}(z) = \begin{cases} 0, & z < 0, \\ 1, & z \geq 0. \end{cases} \tag{7.17}$$

Note that, by splitting u and v, depending on γ_z, these solutions have a well defined limit for the case that γ_z approaches zero. For larger $|\gamma_z|$, the solutions propagate outward and are symmetrical around $z = 0$. The reader might wonder why we do not use the sine and cosine form always instead of using the exponential form only for $|\gamma_z / k_p| < \epsilon$. However, for large and purely imaginary γ_z, the functions $\cos(\gamma_z z)$ and $\sin(\gamma_z z)$ increase exponentially with $|z|$, which is not very convenient for numerical implementation. The value of the smallness parameter ϵ is set to 10^{-5}. We find the following solution for $h^{\mathrm{part}}_{\tilde{\boldsymbol{\alpha}}}$:

$$h^{\mathrm{part}}_{\tilde{\boldsymbol{\alpha}}}(z) = \begin{cases} -i\omega v(z - z_0)\, \mathbf{p}_\parallel \cdot \boldsymbol{v}_{\tilde{\boldsymbol{\alpha}}}(x_0, y_0)^*, & \text{for TE}, \\ -i\omega \left[p_z\, u(z - z_0)\, \nabla_\parallel + v(z - z_0)\, \mathbf{p}_\parallel\right] \cdot \boldsymbol{v}_{\tilde{\boldsymbol{\alpha}}}(x_0, y_0)^*, & \text{for TM}, \end{cases} \tag{7.18}$$

where $\mathbf{p}_\parallel = (p_x, p_y)$ contains only the tangential components of the dipole moment. The factor $\nabla_\parallel \cdot \boldsymbol{v}_{\tilde{\boldsymbol{\alpha}}}(x_0, y_0)^*$ denotes the gradient with respect to the tangential components x and y applied to the function $\boldsymbol{v}^*_{\tilde{\boldsymbol{\alpha}}}$ and evaluated in the point (x_0, y_0) where the dipole is located. From Equation (7.18) it is clear that a dipole that is oriented in the z-direction can only excite waveguide modes that are TM polarized.

In order to derive the particular solution for the tangential electric field, the particular solution for the z-component of the magnetic field is necessary. We will derive this solution here. The z-component of the magnetic field that is a solution of the homogeneous Helmholtz equation is written as the product of a factor that depends on the x and y-coordinate and a factor that only depends on z:

$$H_z^{\text{hom}}(x,y,z) = \sum_{\boldsymbol{\alpha}} a_{\boldsymbol{\alpha}}\, \vartheta_{\bar{\boldsymbol{\alpha}}}(x,y)\, g_{\boldsymbol{\alpha}}(z). \tag{7.19}$$

We now define the function $\varphi_{\bar{\boldsymbol{\alpha}}}$ such that:

$$\left\langle \vartheta_{\bar{\boldsymbol{\alpha}}} \middle| \varphi_{\bar{\boldsymbol{\alpha}}'} \right\rangle_{\Omega_p} \equiv \iint_{\Omega_p} \vartheta_{\bar{\boldsymbol{\alpha}}}(x,y)\, \varphi_{\bar{\boldsymbol{\alpha}}'}(x,y)^*\, \mathrm{d}x\, \mathrm{d}y = \begin{cases} 1, & \bar{\boldsymbol{\alpha}} = \bar{\boldsymbol{\alpha}}', \\ 0, & \bar{\boldsymbol{\alpha}} \neq \bar{\boldsymbol{\alpha}}'. \end{cases} \tag{7.20}$$

See Appendix C.1 for the precise definition of $\vartheta_{\bar{\boldsymbol{\alpha}}}$ and $\varphi_{\bar{\boldsymbol{\alpha}}}$. Similar to the case of the tangential components of the particular solution of the magnetic field, we assume that a particular solution of Equation (7.9b) is of the following form:

$$H_z^{\text{part}}(x,y,z) = \sum_{\bar{\boldsymbol{\alpha}}} \vartheta_{\bar{\boldsymbol{\alpha}}}(x,y)\, H_{z,\bar{\boldsymbol{\alpha}}}^{\text{part}}(z). \tag{7.21}$$

Now, substituting this equation into (7.9b) and performing the double differentiation with respect to x and y, we obtain:

$$\sum_{\bar{\boldsymbol{\alpha}}} \vartheta_{\bar{\boldsymbol{\alpha}}}(x,y) \left(\frac{d^2}{dz^2} + \gamma_z^2 \right) H_{z,\boldsymbol{\alpha}}^{\text{part}}(z) = Q_z(x,y,z). \tag{7.22}$$

After projecting this equation on function $\varphi_{\bar{\boldsymbol{\alpha}}}$, using Equation (7.20), we have again a set of differential equations:

$$\left(\frac{d^2}{dz^2} + \gamma_z^2 \right) H_{z,\bar{\boldsymbol{\alpha}}}^{\text{part}}(z) = \left\langle Q_z \middle| \varphi_{\bar{\boldsymbol{\alpha}}} \right\rangle_{\Omega_p}. \tag{7.23}$$

The right-hand part $\left\langle Q_z \middle| \varphi_{\bar{\boldsymbol{\alpha}}} \right\rangle_{\Omega_p}$ contains the Dirac delta function $\delta(z)$ (see Appendix C.1 for the details), hence $u(z)$ as given by Equation (7.16a) occurs in the particular solution $H_{z,\bar{\boldsymbol{\alpha}}}^{\text{part}}$:

$$H_{z,\bar{\boldsymbol{\alpha}}}^{\text{part}}(z) = \begin{cases} \omega\, u(z-z_0)\, \mathbf{p}_\parallel \cdot \boldsymbol{v}_{\bar{\boldsymbol{\alpha}}}(x_0,y_0)^*, & \text{for TE}, \\ 0, & \text{for TM}. \end{cases} \tag{7.24}$$

With Equations (7.11), (7.16), (7.18), (7.21) and (7.24) the particular solution of the magnetic field is complete. This solution is divergence free, as it should be.

Now that we have the magnetic field, we wish to have the associated tangential electric field. From Maxwell's Equation (1.15d), we have:

$$\mathbf{e}^{\text{part}}(x,y,z) = \frac{1}{i\omega\varepsilon_0\varepsilon_p} \begin{pmatrix} \dfrac{\partial H_z^{\text{part}}}{\partial y} + \dfrac{\partial h_x^{\text{part}}}{\partial z} \\[2ex] -\dfrac{\partial H_z^{\text{part}}}{\partial x} + \dfrac{\partial h_y^{\text{part}}}{\partial z} \end{pmatrix} + \frac{1}{i\omega\varepsilon_0\varepsilon_p}\mathbf{j}, \tag{7.25}$$

with **j** the tangential component of the dipole current density (7.1). The second term on the right vanishes everywhere, except in the point (x_0, y_0, z_0). Therefore, we only derive the electric field in the region outside this point:

$$\mathbf{e}^{\text{part}}_{\bar{\boldsymbol{\alpha}}}(x, y, z) = \boldsymbol{v}_{\bar{\boldsymbol{\alpha}}}(x, y)\, e^{\text{part}}_{\bar{\boldsymbol{\alpha}}}(z), \tag{7.26}$$

with

$$e^{\text{part}}_{\bar{\boldsymbol{\alpha}}}(z) = \frac{1}{i\omega\varepsilon_0\varepsilon_p}\left[i\Gamma^2_{\bar{\boldsymbol{\alpha}}}\, H^{\text{part}}_{z,\bar{\boldsymbol{\alpha}}}(z) + \frac{d}{dz}\, h^{\text{part}}_{\bar{\boldsymbol{\alpha}}}(z)\right], \tag{7.27}$$

where $H^{\text{part}}_{z,\bar{\boldsymbol{\alpha}}}$ is given by Equation (7.24) and $h^{\text{part}}_{\bar{\boldsymbol{\alpha}}}$ by Equation (7.18). The full listing of $e^{\text{part}}_{\bar{\boldsymbol{\alpha}}}$ is given in Appendix C.1, along with the definition of the normalization constant $\Gamma_{\bar{\boldsymbol{\alpha}}}$. The general expression for the field inside the holes is given by the sum of the particular solution and a solution of the homogeneous Equation (7.7):

$$\mathbf{e}(x, y, z) = \sum_{\boldsymbol{\alpha}} \boldsymbol{v}_{\bar{\boldsymbol{\alpha}}}(x, y)\left[a_{\boldsymbol{\alpha}}\eta_{\boldsymbol{\alpha}}(z) + e^{\text{part}}_{\bar{\boldsymbol{\alpha}}}(z)\right], \tag{7.28a}$$

$$\mathbf{h}(x, y, z) = \sum_{\boldsymbol{\alpha}} \boldsymbol{v}_{\bar{\boldsymbol{\alpha}}}(x, y)\left[a_{\boldsymbol{\alpha}}\zeta_{\boldsymbol{\alpha}}(z) + h^{\text{part}}_{\bar{\boldsymbol{\alpha}}}(z)\right]. \tag{7.28b}$$

As stated before, this equation is only valid outside the plane $z = z_0$.

The particular solution satisfies Helmholtz Equation (7.8) and the boundary conditions at the flanks of the pits and holes. In Section 7.4, we will see how, at the interfaces $z = \pm D/2$, the total electromagnetic field inside the pits and holes is matched to the total electromagnetic field above and below the conducting layer. For the case of a pit, however, there is only one interface at which the fields are matched. In addition, boundary conditions have to be satisfied at the bottom of the pit. The introduction of a mirror dipole can account for this. For a dipole located at (x_0, y_0, z_0) inside a pit with depth d_p, with dipole vector $\mathbf{p} = (p_x, p_y, p_z)$, the mirror dipole is located at $(x_0, y_0, D - 2d_p - z_0)$. Its dipole vector can be derived from the condition that the total tangential electric field, due to both dipoles, must vanish at $z = D/2 - d_p$. This gives a mirror dipole vector $\hat{\mathbf{p}} = (-p_x, -p_y, p_z)$. Hence, for the case of a dipole inside a pit, the particular solution is the sum of the particular solutions of the dipole and its mirror dipole.

7.3 The field above and below the layer

The total electric and magnetic field above and below the conducting layer consist of the (known) incident field, its corresponding reflected field (that results from the incident field when the conducting layer does not contain any pits or holes) and the scattered field (that results from the presence of the pits and holes):

$$\begin{bmatrix} \mathbf{E}(\mathbf{r}) \\ \mathbf{H}(\mathbf{r}) \end{bmatrix} = \begin{bmatrix} \mathbf{E}^i(\mathbf{r}) \\ \mathbf{H}^i(\mathbf{r}) \end{bmatrix} + \begin{bmatrix} \mathbf{E}^r(\mathbf{r}) \\ \mathbf{H}^r(\mathbf{r}) \end{bmatrix} + \begin{bmatrix} \mathbf{E}^s(\mathbf{r}) \\ \mathbf{H}^s(\mathbf{r}) \end{bmatrix}. \tag{7.29}$$

We will first treat the incident and reflected field before turning to the scattered field.

7.3.1 Incident and reflected field

In the previous chapters, the incident field was a plane wave or a sum or integral of plane waves originating from a source at infinity. Then, the reflected field was easily calculated from the boundary condition for the fields at the interface between a dielectric and a perfect metal.

However, we now have an incident field that originates from a dipole source near the conducting layer. This dipole vector is $\mathbf{p} = (p_x, p_y, p_z)$ and the dipole is located at (x_0, y_0, z_0). In order to prevent the equations to become too lengthy, we restrict ourselves to a dipole in the upper half space and take $z_0 > D/2$.

As the reflected field in the above equation results from a flat, perfectly conducting layer, we can use a mirror dipole to calculate this reflected field. The total electromagnetic field of a single dipole near a perfectly conducting layer at $z = D/2$ is equal to the sum of the free space fields of the original dipole and its mirror dipole. The mirror dipole is located at $(x_0, y_0, D - z_0)$ and its dipole vector is again given by $\hat{\mathbf{p}} = (-p_x, -p_y, p_z)$. Hence, the free space field of the dipole at (x_0, y_0, z_0) is associated with the incident field, whereas the free space field of the mirror dipole at $(x_0, y_0, D - z_0)$ is associated with the reflected field.

The free space electric and magnetic field at $\mathbf{r} = (x, y, z)$, caused by a single dipole located at $\mathbf{r}_0 = (x_0, y_0, z_0)$ is well known [1]:

$$\mathbf{E}(x,y,z) = \frac{e^{ik_u|\mathbf{r}-\mathbf{r}_0|}}{4\pi\varepsilon_0\varepsilon|\mathbf{r}-\mathbf{r}_0|}\left\{k_u^2\left(\mathbf{n}\times\mathbf{p}\right)\times\mathbf{n} + \left[3\mathbf{n}\left(\mathbf{n}\cdot\mathbf{p}\right)-\mathbf{p}\right]\left(\frac{1}{|\mathbf{r}-\mathbf{r}_0|^2} - \frac{ik_u}{|\mathbf{r}-\mathbf{r}_0|}\right)\right\}, \tag{7.30a}$$

$$\mathbf{H}(x,y,z) = \frac{\omega k_u}{4\pi}\left(\mathbf{n}\times\mathbf{p}\right)\frac{e^{ik_u|\mathbf{r}-\mathbf{r}_0|}}{|\mathbf{r}-\mathbf{r}_0|}\left(1 - \frac{1}{ik_u|\mathbf{r}-\mathbf{r}_0|}\right), \tag{7.30b}$$

with:

$$|\mathbf{r}-\mathbf{r}_0| = \sqrt{(x-x_0)^2 + (y-y_0)^2 + (z-z_o)^2}, \tag{7.31}$$

and $\mathbf{n}$ the unit vector in the direction of $\mathbf{r}-\mathbf{r}_0$.

7.3.2 The scattered field

Whether the incident field originates from infinity or from a dipole source nearby, the description of the scattered field is the same and can be found in Section 2.2. In this section, we will only repeat the elements in the description that we need in the following section.

The tangential scattered field is expanded as follows:

$$\begin{bmatrix} \mathbf{e}^s(\mathbf{r}) \\ \mathbf{h}^s(\mathbf{r}) \end{bmatrix} = \sum_{\beta_1} \int_{-\infty}^{\infty} b_{\boldsymbol{\beta}} \begin{bmatrix} \mathbf{e}_{\boldsymbol{\beta}}(\mathbf{r}) \\ \mathbf{h}_{\boldsymbol{\beta}}(\mathbf{r}) \end{bmatrix} \mathrm{d}\beta_2, \tag{7.32}$$

where the coefficients $b_{\boldsymbol{\beta}}$ are still to be determined and $\left(\mathbf{e}_{\boldsymbol{\beta}}, \mathbf{h}_{\boldsymbol{\beta}}\right)$ are plane waves with wave vector $\mathbf{k}_u$ above the layer and $\mathbf{k}_\ell$ below the layer. The transverse components (k_x, k_y) of the wave vector are real and the z-component is given by:

$$k_z^u = +\sqrt{k_u^2 - k_x^2 - k_y^2}, \tag{7.33a}$$

$$k_z^\ell = -\sqrt{k_\ell^2 - k_x^2 - k_y^2}. \tag{7.33b}$$

The sign in Equation (7.33) follows from the assumed time dependence $\exp(-i\omega t)$ with $\omega > 0$ and from the fact that the scattered field propagates away from the conducting layer. We recall that $\int \mathrm{d}\beta_2$ is a shorthand notation for $\iint \mathrm{d}k_x \mathrm{d}k_y$.

The transverse components of the plane waves are split into a factor that depends on x and y and a factor that depends on z:

$$\mathbf{e}_{\boldsymbol{\beta}}(x,y,z) = \boldsymbol{v}_{\boldsymbol{\beta}}(x,y)\,\eta_{\boldsymbol{\beta}}(z), \tag{7.34a}$$

$$\mathbf{h}_{\boldsymbol{\beta}}(x,y,z) = \boldsymbol{v}_{\boldsymbol{\beta}}(x,y)\,\zeta_{\boldsymbol{\beta}}(z). \tag{7.34b}$$

Analogous to the normalization of the waveguide mode functions, we normalize $\boldsymbol{v}_{\boldsymbol{\beta}}$ such that:

$$\begin{aligned} \langle \boldsymbol{v}_{\boldsymbol{\beta}} | \boldsymbol{v}_{\boldsymbol{\beta}'} \rangle_{\mathbb{R}^2} &\equiv \iint_{\mathbb{R}^2} \left[v_{\boldsymbol{\beta},x}(x,y)\, v_{\boldsymbol{\beta}',x}(x,y)^* + v_{\boldsymbol{\beta},y}(x,y)\, v_{\boldsymbol{\beta}',y}(x,y)^* \right] \mathrm{d}x\,\mathrm{d}y \\ &= \delta_{\beta_1\beta_1'}\,\delta\left(\beta_2 - \beta_2'\right). \end{aligned} \tag{7.35}$$

Note that the integration is over an entire plane. The first δ is the Kronecker delta and the second is the two-dimensional Dirac delta function.

We have defined the operator $\mathscr{A}$ by Equation (2.29) on page 25. This operator maps any two-dimensional vector field $\mathbf{f} : \mathbb{R}^2 \to \mathbb{C}^2$ onto another such vector field and is in fact the integral version of the operator $\frac{\mathbf{k}}{\omega\mu_0}\times$ that can be applied to the electric field of a plane wave to calculate the corresponding magnetic field. In any plane for which z is constant and in particular for $z = \pm D/2$, the scattered transverse magnetic field can, with this operator, be expressed in terms of the transverse electric field:

$$\mathbf{h}^s(x,y,\pm D/2) = \mathscr{A}\left[\mathbf{e}^s(x,y,\pm D/2)\right]. \tag{7.36}$$

This equation holds for all (x,y) with $-\infty < x, y < \infty$.

7.4 Matching at the interfaces

At the interfaces $z = \pm D/2$, we have the following relations for the tangential electric and the tangential magnetic field:

$$\mathbf{e}^{\text{hom}} + \mathbf{e}^{\text{part}} = \mathbf{e}^{i} + \mathbf{e}^{r} + \mathbf{e}^{s}, \qquad \forall (x,y),\, z = \tfrac{\pm D}{2}, \tag{7.37a}$$

$$\mathbf{h}^{\text{hom}} + \mathbf{h}^{\text{part}} = \mathbf{h}^{i} + \mathbf{h}^{r} + \mathbf{h}^{s}, \qquad (x,y) \in \bigcup_{\alpha_1} \Omega_{\alpha_1},\, z = \tfrac{\pm D}{2}, \tag{7.37b}$$

where the left-hand side of these equations corresponds to the field inside the holes and the right-hand side to the field above or below the layer, depending on z. Because the layer is perfectly conducting, Equation (7.37a) reduces to:

$$\mathbf{e}^{\text{hom}} + \mathbf{e}^{\text{part}} = \mathbf{e}^{s}, \qquad \forall (x,y),\, z = \tfrac{\pm D}{2}. \tag{7.38}$$

Substituting Equations (7.36) and (7.38) in Equation (7.37b) gives:

$$\mathbf{h}^{\text{hom}} - \mathscr{A}\left(\mathbf{e}^{\text{hom}}\right) = \mathbf{h}^{i} + \mathbf{h}^{r} - \mathbf{h}^{\text{part}} + \mathscr{A}\left(\mathbf{e}^{\text{part}}\right), \tag{7.39}$$

which is valid for all $(x, y, \pm D/2)$ within the holes and pits. The left-hand side contains the coefficients of the waveguide modes $a_{\boldsymbol{\alpha}}$. The right-hand side is given by the following source terms: the terms $\mathbf{h}^{i} + \mathbf{h}^{r}$ refer to a dipole source above or below the layer (see Appendix C.2 for more details); the terms $\mathbf{h}^{\text{part}}$ and $\mathscr{A}\left(\mathbf{e}^{\text{part}}\right)$ refer to fields originating from a dipole inside a hole or pit.

One could also have more than one dipole, or the incident field can consists of plane waves from infinity together with the field from a nearby dipole source. The linearity of Maxwell's equations implies that the solution for the total incident field is simply the sum of the solutions for the separate incident fields and sources.

In order to obtain a system of equations that is suitable for numerical implementation, we project Equation (7.39) on the function $\boldsymbol{v}_{\bar{\boldsymbol{\alpha}}'}$ by using the scalar product defined in Equation (7.5):

$$\begin{aligned}
&\sum_{\alpha_4} a_{\boldsymbol{\alpha}'} \zeta_{\boldsymbol{\alpha}'}\left(\tfrac{\pm D}{2}\right) - \sum_{\boldsymbol{\alpha}} a_{\boldsymbol{\alpha}} \eta_{\boldsymbol{\alpha}}\left(\tfrac{\pm D}{2}\right) \left\langle \mathscr{A}\left(\boldsymbol{v}_{\bar{\boldsymbol{\alpha}}}\right) \middle| \boldsymbol{v}_{\bar{\boldsymbol{\alpha}}'} \right\rangle_{\Omega_{p'}} \\
&\quad = \left\langle \mathbf{h}^{i} + \mathbf{h}^{r} \middle| \boldsymbol{v}_{\bar{\boldsymbol{\alpha}}'} \right\rangle_{\Omega_{p'}} - h^{\text{part}}_{\bar{\boldsymbol{\alpha}}'}\left(\tfrac{\pm D}{2}\right) + \sum_{\bar{\boldsymbol{\alpha}}} \left\langle \mathscr{A}\left(\boldsymbol{v}_{\bar{\boldsymbol{\alpha}}}\right) \middle| \boldsymbol{v}_{\bar{\boldsymbol{\alpha}}'} \right\rangle_{\Omega_{p'}} e^{\text{part}}_{\bar{\boldsymbol{\alpha}}}\left(\tfrac{\pm D}{2}\right),
\end{aligned} \tag{7.40}$$

where the summation over α_4 is a summation over the two directions of propagation (α_4 is not contained in $\bar{\boldsymbol{\alpha}}$). This equation is valid for all $\bar{\boldsymbol{\alpha}}'$, hence for all α_1 (counting the number of holes and pits), for all α_2 (TE and TM polarization) and for all α_3 (the mode numbers, m_x and m_y). Consequently, solving the system of Equation (7.40) for all $\bar{\boldsymbol{\alpha}}'$ and for $z = \pm D/2$ gives the waveguide mode expansion coefficients $a_{\boldsymbol{\alpha}}$.

Comparing Equation (7.40) with Equation (2.42), we find that the only difference in the system of equations is in the right hand side which contains all physics regarding the sources. As explained earlier, most computation time is spent on calculating the interaction integral. However, the interaction integral does not depend on the thickness D of the conducting layer, the index of refraction n_p inside the pit or hole and, moreover, it does not depend on the incident field. Thus, for a certain setup, once the interaction integral is calculated and stored in a library, we can quickly and easily adapt the parameters D and n_p as well as the incident field, which is a great advantage of this method.

To obtain an expression for the scattered field, we use the normalization defined by Equation (7.35) to project Equation (7.38) for the tangential electric field on the plane wave mode function $\boldsymbol{v}_{\boldsymbol{\beta}'}$:

$$b_{\boldsymbol{\beta}'} = \eta_{\boldsymbol{\beta}'}\left(\tfrac{\pm D}{2}\right)^{-1} \sum_{\boldsymbol{\alpha}} \langle \boldsymbol{v}_{\bar{\boldsymbol{\alpha}}} | \boldsymbol{v}_{\boldsymbol{\beta}'} \rangle_{\mathbb{R}^2} \left[a_{\boldsymbol{\alpha}} \eta_{\boldsymbol{\alpha}}\left(\tfrac{\pm D}{2}\right) + e^{\text{part}}_{\bar{\boldsymbol{\alpha}}}\left(\tfrac{\pm D}{2}\right) \right]. \tag{7.41}$$

After substituting this equation into Equation (7.32), the scattered field can be calculated in a straightforward way by a double integration over k_x and k_y.

With Equations (7.40) and (7.41) we have formulated our three-dimensional vectorial radiation and scattering problem as a linear system for the amplitudes of the waveguide modes only. Since these modes are parametrized by two parameters (γ_x and γ_y), we have thus reduced the three-dimensional physical problem to a two-dimensional numerical problem.

7.5 The far field

By solving the system of Equations (7.40), we determine the coefficients for the waveguide modes $a_{\boldsymbol{\alpha}}$ inside the conducting layer. The coefficients $b_{\boldsymbol{\beta}}$ of the plane waves above and below the conducting layer are given by Equation (7.41). Then, with Equation (7.32), we have an expression for the electromagnetic field in the upper and lower half spaces. This expression is a double diffraction integral. By asymptotic evaluation of this integral, we obtain an (approximate) expression for the far field.

We limit the following derivation to the upper half space $z > D/2$. The lower half space gives similar results. We can write the electric field in spherical coordinates by:

$$\mathbf{E}(r,\varphi,\theta) = \iint_{-\infty}^{\infty} \mathbf{A}(k_x,k_y) e^{ir\Phi(k_x,k_y;\varphi,\theta)}\,\mathrm{d}k_x\mathrm{d}k_y, \tag{7.42}$$

with φ the azimuthal angle and θ the polar angle. Note that in the upper half space $z > D/2$ the angle θ is between 0 and $\pi/2$. The phase function is given by:

$$\Phi(k_x,k_y;\varphi,\theta) = \left(k_x\cos\varphi + k_y\sin\varphi\right)\sin\theta + k_z\cos\theta, \tag{7.43}$$

with $k_z = \sqrt{k_u^2 - k_x^2 - k_y^2}$ and with $\mathbf{k}_u$ the wave vector in the upper half space. The function $\mathbf{A}$ is called the spectral amplitude function of the electric field. For the magnetic field, we can write an expression that is similar to Equation (7.42) with its spectral amplitude function $\mathbf{B}$ given by:

$$\mathbf{B}(k_x, k_y) = \frac{\mathbf{k}_u}{\omega\mu_0} \times \mathbf{A}(k_x, k_y). \tag{7.44}$$

The spectral amplitude function of the scattered electric is listed in Appendix C.3.

From asymptotic theories [39, 40], we use the method of stationary phase to approximate Equation (7.42) for $r \to \infty$:

$$\mathbf{E}(r, \varphi, \theta) \approx 2\pi i k_u \cos\theta\, \mathbf{A}\left(k_x^0, k_y^0\right) \frac{e^{ik_u r}}{r}, \tag{7.45}$$

with:

$$k_x^0 = k_u \cos\varphi \sin\theta, \tag{7.46a}$$

$$k_y^0 = k_u \sin\varphi \sin\theta. \tag{7.46b}$$

This approximation is valid for $0 < \theta < \pi/2$. For $\theta = 0$ and $\theta = \pi/2$, the asymptotic expansion is far from trivial [41–43]. However, the contribution of these specific angles has measure zero in the total emitted energy.

For each direction $\mathbf{n} = (\cos\varphi \sin\theta, \sin\varphi \sin\theta, \cos\theta)$, we can now calculate the far field of the electric field. For the case of a dipole that is located above the layer, this field consists of three contributions: the scattered field that originates from the pits and holes, the field of the dipole and the field of the mirror dipole:

$$\begin{aligned}\mathbf{E}(r, \varphi, \theta) \approx \frac{k_u^2 e^{ik_u r}}{r} \Bigg\{ & i\sqrt{\frac{\mu_0}{\varepsilon_0\varepsilon}} \frac{\cos\theta}{\sin\theta} e^{-ik_u \frac{D}{2}\cos\theta} \left[-b^{\mathrm{S}} (\mathbf{n} \times \hat{\boldsymbol{\imath}}_z) + b^{\mathrm{P}} (\mathbf{n} \times \hat{\boldsymbol{\imath}}_z) \times \mathbf{n}\right] \\ & + \frac{1}{4\pi\varepsilon_0\varepsilon} \left[\left(\mathbf{n} \times \mathbf{p}\right) \times \mathbf{n}\, e^{-ik_u \mathbf{r}_1 \cdot \mathbf{n}} + \left(\mathbf{n} \times \hat{\mathbf{p}}\right) \times \mathbf{n}\, e^{-ik_u \mathbf{r}_2 \cdot \mathbf{n}}\right] \Bigg\}.\end{aligned} \tag{7.47}$$

The plane wave coefficients b^{S} and b^{P} are given by Equation (7.41) and should be evaluated in the point $\left(k_x^0, k_y^0\right)$. The vectors $\mathbf{r}_1$ and $\mathbf{r}_2$ are the position vectors of the dipole and its mirror image, respectively. In the above expression, we have used the approximation:

$$|\mathbf{r} - \mathbf{r}_j| \approx r - \mathbf{n} \cdot \mathbf{r}_j, \tag{7.48}$$

which is valid if $|\mathbf{r}|$ is large with respect to $|\mathbf{r}_j|$.

The energy that is radiated in the radial direction is given by:

$$\begin{aligned} S_r(r, \varphi, \theta) &= \tfrac{1}{2}\,\mathrm{Re}\left(\mathbf{E} \times \mathbf{H}^*\right) \cdot \mathbf{n} \\ &= \frac{k_u}{2\omega\mu_0}\,\mathrm{Re}\left[\mathbf{E} \times \left(\mathbf{n} \times \mathbf{E}^*\right)\right] \cdot \mathbf{n} \\ &= \frac{k_u}{2\omega\mu_0}\left(\mathbf{E} \cdot \mathbf{E}^* - |\mathbf{E} \cdot \mathbf{n}|^2\right). \end{aligned} \tag{7.49}$$

Because the electric field is divergence free in the far field, the energy that is radiated in the radial direction in the far field is:

$$S_r(r,\varphi,\theta) \approx \frac{k_u}{2\omega\mu_0}\mathbf{E}\cdot\mathbf{E}^*. \tag{7.50}$$

As the electric field, given by Equation (7.47), consists of four different vectors, it is clear that the Poynting vector in the radial direction, in principle, consists of sixteen terms. Four terms are formed by the dot product of a vector with itself. These terms are positive and correspond to the energy flux of the S polarized plane wave and of the P polarized plane wave of the scattered field, the energy flux of the dipole and of the mirror dipole. The other twelve terms are interference terms between pairs of different vectors. The interference terms can be positive or negative, depending on the phase relation between the pair of vectors. When the two vectors in a pair are orthogonal, the interference term is zero.

The relative spontaneous emission is calculated by integrating S_r over the upper half sphere and dividing the result by the total radiation that is emitted by a dipole having a vector $\mathbf{p} = (p_x, p_y, p_z)$ and located in free space:

$$f = \frac{1}{f_{\text{free}}}\int_0^{\pi/2}\int_0^{2\pi} S_r(r,\varphi,\theta)\, r^2 \sin\theta\, \mathrm{d}\varphi\, \mathrm{d}\theta, \tag{7.51}$$

with

$$f_{\text{free}} = \frac{c k_u^4 |\mathbf{p}|^2}{12\pi\varepsilon_0\varepsilon}. \tag{7.52}$$

Depending on the location of the dipole, its orientation and the presence of scattering structures such as pits and holes, the number f may be larger or smaller than unity, but can not be negative.

Chapter 8

Spontaneous emission calculations

8.1 Introduction

Spontaneous emission is the phenomenon of the transition of an excited state to a state with lower energy by the interaction of this excited state with vacuum fluctuations. When an excited state, such as a fluorescent molecule or a Rydberg atom, is placed near an interface between optically different materials, the spontaneous emission rate is changed with respect to the spontaneous emission in free space. This observation was made by Purcell in 1946 [44]. The excited state is the source of an electromagnetic field that is (partially) reflected by the interface. If this reflected field is in phase with the excited state then the spontaneous emission is enhanced and if the reflected field is out of phase then the spontaneous emission is decreased. Actually, when placed near an interface, not only the spontaneous emission of the excited state is altered, but also the spatial distribution of the emitted radiation.

For numerous applications, such as lasers, spectroscopy, light-emitting diodes and biomedical sensors, the changes in the spontaneous emission rate and the spatial distribution of radiation are important. However, especially when the interface near the excited state has a complex geometry, calculation of the field is far from trivial. Many calculations have been done for planar interfaces, for both metal-dielectric interfaces as well as dielectric-dielectric interfaces [45–50]. For non-planar interfaces with features that have sizes comparable to the wavelength of the emitted field, calculations are both challenging and time consuming. Research has been done on the influence of surface roughness, the presence of small particles and so-called islandized metal films were studied. See [51] and references therein for a comprehensive review. More recently, work has been done on spontaneous emission in micro cavities [52], near photonic crystals [53] and near nanoparticles [54–56].

Spontaneous emission is actually a phenomenon that can be explained by the full quantum theory but not by classical electromagnetics.[1] In quantum theory, the spontaneous emission rate is given by Fermi's golden rule. It states that the rate for spontaneous transition from an excited state to a lower energy state is proportional to the coupling between the excited state and the vacuum fluctuations times the number of ways in which the transition can take place.[2] In classical electromagnetics, an accelerating charge emits radiation and hence the charge ends up in a lower energy state. The phenomenon that the radiation of energy by an accelerating charged particle influences its own motion is called the radiative effect. In classical electrodynamics, this radiative reaction is not considered [1]. However, it turns out that both effects, vacuum fluctuations and radiation reaction, depend in the same way upon the mode expansion of the electromagnetic field [57]. This is the reason why the *relative* emission rate, i.e. the spontaneous emission of an excited state near some kind of interface normalized by the spontaneous emission rate of this excited state in free space, can be *calculated* with the classical approach, although it can not be *explained* by classical electromagnetics. More specifically, the relative spontaneous emission for an excited state near some kind of interface is equal to the total emitted radiation of the oscillating dipole, normalized by the total emitted radiation of the free space dipole. It is the total relative emitted radiation that we are going to calculate.

For these calculations, we use the classical theory that was presented in the previous chapter. The most important drawback of our calculations is the assumed perfect conductivity of the metal. We are aware of the importance of the finite penetration depth of metals at optical frequencies and the corresponding possibility of non-radiative decay of the excited state. However, for other parts of the electromagnetic spectrum, the assumption of perfect conductivity is certainly justified. In that case only radiative decay is possible. In fact, the first experiments on spontaneous emission enhancement and inhibition by Purcell were done for radio frequencies.

8.2 Numerical considerations

As explained in the previous chapter, the presence of a dipole source leads to a source term in the Helmholtz equation. For the case of a dipole inside a pit or hole, this source term consists of a delta function and its derivative. The solution of the Helmholtz equation then is a sum of a homogeneous and a particular solution. Both solutions are expanded in waveguide modes. These waveguide modes

---

[1] The first description of spontaneous emission was given by Einstein, in his phenomenological theory of absorption and spontaneous and stimulated emission.

[2] Often, though, a full quantum description of the atom is used together with a classical description of the field.

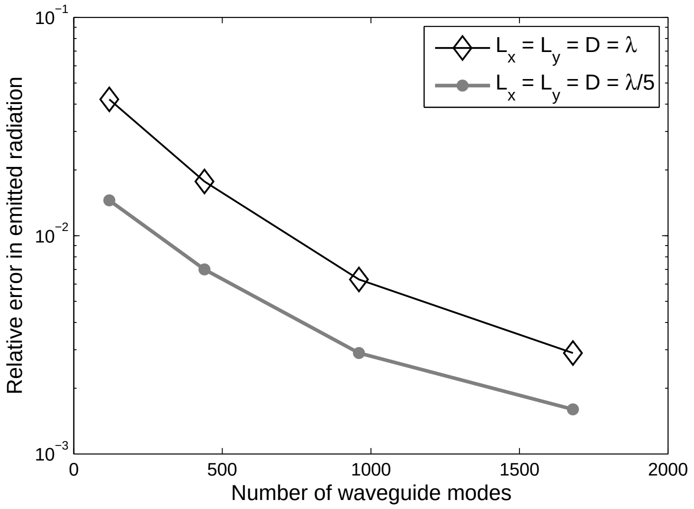

Figure 8.1: Relative error in the total emitted radiation as a function of the number of waveguide modes. As a reference, a calculation with 2600 waveguide modes is used. The setup is a single, cubic hole, with sizes λ and $\lambda/5$. The dipole is located in the center of the hole and is directed along the z-axis.

consist of trigonometric functions. The expansion of a delta function in trigonometric functions, converges slowly. Therefore, it is expected that a large number of waveguide modes has to be taken into account in order to arrive at an accurate solution. Figure 8.1 shows the relative error in the total emitted energy as a function of the number of waveguide modes. Calculations were done for 120, 440, 960 and 1680 waveguide modes and compared with calculations for 2600 waveguide modes. Compared with the relative error in the energy for the case of a plane wave (Figure 2.3 on page 31), apparently, still a relatively small amount of modes suffices to have an relative error smaller than one percent. In the results shown in this chapter, we always use 960 waveguide modes.

When a dipole is located above or below the perfectly conducting layer, in the right-hand side of the system of equations (7.40), the term $\mathbf{h}^i + \mathbf{h}^r$ is the total magnetic field that originates from the dipole, evaluated at the interface. It consists of the free space field of the dipole $\mathbf{h}^i$ and the free space field of its mirror dipole $\mathbf{h}^r$. The analytical expression for the free space field of a dipole is given by Equation (7.30). The larger the distance between the dipole and the interface $z = \pm D/2$, the smoother the term $\mathbf{h}^i + \mathbf{h}^r$ will be. Hence, for a smaller distance between the dipole and the interface, more waveguide modes will be needed to obtain an accurate solution. In order to get an a feeling for the accuracy, we compare a calculation with 2600 waveguide modes with a calculation of 960 waveguide modes. We consider the case of a dipole with $\mathbf{p} = (1, 1, 1)$, located a distance $\lambda/100$ above a cubic hole with size λ. When the transverse position of the dipole coincides with the (transverse) center of the hole, the difference between both calculations is 0.2%. When the transverse position of the dipole coincides with one of the edges of the hole, the difference is 5%. As remarked in Section 2.4, near the rim of the hole, the fields are very large and difficult to calculate. For most results shown in this chapter, the dipole is located far enough from the edges to have a relative error of less than one percent.

In the previous chapter we concluded that only the right-hand part of the system of equations that describes the scattering problem depends on the dipole. As most computation time is spent on the calculation of the interaction integral, it is clear that a dipole calculation will not take much time, if the interaction integrals were stored in a library. Then the time needed to calculate the relative spontaneous emission for dipole inside hole only takes a couple of seconds on a regular desk top computer. When the dipole is located above or below the perfectly conducting layer and the interaction integrals are known, the calculation takes about seven minutes.

8.3 A dipole inside a hole

In this section, a dipole is located at the center inside a square hole. The dipole is either oriented in the x-direction or in the z-direction. The thickness of the perfectly conducting layer is varied, as well as the width of the hole.

Figure 8.2 on the next page shows the relative spontaneous emission of a dipole oriented in the x-direction as a function of layer thickness, for four sizes of the width of the hole. For the smallest hole, $L_x = L_y = 2/5\lambda$, all waveguide modes are evanescent. See the tables in Appendix B for the propagation constants of the various modes. Therefore, increasing the layer thickness leads to an exponential decrease in the emitted radiation. For the larger holes, the lowest order waveguide modes are propagating. These modes are excited by the dipole, causing an energy flux away from the dipole, even if the layer thickness is large. This result is similar to the result shown in Figure 4.1 on page 45 in Section 4.2 for the energy flux through a hole as a function of layer thickness. In that section, the incident field was a plane wave. In both cases, the modulation of the energy flux with the layer thickness is the largest for the size of the hole that is the closest to the cutoff wavelength of the waveguide. As we noted in Chapter 4, a hole in a perfectly conducting layer is like a Fabry-Perot cavity. The closer the cavity is to cutoff, the larger is its quality factor. At a rough estimate, the spontaneous emission inside a cavity is linearly proportional to the quality factor [47]. Hence, we can use the above figure to estimate the quality factor of the shown geometries.

Figure 8.3 on page 86 shows polar plots of the far field Poynting vector in the radial direction. The dipole is again located at the center of a hole and oriented

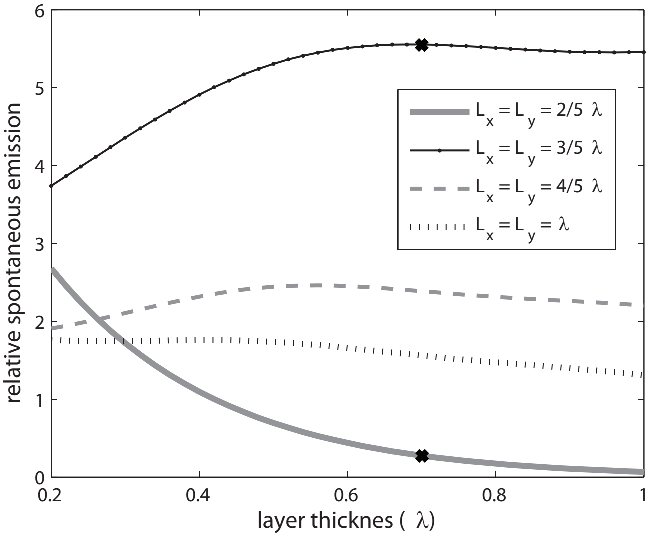

Figure 8.2: Relative spontaneous emission for a dipole inside a square hole as a function of the layer thickness. The dipole is located at the center of the hole and oriented in the x-direction.

along the x-direction. Results are shown for the (x,z) and the (y,z)-plane, for positive z. As a reference, the dashed gray lines show the corresponding Poynting vector for a dipole in free space. In the upper graphs, Figure 8.3(a), the width is $2/5\lambda$ and the layer thickness is 0.7λ. The energy flux is approximately four times smaller than the free space energy flux, except in the direction along the x-axis. The spontaneous emission for this case is indeed approximately one fourth of the spontaneous emission in free space (consider the lower cross in Figure 8.2).

Along the x-axis, an x-oriented free space dipole does not emit any radiation, and, as a consequence, the energy flux has the form of lobe in the polar plot in the (x,z)-plane. In the (y,z)-plane, the energy flux is constant with respect to the polar angle. For an x-oriented dipole inside a hole, it is just the other way around. No energy is radiated along the y-axis. The energy propagating along the x-axis is due to the electromagnetic surface waves, that are excited by the dipole.

The graphs in 8.3(b) on the next page show similar results for a hole with a width of $3/5\lambda$ and a layer thickness of 0.7λ. These are qualitatively comparable to the figures for a width of $2/5\lambda$. Quantitatively, the energy flux is approximately five times larger than the energy flux in free space, which agrees with a relative spontaneous emission of 5.5, indicated by the upper cross in Figure 8.2. Because for this width the lowest order waveguide mode is propagating, the energy flux has a maximum along the z-axis and is smaller (but non-zero) along the x-axis.

Figure 8.4 on page 87 is similar to Figure 8.2, but now the dipole is oriented along

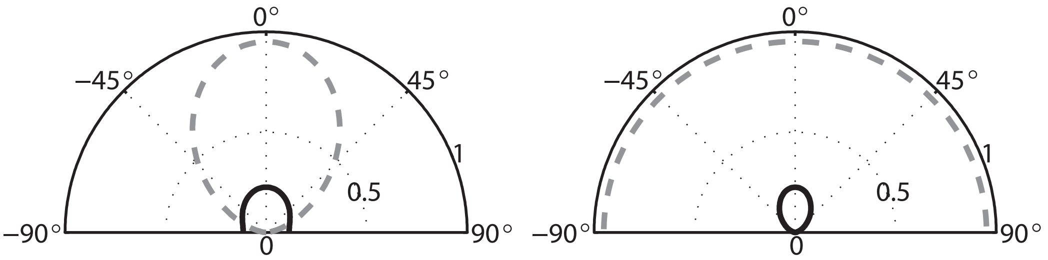

(a) $L_x = L_y = 2/5\lambda$, left: (x,z)-plane, right: (y,z)-plane

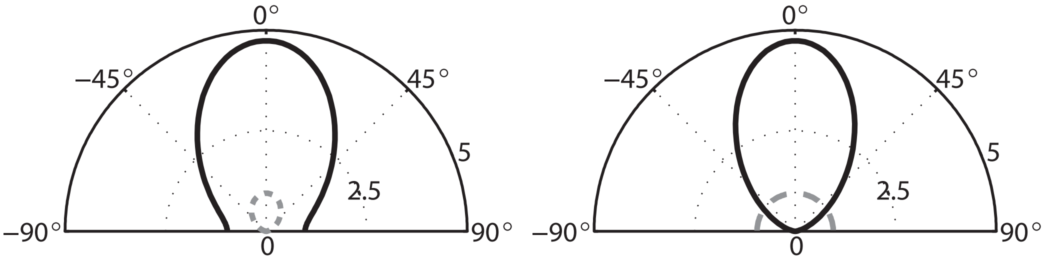

(b) $L_x = L_y = 3/5\lambda$, left: (x,z)-plane, right: (y,z)-plane

Figure 8.3: Polar plots of the energy flux in the radial direction in the far field, caused by an x-oriented dipole in the center of a hole (solid black line). The plots correspond to the crosses in Figure 8.2. The layer thickness for all figures is 0.7λ. The polar angle is the angle with the optical axis, the z-axis. The dashed gray line corresponds to the energy flux in the radial direction for an identical dipole in free space. Note the difference in scale (which is in arbitrary units) between the upper and lower graphs.

the z-direction. For this orientation, the relative spontaneous emission does not only show an exponential decrease for a hole width of $2/5\lambda$, but also for $3/5\lambda$. This is due to the fact that a z-oriented dipole can not excite waveguide modes that are TE polarized. The lowest order TM polarized waveguide mode has a larger cutoff than the lowest order TE mode: $\lambda/\sqrt{2}$ for TM and $\lambda/2$ for TE, for a square hole with width L. For a width of $4/5\lambda$, which is above cutoff for TM, the modulation of the relative spontaneous emission is the largest. The maximum is well over 7, for a layer thickness of 0.7λ. For this layer thickness, the z-component of the wavenumber (k_z) of the lowest order TM mode is 0.46 times the wavenumber. The effective wavelength of this mode in the z-direction is $2\pi/k_z = 2.14\lambda$. This effective wavelength is not an integer number times the layer thickness, so it seems that the maximum of the relative spontaneous emission is not due to constructive interference of this lowest order mode. In Figure 8.5, we plot the near field for a more detailed study.

Figure 8.5 on the facing page shows the absolute value of the electric field in the z-direction for a dipole oriented in the z-direction. The width of the hole is $4/5\lambda$

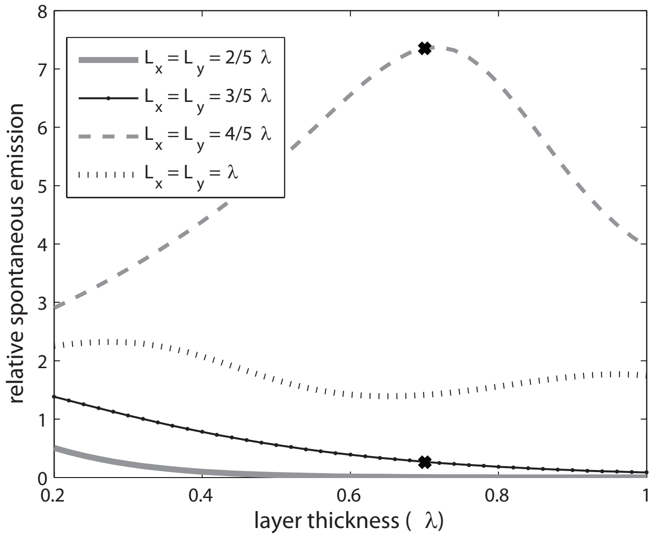

Figure 8.4: Relative spontaneous emission for a dipole inside a square hole as a function of the layer thickness. The dipole is located at the center of the hole and oriented in the z-direction.

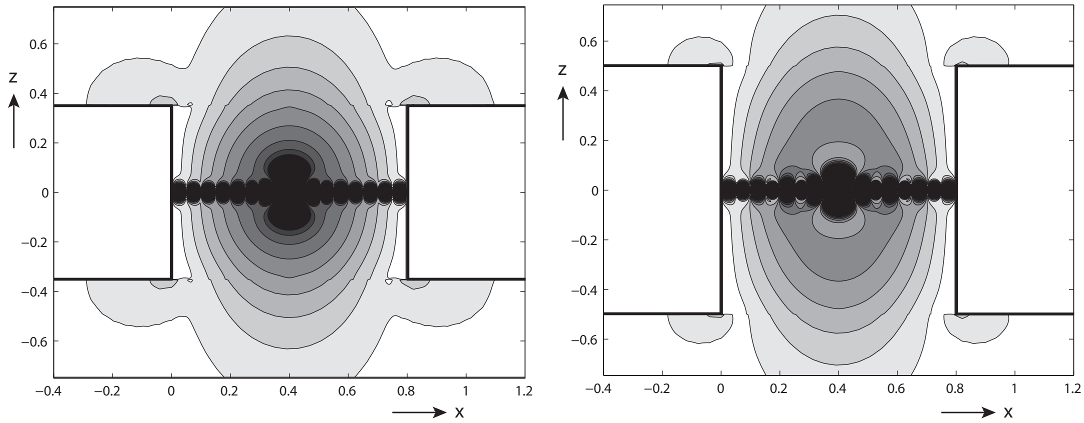

(a) Layer thickness is 0.7λ

(b) Layer thickness is λ

Figure 8.5: Gray scale plots of the absolute value of the z-component of the electric field in the (x, z)-plane. White denotes zero field strength, black maximum field strength. Both graphs have the same scaling. The dipole is located at the center of the hole, the orientation is along the z-axis. The width of the hole is $4/5\lambda$ for both graphs, the layer thickness is indicated in the captions. The scale in x and z-direction is in units of the wavelength.

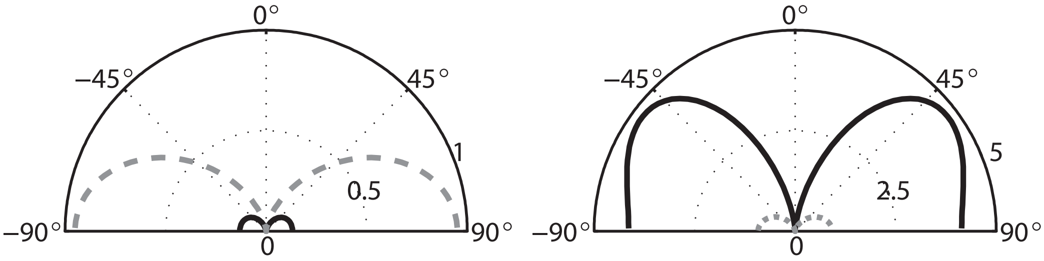

Figure 8.6: Polar plots of the energy flux in the radial direction in the far field, due to a z-oriented dipole in the center of a hole (solid black line). The plots correspond to the crosses in Figure 8.4: the width of the hole is $3/5\lambda$ in the left graph and $4/5\lambda$ in the right graph. The layer thickness is 0.7λ for both. The dashed gray line corresponds to the energy flux in the radial direction for an identical dipole in free space. The radial scale is in arbitrary units.

for both graphs, the layer thickness is 0.7λ in Figure 8.5(a) and λ in Figure 8.5(b). These correspond to a relative spontaneous emission of 7.5 and 4, respectively. The electric field strength is infinite at the location of the dipole. Hence, the black values near the dipole location do not mean that the field strength is constant, but, rather that the field strength is larger than the maximum value that was chosen for the graph. Both graphs have the same scaling and isolines are shown for equi-spaced values. The field strength is zero near the side walls of the hole, as it should be, because E_z is parallel to the perfect conductor. Near the edges just outside the hole, the field strength has a maximum, as is expected from the theory of diffraction near edges [12]. Inside the hole, along the line parallel to the x-axis and with $z = 0$, the field has fifteen maxima. That is due to the fact that the highest order modes that are taken into account in the calculation also have fifteen maxima. These higher order modes only dominate the field near the dipole, though. For the case of a layer thickness of 0.7λ, which has the highest relative spontaneous emission, the field strength decreases monotonically away from the dipole, but for a layer thickness of λ, minima are seen at the upper and lower side of the dipole, just above and below the black lobes.[3]

Figure 8.6 shows polar plots of the far field Poynting vector in the radial direction, for a z-oriented dipole. The dipole is again located at the center of the hole. We only show the Poynting vector in the (x, z)-plane, as the figures would be identical in the (y, z)-plane, due to the symmetry of the setup. The graph on the left corresponds to the lower cross in Figure 8.4 on the preceding page: the width of the hole is $3/5\lambda$ and the layer thickness is 0.7λ. The graph on the right corresponds to

---

[3] Once more, we checked the influence of taking into account more waveguide modes in the calculation. The difference in the relative spontaneous emission for the case of a dipole oriented in the z-direction, located at the center of a hole with width $4/5\lambda$ and layer thickness 0.7λ is 0.2% for 960 and 2600 waveguide modes.

the upper cross in Figure 8.4: the width of the hole is $4/5\lambda$ and the layer thickness is again 0.7λ. The free space energy flux is plotted as a gray dashed line. A free space dipole oriented in the z-direction does not emit radiation along the z-axis and emits most radiation along the (x, y)-plane. A z-oriented dipole inside a hole also does not emit radiation along the z-axis. However, depending on the size of the hole, the maximum in energy flux does not need to be along the (x, y)-plane.

8.4 A dipole above a pit

In this section, a dipole is located above a square hole, such that the x and y-coordinate of the dipole coincide with the x and y-coordinate of the center of the pit. The distance between the dipole and the upper plane of the layer is fixed at $\lambda/10$. The dipole is either oriented in the x-direction or in the z-direction. The thickness of the perfectly conducting layer is varied, as well as the width of the pit.

Figure 8.7(a) shows the relative spontaneous emission of a dipole that is oriented in the x-direction as a function of the depth of the pit, for four sizes of the width of the hole. In Figure 8.7(b) the dipole is oriented in the z-direction. When the pit has zero depth, the interface is flat. The x-oriented dipole is out of phase with its mirror dipole and the spontaneous emission goes to zero if the dipole approaches the interface. The z-oriented dipole is in phase with its mirror dipole and, hence, the spontaneous emission is doubled if the dipole is placed at the interface. For the smallest pit width, $L_x = L_y = 2/5\lambda$, all waveguide modes are evanescent and the relative spontaneous emission increases (upper figure) or decreases (lower figure) with the pit depth, up to a depth beyond which nothing changes. This depth is 0.4λ for the upper figure and 0.2λ for the lower figure. The lowest order waveguide mode (TE, $(m_x, m_y) = (1,0)$ or $(0,1)$), that can be excited by an x-polarized dipole has a penetration depth that is approximately twice as large as the lowest order mode that can be excited by a z-oriented dipole (TM, $(m_x, m_y) = (1,1)$). For the case of a z-oriented dipole above a pit with a width of $3/5\lambda$, all TM modes are again evanescent, however, the spontaneous emission is seen to increase slightly for a pit depth between 0.8λ and λ. For the wider pits, the modulation of the spontaneous emission with pit depth is oscillating, although the effect is not very large for the z-oriented dipole. The amplitude of this oscillation is the smallest for the widest pits. For a z-oriented dipole above a pit with a width of $4/5\lambda$, the spontaneous emission has the smallest value for a pit depth of 0.44λ. The radiation pattern of this setup, as well as the radiation patterns of two other setups (indicated by a cross in Figure 8.7) are shown in Figure 8.8.

The polar plot on the left in Figure 8.8 shows the radiation pattern of an x-oriented dipole, for the case indicated by the cross in Figure 8.7(a). Hence, the width is $3/5\lambda$ and the depth of the pit is 0.84λ. The distance from the dipole to the bottom of the pit is 0.94λ. The relative spontaneous emission for this setup is 0.25. The solid

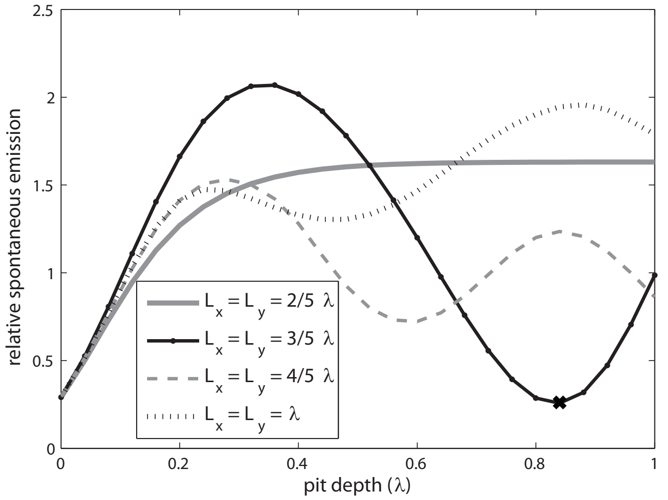

(a) $\mathbf{p} = (1, 0, 0)$

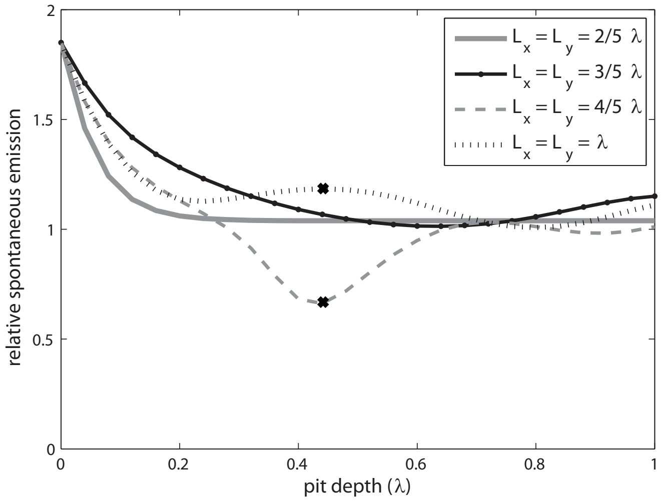

(b) $\mathbf{p} = (0, 0, 1)$

Figure 8.7: Relative spontaneous emission for a dipole above a square pit as a function of the pit depth. The x and y-coordinate of the dipole coincide with x and y-coordinate of the center of the pit. The z-coordinate is $\lambda/10$ above the interface. The dipole is oriented in the x-direction (top) or in the z-direction (bottom).

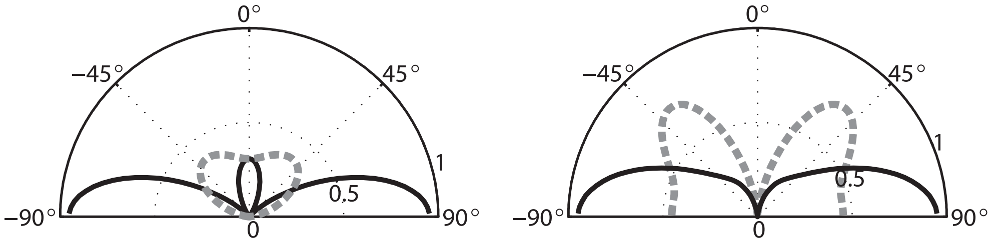

Figure 8.8: Left: radiation pattern of a dipole with strength $\mathbf{p} = (1,0,0)$ located at a distance $\lambda/10$ above the layer with a square pit. The depth of the pit is 0.84λ and $L_x = L_y = 3/5\lambda$ for both lines. The solid black line is the radiation pattern in the (x,z)-plane and the dashed gray line is the radiation pattern in the (y,z)-plane. See the cross in Figure 8.7(a). Right: radiation pattern of a dipole with strength $\mathbf{p} = (0,0,1)$ located at a distance $\lambda/10$ above the layer with a square pit. The solid black line corresponds to a depth of 0.44λ and $L_x = L_y = \lambda$. The dashed gray line corresponds to the same depth and $L_x = L_y = 4/5\lambda$. See the crosses in Figure 8.7(b). The scale in the radial direction is not identical for the left and right graphs.

black line is the radiation pattern in the (x,z)-plane and the dashed gray line is the radiation pattern in the (y,z)-plane. In the (x,z)-plane, the radiation pattern shows three lobes, two of which along the interface. These are due to surface waves that the dipole excites at the edges of the pit. A smaller lobe of radiation is directed along the z-axis, and no radiation is emitted at an angle of approximately 37° with the z-axis. For this direction, the radiation in the (y,z)-plane has a maximum. Together with zero radiation along the interface, this results in a heart shaped radiation pattern in the (y,z)-plane.

The polar plot on the right shows the radiation pattern of a z-oriented dipole. For both lines the depth of the pit is 0.44λ. For the solid black line the width is λ and for the dashed gray line the width is $4/5\lambda$. See the two crosses in Figure 8.7(b). Results are shown for the (x,z)-plane, but because of the symmetry, this is not different from the result in the (y,z)-plane. No radiation is emitted along the z-axis. For the larger hole, most of the energy is emitted along the interface, while for the smaller hole, the emitted radiation has a maximum at an angle of approximately 38° with the z-axis.

8.5 Relative spontaneous emission near a hole

Figure 8.9 on the next page shows the relative spontaneous emission of a dipole in gray levels. The dipole is oriented in the x-direction. The gray value at each position gives the relative spontaneous emission when the dipole is placed at that

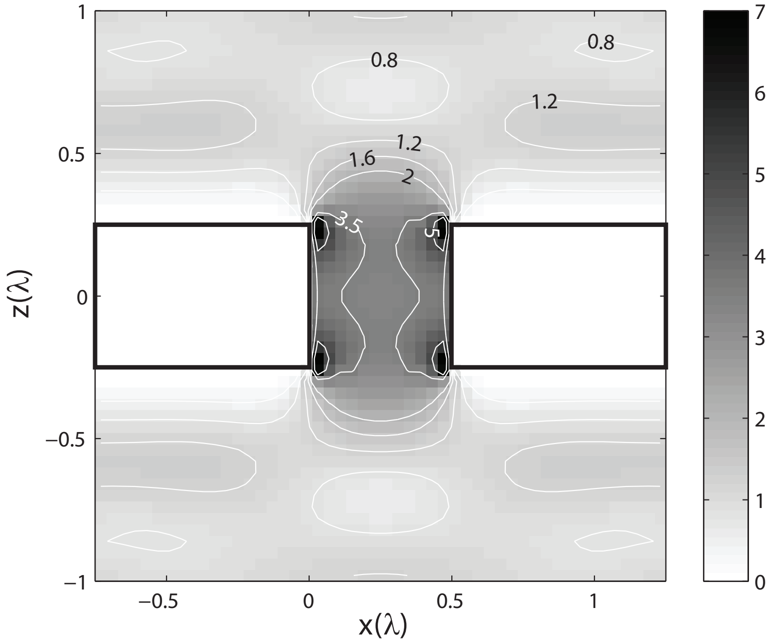

(a) (x, z)-plane

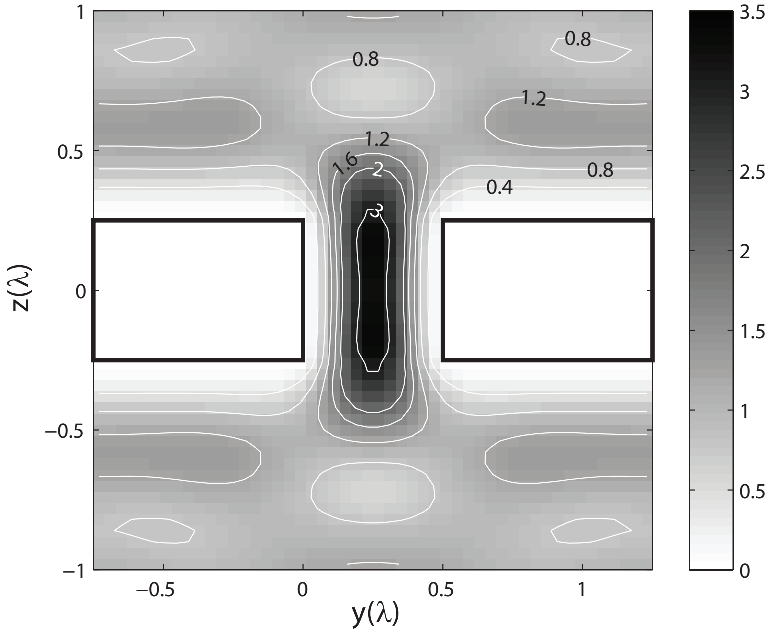

(b) (y, z)-plane

Figure 8.9: Gray scale figures of the relative spontaneous emission for an x-oriented dipole as a function of the position, near a hole. The hole is cubic: $L_x = L_y = D = \lambda/2$. Isolines are drawn for various values. Note that the gray scale for both figures is different.

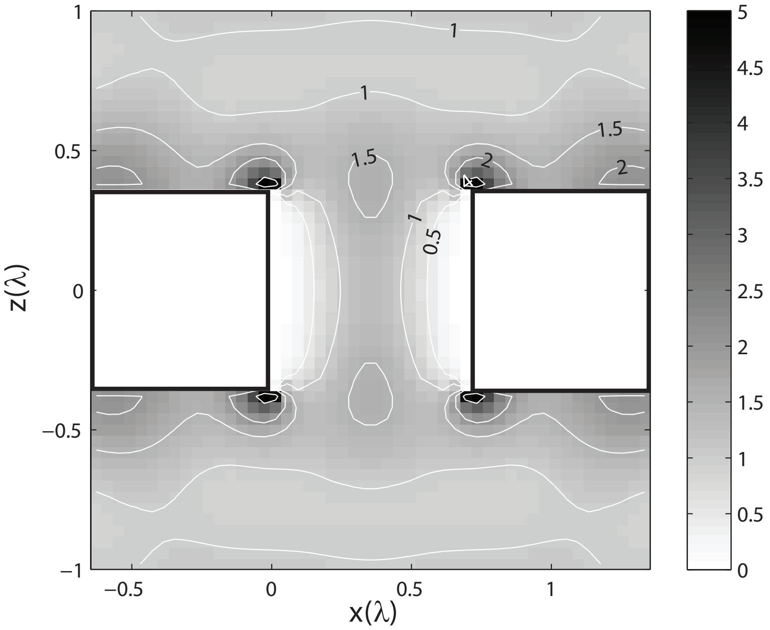

Figure 8.10: Gray scale figure of the relative spontaneous emission for a z-oriented dipole as a function of the position, near a hole. The hole is cubic: $L_x = L_y = D = \lambda/\sqrt{2}$.

position. The hole is cubic, with the dimension chosen such that it is exactly at cutoff for the lowest order waveguide mode that an x-oriented dipole can excite, which is the lowest TE mode. Thus, the size is $\lambda/2$. The upper graph shows the relative spontaneous emission in the (x,z)-plane, where the y-coordinate coincides with the center of the hole. At a distance of $\lambda/100$ from the conducting layer, close to the edges, the relative spontaneous emission has a maximum of 7. Even closer to the edge, the emission will be larger, of course, because the fields are infinite near perfectly sharp edges. In the center of the hole, the relative spontaneous emission is 3. Just above and below the layer, the emission vanishes, because of the mirror dipole that has an opposite phase. The destructive and constructive interference of the dipole and its mirror dipole, further away from the layer, are best visible in the lower graph, which shows the (y,z)-plane. The gray scaling here is different from the upper graph. In this plane, inside the hole, near the walls, the spontaneous emission is zero, because the dipole is tangential to the perfectly conducting surface. From these figures, we can conclude that the quality factor of this hole is 3, although this is not expected to be true for a z-oriented dipole.

Figure 8.10 is similar to the previous graphs, but now the dipole is oriented in the z-direction and the size of the cubic hole is chosen such that it is at cutoff for the lowest order waveguide mode that a z-oriented dipole can excite: the lowest order TM mode. Hence, the size is $\lambda/\sqrt{2}$. As the setup is symmetric for this dipole orientation, we only show the (x, z)-plane. Close to the edges, the spontaneous emission is again the highest; we find a value of 5 at a distance of $\lambda/100$ from the edge. Inside the hole near the walls, the emission is zero because the orientation of the dipole is parallel to the perfectly conducting wall. In the center of the hole, the relative spontaneous emission is not that high: 1.2. At the upper and lower side of the layer, the furthest away from the edge, the relative spontaneous emission is 2, because the dipole and its mirror dipole have the same strength and are in phase.

Chapter 9

Conclusions

9.1 The mode expansion method

In this thesis we have presented a mode expansion theory to model the scattering from three-dimensional pits and holes in a perfectly conducting metal layer. The metal layer has a finite thickness and the sizes of the holes and pits are of the same order of magnitude as the wavelength of the scattering light.

Our model is called a mode expansion theory because the electromagnetic fields inside the pits and holes are expanded in terms of waveguide modes. These waveguide modes are propagating or evanescent and can have two different polarizations. Any electromagnetic field inside the pits and holes can be written in terms of this infinite set of waveguide modes. Similarly, the electromagnetic fields above and below the metal layer are expanded into plane waves. These plane waves can be propagating or evanescent and can also have two different polarizations. The reader will not be surprised that any electromagnetic field above or below the layer can be written in terms of the plane waves. Hence, with these two expansions of the electromagnetic field, we have a rigorous description of our scattering problem.

A system of equations is derived by matching the tangential field components at the interfaces. The expansion coefficients for the plane waves are eliminated from the system of equations, such that the only unknowns are the expansion coefficients of the waveguide modes. Hence, the number of unknowns is small.

This mode expansion theory is not new. It has been used to calculate the scattering of a plane wave by a single, circular hole in a thick metal plate. However, we have extended the theory to the case of multiple pits and holes, as well as a two-dimensional periodic array of pits and holes.

Another extension of the theory is related to the source of electromagnetic radiation. Usually, the incident field consists of a plane wave or a continuum of plane waves. These originate from a (not specified) source located at infinity. Our model, in addition, allows for an oscillating electric dipole as the source of electromagnetic radiation. This dipole can be located inside a pit or hole, as well as above or below the perfectly conducting layer.

In the numerical implementation, we truncate the series of waveguide modes. The system of equations that describes the diffraction problem then consists of a coefficient matrix, a vector containing the unknowns, and a right hand part. The right hand part is the driving term and arises from the incident field. The coefficient matrix contains the so-called interaction integrals.

These integrals describe the interaction of one waveguide mode, via the plane waves, with another waveguide mode in the same or in another pit or hole. Most computation time is spent on the computation of these interaction integrals, as these may contain violently oscillating and singular (but integrable) factors. However, once the interaction integrals are computed for a specific diffraction geometry, important parameters such as the thickness of the conducting layer and the index of refraction inside the pit or hole can be varied with negligible computational effort. Moreover, the incident field can be changed without the need to recompute the interaction integrals. It is thus very useful to construct a library of interaction integrals for various scattering geometries.

The number of waveguide modes that is needed to have an accurate representation of the field is found to be around 400 per pit or hole, when the width of the hole is not larger than twice the wavelength. If the thickness of the conducting layer is more than an order of magnitude smaller than the wavelength, a higher number of waveguide modes must be taken into account. The reason for this is that the expansion by waveguide modes of the infinite electromagnetic fields, that occur near infinitely sharp edges, does not converge very quickly. This is a problem, however, that is difficult to solve for any numerical computational scheme. For most scattering problems that are treated in this thesis, the number of 400 waveguide modes was sufficient to obtain a relative error in the energy of less than one percent. For this number, it takes a few hours to calculate the interaction integrals. Solving the actual system of equations takes only a few seconds or less on a normal desktop computer.

The method presented in this thesis has two drawbacks. The first is the inflexibility regarding the geometry. We have only used rectangular pits and holes. For these, the waveguide modes consist of trigonometric functions. For other regular shapes, such as circular and elliptical cylinders, the waveguide modes are analytical functions such as Bessel functions and Mathieu functions. For more exotic shapes, the waveguide modes must be determined numerically.

The second drawback is the assumption of perfect conductivity. Whether this assumptions is justified, depends on the wavelength and material that are modeled. If the skin depth is small compared with the wavelength, the perfect conductor assumption is valid. This is for example the case for terahertz and microwave frequencies. For optical frequencies, the perfect conductor assumption is not entirely justified. However, we think that the model is still of qualitative value. Apart from absorption of energy in the metal, all relevant physics is present in the model. This also includes the surface plasmon equivalent of a perfect conductor: an electromagnetic surface wave.

Besides the small number of unknowns and the modest memory demands regarding numerical computation, the most important advantage of the mode expansion method has a more cognitive nature. The expansion of the electromagnetic field in eigenfunctions (plane waves and waveguide modes) helps in obtaining a physical interpretation of the scattering problem. Consequently, the mode expansion technique is very suitable for theoretical electromagnetic scattering experiments.

9.2 Calculations

We have compared calculations, obtained with our mode expansion technique, with experimental results on the scattering of a terahertz pulse. The near field of this pulse was measured at the shadow side of an aluminum foil with square holes. Our calculations are in excellent agreement with these near field measurements. Therefore, we can conclude that the mode expansion theory is effective and that the numerical implementation is reliable.

We have studied the transmission of energy through single and multiple holes and compared this to the energy that is incident on the hole. We have found that there are two mechanisms that can lead to enhanced or decreased transmission. The first is related to the Fabry-Perot resonance of waveguide modes inside a hole. Extraordinary transmission can occur for a single hole when the lowest order waveguide mode is just above cutoff. For the second mechanism to occur, the presence of a second hole or pit is needed. Depending on the polarization of the incident light, electromagnetic surface waves can be excited by the scattering from the second hole or pit and these waves can enhance or decrease the transmission through the first hole.

We have studied the behavior of optical vortices inside holes as well as the transmission of angular momentum through holes. We used a Laguerre-Gaussian mode as incident field. We have found that, as degree theory predicts, the total topological charge in a plane inside the hole can change only if a vortex either appears or disappears via the walls of the hole. If this is not the case, the total topological charge is conserved. This means that pairs of oppositely handed vortices may appear abruptly within the area of the hole. When studying the transmission of angular momentum of a hole, we have found that, depending on the size of the hole and the thickness of the conducting layer, angular momentum can be transferred from the field to the surface currents of the perfect conductor. However, angular momentum can also be transferred from the currents to the field.

We have used our model with the dipole as the source of electromagnetic radiation to carry out spontaneous emission calculations. A dipole that is oriented in the plane of the conducting layer excites other waveguide modes than a dipole that is oriented perpendicular to the conducting layer. As a consequence, the relative spontaneous emission of a parallel dipole is reduced for pits and holes with a width that is smaller than half the wavelength λ. For a perpendicular dipole, the relative spontaneous emission is reduced when the width is smaller than $\lambda/\sqrt{2}$. The spontaneous emission can be enhanced by a factor 3 to 5 if the size of the hole or pit is chosen well. Close to the edges of the holes, however, the relative spontaneous emission can be orders of magnitude larger, due to the infinite fields that occur near sharp edges.

Appendix A

The interaction integral

In this appendix we elaborate on the interaction integral that describes the interaction of waveguide mode $\bar{\boldsymbol{\alpha}}$, via the scattered field through operator $\mathscr{A}$, with another waveguide mode $\bar{\boldsymbol{\alpha}}'$. We will first write out the integral, then we will discuss some symmetry properties and, finally, the numerical implementation.

A.1 Calculation of the interaction integral

The interaction integral is given by:

$$\begin{aligned}\left\langle \mathscr{A}\left(\boldsymbol{v}_{\bar{\boldsymbol{\alpha}}}\right) \middle| \boldsymbol{v}_{\bar{\boldsymbol{\alpha}}'} \right\rangle_{\Omega_{p'}} = &\int\limits_{-\infty}^{\infty} \frac{k_z}{\omega\mu_0} \left\langle \boldsymbol{v}_{\bar{\boldsymbol{\alpha}}} \middle| \boldsymbol{v}^{\mathrm{S}}_{\beta_2} \right\rangle_{\Omega_p} \left\langle \boldsymbol{v}_{\bar{\boldsymbol{\alpha}}'} \middle| \boldsymbol{v}^{\mathrm{S}}_{\beta_2} \right\rangle^*_{\Omega_{p'}} \mathrm{d}\beta_2 \\ &+ \int\limits_{-\infty}^{\infty} \frac{\omega\varepsilon\varepsilon_0}{k_z} \left\langle \boldsymbol{v}_{\bar{\boldsymbol{\alpha}}} \middle| \boldsymbol{v}^{\mathrm{P}}_{\beta_2} \right\rangle_{\Omega_p} \left\langle \boldsymbol{v}_{\bar{\boldsymbol{\alpha}}'} \middle| \boldsymbol{v}^{\mathrm{P}}_{\beta_2} \right\rangle^*_{\Omega_{p'}} \mathrm{d}\beta_2. \end{aligned} \tag{A.1}$$

Please recall that $\beta_2 = (k_x, k_y)$ and that $\int \mathrm{d}\beta_2 = \iint \mathrm{d}k_x\, \mathrm{d}k_y$. We consider one of the scalar products, with $\boldsymbol{\beta} = (\beta_1, \beta_2)$ and $\beta_1 = \mathrm{S}, \mathrm{P}$:

$$\begin{aligned}\left\langle \boldsymbol{v}_{\bar{\boldsymbol{\alpha}}} \middle| \boldsymbol{v}_{\boldsymbol{\beta}} \right\rangle_{\Omega_p} &= \int\limits_{x_0^p}^{x_0^p+L_x^p} \int\limits_{y_0^p}^{y_0^p+L_y^p} \boldsymbol{v}_{\bar{\boldsymbol{\alpha}}}(x,y) \cdot \boldsymbol{v}_{\boldsymbol{\beta}}(x,y)^*\, \mathrm{d}x\, \mathrm{d}y, \\ &= e^{-i\left(k_x x_0^p + k_y y_0^p\right)} \int\limits_0^{L_x^p} \int\limits_0^{L_y^p} \boldsymbol{v}_{\bar{\boldsymbol{\alpha}}}(\bar{x}_p, \bar{y}_p) \cdot \boldsymbol{v}_{\boldsymbol{\beta}}(\bar{x}_p, \bar{y}_p)^*\, \mathrm{d}\bar{x}_p\, \mathrm{d}\bar{x}_p, \end{aligned} \tag{A.2}$$

where we have changed to local coordinates. This final double integral is in fact a Fourier integral that can be calculated analytically:

$$
\begin{aligned}
F_{\tilde{\boldsymbol{\alpha}}}^{\beta_1}(k_x,k_y) &\equiv \int_0^{L_x^p}\int_0^{L_y^p} \boldsymbol{v}_{\tilde{\boldsymbol{\alpha}}}(\bar{x}_p,\bar{y}_p)\cdot\boldsymbol{v}_{\boldsymbol{\beta}}(\bar{x}_p,\bar{y}_p)^*\,\mathrm{d}\bar{x}_p\,\mathrm{d}\bar{x}_p,\\
&= \frac{\Lambda_{\boldsymbol{\alpha}}\Lambda_{\boldsymbol{\beta}}}{\Gamma_{\boldsymbol{\alpha}}\Gamma_{\boldsymbol{\beta}}}\begin{cases}
\gamma_y k_y\, c_{m_x}^p(k_x)\, s_{m_y}^p(k_y) + \gamma_x k_x\, s_{m_x}^p(k_x)\, c_{m_y}^p(k_y), & \alpha_2 = \mathrm{TE},\ \beta_1 = \mathrm{S},\\
\gamma_x k_y\, c_{m_x}^p(k_x)\, s_{m_y}^p(k_y) - \gamma_y k_x\, s_{m_x}^p(k_x)\, c_{m_y}^p(k_y) = 0, & \alpha_2 = \mathrm{TM},\ \beta_1 = \mathrm{S},\\
\gamma_y k_x\, c_{m_x}^p(k_x)\, s_{m_y}^p(k_y) - \gamma_x k_y\, s_{m_x}^p(k_x)\, c_{m_y}^p(k_y), & \alpha_2 = \mathrm{TE},\ \beta_1 = \mathrm{P},\\
\gamma_x k_x\, c_{m_x}^p(k_x)\, s_{m_y}^p(k_y) + \gamma_y k_y\, s_{m_x}^p(k_x)\, c_{m_y}^p(k_y), & \alpha_2 = \mathrm{TM},\ \beta_1 = \mathrm{P},
\end{cases}
\end{aligned}
\tag{A.3}
$$

where the functions $c_{m_j}^p$ and $s_{m_j}^p$ with subscript $j = x, y$ are given by:

$$
c_{m_j}^p(k_j) \equiv \int_0^{L_j^p} \cos(\gamma_j z) e^{-ik_j z}\mathrm{d}z = \begin{cases}
\dfrac{ik_j}{\gamma_j^2 - k_j^2}\left[1 - (-1)^{m_j} e^{-ik_j L_j}\right], & k_j \neq \pm\gamma_j,\\
\tfrac{1}{2}L_j, & k_j = \pm\gamma_j,\ k_j \neq 0,\\
L_j, & k_j = \gamma_j = 0,
\end{cases}
\tag{A.4a}
$$

$$
s_{m_j}^p(k_j) \equiv \int_0^{L_j^p} \sin(\gamma_j z) e^{-ik_j z}\mathrm{d}z = \begin{cases}
\dfrac{\gamma_j}{\gamma_j^2 - k_j^2}\left[1 - (-1)^{m_j} e^{-ik_j L_j}\right], & k_j \neq \pm\gamma_j,\\
\mp\tfrac{1}{2}iL_j, & k_j = \pm\gamma_j,\ k_j \neq 0,\\
0, & k_j = \gamma_j = 0.
\end{cases}
\tag{A.4b}
$$

Note that $F_{\tilde{\boldsymbol{\alpha}}}^{\beta_1}(k_x,k_y)$ is zero for all (k_x,k_y) when the waveguide mode is TM polarized and the plane wave is S-polarized. Hence, these polarizations do not interact. For the interaction integral we now have:

$$
\begin{aligned}
\left\langle \mathscr{A}(\boldsymbol{v}_{\tilde{\boldsymbol{\alpha}}}) \middle| \boldsymbol{v}_{\tilde{\boldsymbol{\alpha}}'} \right\rangle_{\Omega_{p'}} = &\int_{-\infty}^{\infty}\int_{-\infty}^{\infty} \frac{k_z}{\omega\mu_0}\, e^{i(k_x\Delta_x + k_y\Delta_y)}\, F_{\tilde{\boldsymbol{\alpha}}}^{\mathrm{S}}(k_x,k_y)\, F_{\tilde{\boldsymbol{\alpha}}'}^{\mathrm{S}}(k_x,k_y)^*\,\mathrm{d}k_x\mathrm{d}k_y,\\
&+ \int_{-\infty}^{\infty}\int_{-\infty}^{\infty} \frac{\omega\varepsilon\varepsilon_0}{k_z}\, e^{i(k_x\Delta_x + k_y\Delta_y)}\, F_{\tilde{\boldsymbol{\alpha}}}^{\mathrm{P}}(k_x,k_y)\, F_{\tilde{\boldsymbol{\alpha}}'}^{\mathrm{P}}(k_x,k_y)^*\,\mathrm{d}k_x\mathrm{d}k_y,
\end{aligned}
\tag{A.5}
$$

with $\Delta_x = x_0^{p'} - x_0^p$ and $\Delta_y = y_0^{p'} - y_0^p$, the distance between pit p' and p. From the above equation it is clear that this double integral is difficult for two reasons. First, the factor $\exp\left[i\left(k_x\Delta_x + k_y\Delta_y\right)\right]$ oscillates violently when pit p' and p are far apart. Second, the factor k_z^{-1} is singular for $k_x^2 + k_y^2 = k^2$. The integrand is still integrable, but care has to be taken.

A.2 Symmetry properties of the interaction integral

We introduce a short notation for the integrand of the interaction integral (A.5):

$$\begin{aligned} I_{\bar{\boldsymbol{\alpha}}\bar{\boldsymbol{\alpha}}'}(k_x, k_y) \equiv{}& \frac{k_z}{\omega\mu_0}\, e^{i(k_x\Delta_x + k_y\Delta_y)}\, F^{\mathrm{S}}_{\bar{\boldsymbol{\alpha}}}(k_x, k_y)\, F^{\mathrm{S}}_{\bar{\boldsymbol{\alpha}}'}(k_x, k_y)^* \\ &+ \frac{\omega\varepsilon\varepsilon_0}{k_z}\, e^{i(k_x\Delta_x + k_y\Delta_y)}\, F^{\mathrm{P}}_{\bar{\boldsymbol{\alpha}}}(k_x, k_y)\, F^{\mathrm{P}}_{\bar{\boldsymbol{\alpha}}'}(k_x, k_y)^*. \end{aligned} \tag{A.6}$$

This integrand has the following properties:

$$I_{\bar{\boldsymbol{\alpha}}\bar{\boldsymbol{\alpha}}'}(-k_x, -k_y) = \begin{cases} I_{\bar{\boldsymbol{\alpha}}\bar{\boldsymbol{\alpha}}'}(k_x, k_y)^*, & \text{for } k_x^2 + k_y^2 \leq k^2, \\ -I_{\bar{\boldsymbol{\alpha}}\bar{\boldsymbol{\alpha}}'}(k_x, k_y)^*, & \text{for } k_x^2 + k_y^2 > k^2. \end{cases} \tag{A.7}$$

This means that the integration area reduces to two quadrants. Furthermore, inside the k-circle ($k_x^2 + k_y^2 < k^2$), we only have to calculate the real part of the integrand, and outside the k-circle we only have to calculate the imaginary part:

$$\begin{aligned} \int_{-\infty}^{\infty}\int_{-\infty}^{\infty} I_{\bar{\boldsymbol{\alpha}}\bar{\boldsymbol{\alpha}}'}(k_x, k_y)\,\mathrm{d}k_x\mathrm{d}k_y = 2 & \iint\limits_{\substack{k_x^2+k_y^2\leq k^2 \\ k_x\geq 0}} \mathrm{Re}\left[I_{\bar{\boldsymbol{\alpha}}\bar{\boldsymbol{\alpha}}'}(k_x, k_y)\right]\mathrm{d}k_x\mathrm{d}k_y \\ & + 2i \iint\limits_{\substack{k_x^2+k_y^2> k^2 \\ k_x\geq 0}} \mathrm{Im}\left[I_{\bar{\boldsymbol{\alpha}}\bar{\boldsymbol{\alpha}}'}(k_x, k_y)\right]\mathrm{d}k_x\mathrm{d}k_y, \end{aligned} \tag{A.8}$$

where $\mathrm{Re}(z)$ and $\mathrm{Im}(z)$ denote the real and the imaginary part of the complex number z. The integrand also has the following property, regarding the interchanging of the two modes $\bar{\boldsymbol{\alpha}}$ and $\bar{\boldsymbol{\alpha}}'$:

$$I_{\bar{\boldsymbol{\alpha}}'\bar{\boldsymbol{\alpha}}}(k_x, k_y) = \begin{cases} I_{\bar{\boldsymbol{\alpha}}\bar{\boldsymbol{\alpha}}'}(k_x, k_y)^*, & \text{for } k_x^2 + k_y^2 \leq k^2, \\ -I_{\bar{\boldsymbol{\alpha}}\bar{\boldsymbol{\alpha}}'}(k_x, k_y)^*, & \text{for } k_x^2 + k_y^2 > k^2. \end{cases} \tag{A.9}$$

Combining the properties (A.8) and (A.9), we find that the interaction integral of mode $\bar{\boldsymbol{\alpha}}$ with mode $\bar{\boldsymbol{\alpha}}'$ is equal to the interaction integral of mode $\bar{\boldsymbol{\alpha}}'$ with mode $\bar{\boldsymbol{\alpha}}$:

$$\left\langle \mathscr{A}\left(\boldsymbol{v}_{\bar{\boldsymbol{\alpha}}}\right) \middle| \boldsymbol{v}_{\bar{\boldsymbol{\alpha}}'} \right\rangle_{\Omega_{p'}} = \left\langle \mathscr{A}\left(\boldsymbol{v}_{\bar{\boldsymbol{\alpha}}'}\right) \middle| \boldsymbol{v}_{\bar{\boldsymbol{\alpha}}} \right\rangle_{\Omega_{p}}. \tag{A.10}$$

Hence, we only have to calculate half of the interaction integrals. When these interaction integrals are elements of a matrix, this means that interchanging $\bar{\boldsymbol{\alpha}}$ and $\bar{\boldsymbol{\alpha}}'$ corresponds to transposing the matrix.[1]

---

[1] If the half spaces above and below the perfectly conducting layer are filled with the same dielectric ($n_u = n_\ell$), then an interaction integral at $z = D/2$ is minus this interaction integral at $z = -D/2$.

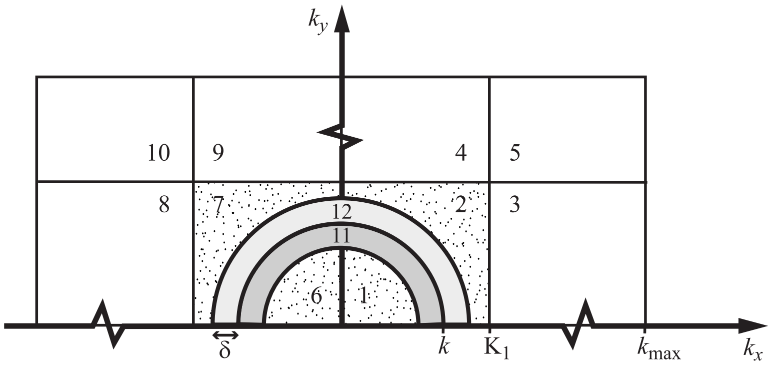

Figure A.1: The division of the integration area into 12 domains. Not on scale.

The above properties are valid for every interaction integral. Now we assume that the holes or pits, in which mode $\bar{\boldsymbol{\alpha}}$ and $\bar{\boldsymbol{\alpha}}'$ live, have the same size ($L_x^p = L_x^{p'} = L_x, L_y^p = L_y^{p'} = L_y$). Without proof, we state the following relation between the interaction integral of mode $(\alpha_1, \alpha_2, \alpha_3)$ and mode $(\alpha_1', \alpha_2', \alpha_3')$ and the interaction integral of mode $(\alpha_1', \alpha_2', \alpha_3)$ and mode $(\alpha_1, \alpha_2, \alpha_3')$:

$$\left\langle \mathscr{A}\left(\boldsymbol{v}_{\bar{\boldsymbol{\alpha}}'}\right) \middle| \boldsymbol{v}_{\bar{\boldsymbol{\alpha}}} \right\rangle_{\Omega_{p'}} = (-1)^{m_x + m_x'} (-1)^{m_y + m_y'} \left\langle \mathscr{A}\left(\boldsymbol{v}_{\bar{\boldsymbol{\alpha}}}\right) \middle| \boldsymbol{v}_{\bar{\boldsymbol{\alpha}}'} \right\rangle_{\Omega_{p'}}. \tag{A.11}$$

Note that, in this relation, on both sides of the equal sign, the integration is over the area of pit or hole p', whereas in Equation (A.10), the integrations on the two sides of the equal sign are over different areas. When, in addition, either Δ_x or Δ_y or both are zero, then the interaction integral can be zero, depending on α_3 and α_3':

$$\Delta_x = 0, \Delta_y \neq 0: \quad \left\langle \mathscr{A}\left(\boldsymbol{v}_{\bar{\boldsymbol{\alpha}}}\right) \middle| \boldsymbol{v}_{\bar{\boldsymbol{\alpha}}'} \right\rangle_{\Omega_{p'}} = 0, \quad \text{for } m_x + m_x' \text{ odd}, \tag{A.12a}$$

$$\Delta_x \neq 0, \Delta_y = 0: \quad \left\langle \mathscr{A}\left(\boldsymbol{v}_{\bar{\boldsymbol{\alpha}}}\right) \middle| \boldsymbol{v}_{\bar{\boldsymbol{\alpha}}'} \right\rangle_{\Omega_{p'}} = 0, \quad \text{for } m_y + m_y' \text{ odd}, \tag{A.12b}$$

$$\Delta_x = \Delta_y = 0: \quad \left\langle \mathscr{A}\left(\boldsymbol{v}_{\bar{\boldsymbol{\alpha}}}\right) \middle| \boldsymbol{v}_{\bar{\boldsymbol{\alpha}}'} \right\rangle_{\Omega_{p'}} = 0, \quad \text{for } m_x + m_x' \text{ odd or } m_y + m_y' \text{ odd}. \tag{A.12c}$$

In the third case, hence when $\Delta_x = \Delta_y = 0$, which means that the two modes live in the same pit or hole, the integration area is reduced to one quadrant because then the integrand is even in k_x and k_y.

A.3 Numerical computation of the interaction integral

Since we have to calculate a lot of interaction integrals, we have to find a method that is both fast and accurate. To select the best numerical integration routine we concentrate on the two most difficult parts of the interaction integral: the circle in the (k_x, k_y)-plane where the square root $k_z = \left(k^2 - k_x^2 - k_y^2\right)^{1/2}$ is equal to zero and the exponential factor $\exp\left(i k_x \Delta_x + i k_y \Delta_y\right)$ that oscillates violently when the two holes or pits under consideration are far apart. The square root term would be best tackled with polar coordinates, whereas the exponential term would be easier to integrate with cartesian coordinates. To overcome this problem, we split the integration area in 12 domains. See Figure A.1. From symmetry properties of the integrand, discussed in the previous section, it follows that it suffices to integrate over half the (k_x, k_y)-plane. Furthermore, in the domains 1, 6 and 11 that are situated within the circle $k_x^2 + k_y^2 = k^2$, only the real parts need to be calculated. For the other domains, we only need the imaginary parts:

$$\left\langle \mathscr{A}\left(\boldsymbol{v}_{\bar{\boldsymbol{\alpha}}}\right) \middle| \boldsymbol{v}_{\bar{\boldsymbol{\alpha}}'} \right\rangle_{\Omega_{p'}} = \sum_{N \in \mathscr{N}_{\text{in}}} m_{\text{f}} \operatorname{Re}\left(I_N\right) + \sum_{N \in \mathscr{N}_{\text{out}}} i\, m_{\text{f}} \operatorname{Im}\left(I_N\right), \tag{A.13}$$

with m_{f} a multiplication factor and $\mathscr{N}$ a set of domain numbers:

$$\text{for } \alpha_1 = \alpha_1' : \qquad m_{\text{f}} = 4,\ \mathscr{N}_{\text{in}} = \{1, 11\},\ \mathscr{N}_{\text{out}} = \{2, 3, 4, 5, 12\}, \tag{A.14a}$$

$$\text{for } \alpha_1 \neq \alpha_1' : \qquad m_{\text{f}} = 2,\ \mathscr{N}_{\text{in}} = \{1, 6, 11\},\ \mathscr{N}_{\text{out}} = \{2, 3, 4, 5, 7, 8, 9, 10, 12\}, \tag{A.14b}$$

and with

$$I_N = \iint\limits_{\text{domain } N} I_{\bar{\boldsymbol{\alpha}}\bar{\boldsymbol{\alpha}}'}(k_x, k_y)\, \mathrm{d}k_x \mathrm{d}k_y. \tag{A.15}$$

the double integral over one of the domains.

The two half rings, domains 11 and 12, are called the inner δ-ring $[(k-\delta)^2 \leq k_x^2 + k_y^2 \leq k^2]$ and the outer δ-ring $[(k^2 < k_x^2 + k_y^2 \leq (k+\delta)^2]$. The value of δ is chosen such, that the number of oscillations of the exponential factor inside the rings is small. However, the δ-rings should be wide enough to contain the steepest part of the square root factor (typically larger than or equal to $k/10$). Within the two δ-rings, we choose a polar coordinate system. Furthermore, we apply a substitution to get rid of the square root singularity. We then use a standard, adaptive quadrature routine from the NAG foundation toolbox for Matlab, D01FCF.[2]

Regarding the domains 1 to 10, we assume that the square root factor is sufficiently flat. In these areas, we split the integrand in a slowly varying part and the (possibly) quickly oscillating exponential factor. Domains 1, 2, 6 and 7 are the areas that are bounded by the inner and outer δ-ring. We approximate this boundary linearly on a cartesian grid. The slowly varying part is also approximated linearly, on a cartesian grid. This linear approximation times the exponential factor can now be integrated exactly. The domains 3, 4, 5 and 8, 9, 10 are rectangular areas, bounded by K_1 and k_{max}. Here, we approximate the slowly varying part parabolically and we integrate exactly this parabolic approximation times the exponent.

---

[2] This routine is a multi-dimensional adaptive quadrature over a hyper-rectangle. For a description, see the internet link: http://www.nag.com/nagware/mt/doc/d01fcf.html.

Appendix B

Waveguide mode propagation constants

For a waveguide mode in a pit or hole with index of refraction n_p and sizes L_x and L_y the propagation constant is given by:

$$\gamma_z = \sqrt{\left(\frac{2\pi n_p}{\lambda}\right)^2 - \left(\frac{m_x \pi}{L_x}\right)^2 - \left(\frac{m_y \pi}{L_y}\right)^2}, \tag{B.1}$$

with λ the wavelength in vacuum and m_x and m_y integers. If the index of refraction is taken to be unity, we have:

$$\gamma_z = \frac{\pi}{\lambda}\sqrt{4^2 - \left(\frac{m_x \lambda}{L_x}\right)^2 - \left(\frac{m_y \lambda}{L_y}\right)^2}. \tag{B.2}$$

In the following tables, we give the lowest order propagation constants γ_z in units of $\frac{\pi}{\lambda}$ for various values of L_x and L_y.

$\gamma_z\left(\frac{\pi}{\lambda}\right)$	$m_x = 0$	$m_x = 1$	$m_x = 2$	$m_x = 3$
$m_y = 0$	-	0	$3.5i$	$5.7i$
$m_y = 1$	0	$2i$	$4i$	$6i$
$m_y = 2$	$3.5i$	$4i$	$5.3i$	$6.9i$
$m_y = 3$	$5.7i$	$6i$	$6.9i$	$8.3i$

Table B.1: $L_x = L_y = \frac{1}{2}\lambda$

$\gamma_z\left(\frac{\pi}{\lambda}\right)$	$m_x = 0$	$m_x = 1$	$m_x = 2$	$m_x = 3$
$m_y = 0$	-	$1.5i$	$4.6i$	$7.2i$
$m_y = 1$	$1.5i$	$2.9i$	$5.2i$	$7.6i$
$m_y = 2$	$4.6i$	$5.2i$	$6.8i$	$8.8i$
$m_y = 3$	$7.2i$	$7.6i$	$8.8i$	$10.4i$

Table B.2: $L_x = L_y = \frac{2}{5}\lambda$

$\gamma_z\left(\frac{\pi}{\lambda}\right)$	$m_x = 0$	$m_x = 1$	$m_x = 2$	$m_x = 3$
$m_y = 0$	-	1.1	$2.7i$	$4.6i$
$m_y = 1$	1.1	$1.2i$	$3.1i$	$4.9i$
$m_y = 2$	$2.7i$	$3.1i$	$4.3i$	$5.7i$
$m_y = 3$	$4.6i$	$4.9i$	$5.7i$	$6.8i$

Table B.3: $L_x = L_y = \frac{3}{5}\lambda$

$\gamma_z\left(\frac{\pi}{\lambda}\right)$	$m_x = 0$	$m_x = 1$	$m_x = 2$	$m_x = 3$
$m_y = 0$	-	1.7	0	$2.2i$
$m_y = 1$	1.7	1.4	i	$2.5i$
$m_y = 2$	0	i	$2i$	$3i$
$m_y = 3$	$2.2i$	$2.5i$	$3i$	$3.7i$

Table B.4: $L_x = L_y = \lambda$

$\gamma_z\left(\frac{\pi}{\lambda}\right)$	$m_x = 0$	$m_x = 1$	$m_x = 2$	$m_x = 3$
$m_y = 0$	-	1.94	1.73	1.32
$m_y = 1$	1.94	1.87	1.66	1.22
$m_y = 2$	1.73	1.66	1.41	0.87
$m_y = 3$	1.32	1.22	0.87	$0.71i$

Table B.5: $L_x = L_y = 2\lambda$

Appendix C

Mode expansion theory for a nearby dipole source

C.1 Listing of functions concerning the dipole inside a hole

The right hand part of Equation (7.14) can be calculated with partial integration:

$$\langle \boldsymbol{q} | \boldsymbol{v}_{\bar{\boldsymbol{\alpha}}} \rangle_{\Omega_p} = \begin{cases} -i\omega \dfrac{d}{dz}\delta(z-z_0)\,\mathbf{p}_{\parallel}\cdot \boldsymbol{v}_{\bar{\boldsymbol{\alpha}}}(x_0,y_0)^*, & \text{for TE,} \\ -i\omega \left[p_z\,\delta(z-z_0)\,\nabla_{\parallel} + \dfrac{d}{dz}\delta(z-z_0)\,\mathbf{p}_{\parallel}\right]\cdot \boldsymbol{v}_{\bar{\boldsymbol{\alpha}}}(x_0,y_0)^*, & \text{for TM,} \end{cases} \tag{C.1}$$

if $(x_0,y_0)\in\Omega_p$. If $(x_0,y_0)\notin\Omega_p$, then $\langle \boldsymbol{q} | \boldsymbol{v}_{\bar{\boldsymbol{\alpha}}} \rangle_{\Omega_p}$ equals zero.

The complementary functions $\vartheta_{\bar{\boldsymbol{\alpha}}}$ and $\varphi_{\bar{\boldsymbol{\alpha}}}$ are given by:

$$\vartheta_{\bar{\boldsymbol{\alpha}},z}(\bar{x}_p,\bar{y}_p) = -i\Lambda_{\boldsymbol{\alpha}}\,\Gamma_{\boldsymbol{\alpha}}\,\Pi(\bar{x}_p,\bar{y}_p)\cos(\gamma_x\,\bar{x}_p)\cos(\gamma_y\,\bar{y}_p),\ \text{for } \alpha_2=\text{TE}, \tag{C.2a}$$

$$\varphi_{\bar{\boldsymbol{\alpha}}}(\bar{x}_p,\bar{y}_p) = \frac{-i\Lambda_{\boldsymbol{\alpha}}}{\Gamma_{\boldsymbol{\alpha}}}\,\Pi(\bar{x}_p,\bar{y}_p)\cos(\gamma_x\,\bar{x}_p)\cos(\gamma_y\,\bar{y}_p), \qquad \text{for } \alpha_2=\text{TE}, \tag{C.2b}$$

where we only have defined the functions for TE polarization because, by definition, $H^{\text{part}}_{z,\bar{\boldsymbol{\alpha}}}$ is zero for $\alpha_2=\text{TM}$. We have used $\gamma_x=\frac{m_x\pi}{L_x}$ and $\gamma_y=\frac{m_y\pi}{L_y}$ and we have introduced local coordinates for every pit or hole: $\bar{x}_p \equiv x-x_0^p, \bar{y}_p\equiv y-y_0^p$. The constants $\Lambda_{\boldsymbol{\alpha}}$ and $\Gamma_{\boldsymbol{\alpha}}$ are given by

$$\Lambda_{\boldsymbol{\alpha}} = \begin{cases} 2\left(L_x^p L_y^p\right)^{-1/2}, & \text{if } m_x\neq 0 \text{ and } m_y\neq 0, \\ \sqrt{2}\left(L_x^p L_y^p\right)^{-1/2}, & \text{if } m_x=0 \text{ or } m_y=0, \end{cases} \tag{C.3}$$

and

$$\Gamma_{\boldsymbol{\alpha}} = \sqrt{\gamma_x^2 + \gamma_y^2}. \tag{C.4}$$

Furthermore, the function $\Pi(\bar{x}_p, \bar{y}_p)$ is a rectangle function that indicates that the mode functions are identical to zero outside the cross-sectional area of the p-th hole:

$$\Pi(\bar{x}_p, \bar{y}_p) \equiv \left[\mathrm{H}(\bar{x}_p) - \mathrm{H}(\bar{x}_p - L_x^p)\right]\left[\mathrm{H}(\bar{y}_p) - \mathrm{H}(\bar{y}_p - L_y^p)\right], \tag{C.5}$$

where $\mathrm{H}(x)$ is the Heaviside function.

For TM polarization, the scalar product $\langle Q_z | \varphi_{\bar{\boldsymbol{\alpha}}} \rangle_{\Omega_p}$ is given by:

$$\langle Q_z | \varphi_{\bar{\boldsymbol{\alpha}}} \rangle_{\Omega_p} = \begin{cases} \omega\,\delta(z - z_0)\,\mathbf{p}_\parallel \cdot \boldsymbol{v}_{\bar{\boldsymbol{\alpha}}}(x_0, y_0)^*, & (x_0, y_0) \in \Omega_p, \\ 0, & (x_0, y_0) \notin \Omega_p. \end{cases} \tag{C.6}$$

For TE polarization, the factor $\langle Q_z | \varphi_{\bar{\boldsymbol{\alpha}}} \rangle_{\Omega_p}$ is equal to zero.

The z-dependent part of the particular electric field is given by:

$$e_{\bar{\boldsymbol{\alpha}}}^{\text{part}}(z) = \frac{1}{i\omega\varepsilon_0\varepsilon_p}\left[i\Gamma_{\bar{\boldsymbol{\alpha}}}^2\, H_{z,\bar{\boldsymbol{\alpha}}}^{\text{part}}(z) + \frac{d}{dz}\, h_{\bar{\boldsymbol{\alpha}}}^{\text{part}}(z)\right], \tag{C.7}$$

with

$$H_{z,\bar{\boldsymbol{\alpha}}}^{\text{part}}(z) = \begin{cases} \omega\, u(z - z_0)\,\mathbf{p}_\parallel \cdot \boldsymbol{v}_{\bar{\boldsymbol{\alpha}}}(x_0, y_0)^*, & \alpha_2 = \text{TE}, \\ 0, & \alpha_2 = \text{TM}, \end{cases} \tag{C.8}$$

and

$$\frac{d}{dz}\, h_{\bar{\boldsymbol{\alpha}}}^{\text{part}}(z) = \begin{cases} -i\omega \dfrac{d}{dz}\, v(z - z_0)\,\mathbf{p}_\parallel \cdot \boldsymbol{v}_{\bar{\boldsymbol{\alpha}}}(x_0, y_0)^*, & \text{for TE}, \\ -i\omega\left[p_z\, v(z - z_0)\,\nabla_\parallel + \dfrac{d}{dz}\, v(z - z_0)\,\mathbf{p}_\parallel\right] \cdot \boldsymbol{v}_{\bar{\boldsymbol{\alpha}}}(x_0, y_0)^*, & \text{for TM}, \end{cases} \tag{C.9}$$

where we have used that $\frac{d}{dz}\, u(z) = v(z)$. Furthermore:

$$\frac{d}{dz}\, v(z) = \frac{d^2}{dz^2}\, u(z) = \delta(z) - \gamma_z^2\, u(z), \tag{C.10}$$

with u and v given by Equation (7.16) and δ the Dirac delta function.

C.2 The tangential magnetic field of a dipole above the layer

If a dipole with strength (p_x, p_y, p_z) is located at (x_0, y_0, z_0) above a perfectly conducting layer at $z = D/2$, then the total electromagnetic field is equal to the sum of the free space dipole field of this dipole and the free space field of a so-called mirror dipole with strength $(-p_x, -p_y, p_z)$ and location $(x_0, y_0, D-z_0)$. The terms $\mathbf{h}^i + \mathbf{h}^r$ in Equation (7.39) are thus given by:

$$\mathbf{h}^i + \mathbf{h}^r = \mathbf{h}^{\text{dip}}_{\text{free space}} + \mathbf{h}^{\text{mirror dip}}_{\text{free space}} = \mathbf{h}^{\text{dip}}, \tag{C.11}$$

where the free space fields are calculated from Equation (7.30). In the plane $z = D/2$, the tangential components of the total magnetic field of a dipole near the conducting layer are given by:

$$h_x^{\text{dip}}(x, y, \tfrac{D}{2}) = \frac{ck^2}{2\pi}\left[p_z \frac{x - x_0}{r(x,y)} - p_x \frac{\frac{D}{2} - z_0}{r(x,y)}\right] \frac{e^{ikr(x,y)}}{r(x,y)}\left[1 - \frac{1}{ikr(x,y)}\right], \tag{C.12a}$$

$$h_y^{\text{dip}}(x, y, \tfrac{D}{2}) = \frac{ck^2}{2\pi}\left[p_z \frac{y - y_0}{r(x,y)} - p_y \frac{\frac{D}{2} - z_0}{r(x,y)}\right] \frac{e^{ikr(x,y)}}{r(x,y)}\left[1 - \frac{1}{ikr(x,y)}\right], \tag{C.12b}$$

with

$$r(x,y) = \sqrt{(x-x_0)^2 + (y-y_0)^2 + (D/2 - z_o)^2}. \tag{C.13}$$

C.3 Spectral amplitude function of the scattered field

The spectral decomposition of the scattered electric field is given by:

$$\mathbf{E}^s(r, \varphi, \theta) = \iint_{-\infty}^{\infty} \mathbf{A}^s(k_x, k_y) e^{ir\Phi(k_x, k_y; \varphi, \theta)}\, \mathrm{d}k_x \mathrm{d}k_y. \tag{C.14}$$

The spectral amplitude function is given by:

$$\mathbf{A}^s(k_x, k_y) = \frac{k_u \omega \mu_0}{2\pi} \frac{e^{-ik_z^u D/2}}{\sqrt{k_x^2 + k_y^2}} \left[b^{\text{S}} (\mathbf{n} \times \hat{\boldsymbol{\imath}}_z) - b^{\text{P}} (\mathbf{n} \times \hat{\boldsymbol{\imath}}_z) \times \mathbf{n}\right], \tag{C.15}$$

with $\mathbf{n} = (\cos\varphi \sin\theta, \sin\varphi \sin\theta, \cos\theta)$.

Bibliography

[1] J. Jackson, *Classical Electrodynamics*, 3rd ed. New York: Wiley, 1999.

[2] J. S. Schwinger, L. L. DeRaad, and Kimball, A. M., *Classical Electrodynamics*. Massachusetts: Perseus Books, 1998.

[3] L. Ward, *The Optical Constants of Bulk Materials and Films*, 2nd ed. Bristol: IOP publishing Ltd, 1994.

[4] J. A. Stratton, *Electromagnetic Theory*. New York: McGraw-Hill, 1941.

[5] H. Raether, *Surface Plasmons on Smooth and Rough Surfaces and on Gratings*, 1st ed. Berlin: Springer-Verlag, 1988.

[6] E. D. Palik, *Handbook of Optical Constants of Solids*. New York: Academic Press, 1985.

[7] M. A. Ordal, R. J. Bell, R. W. Alexander, Jr., L. L. Long, and M. R. Querry, "Optical properties of fourteen metals in the infrared and far infrared - Al, Co, Cu, Au, Fe, Pb, Mo, Ni, Pd, Pt, Ag, Ti, V, and W," *Appl. Opt.*, vol. 24, pp. 4493–4499, Dec. 1985.

[8] M. Born and E. Wolf, *Principles of Optics*. London: Pergamon Press, 1959.

[9] J. J. Bowman, T. B. A. Senior, and P. L. E. Uslenghi, *Electromagnetic and acoustic scattering by simple shapes (Revised edition)*. New York, Hemisphere Publishing Corp., 1987.

[10] J. Meixner and W. Andrejewski, "Strenge Theorie der Beugung ebener elektromagnetischer Wellen an der vollkommen leitenden Kreisscheibe und an der kreisförmigen Öffnung im vollkommen leitenden ebenen Schirm," *Annalen der Physik*, vol. 442, pp. 157–168, 1950.

[11] A. Roberts, "Electromagnetic theory of diffraction by a circular aperture in a thick, perfectly conducting screen," *J. Opt. Soc. Am. A*, vol. 4, pp. 1970–1983, 1987.

[12] J. v. Bladel, *Singular Electromagnetic Fields and Sources*, 1st ed. Oxford: Clarendon Press, 1991.

[13] F. Garcia-Vidal, E. Moreno, J. Porto, and L. Martin-Moreno, "Transmission of light through a single rectangular hole," *Phys. Rev. Lett.*, vol. 95, p. 103901, 2005.

[14] N. C. J. van der Valk, T. Wenckebach, and P. C. M. Planken, "Full mathematical description of electro-optic detection in optically isotropic crystals," *J. Opt. Soc. Am. B*, vol. 21, pp. 622–631, Mar. 2004.

[15] G. Zhao, R. N. Schouten, N. van der Valk, W. T. Wenckebach, and P. C. M. Planken, "Design and performance of a THz emission and detection setup based on a semi-insulating GaAs emitter," *Review of Scientific Instruments*, vol. 73, pp. 1715–1719, Apr. 2002.

[16] N. C. J. van der Valk and P. C. M. Planken, "Electro-optic detection of sub-wavelength terahertz spot sizes in the near field of a metal tip," *Appl. Phys. Lett.*, vol. 81, pp. 1558–1560, Aug. 2002.

[17] N. C. J. van der Valk, "Towards terahertz microscopy," PhD Dissertation, Delft University of Technology, 2005, http://www.library.tudelft.nl/dissertations.

[18] H. Bethe, "Theory of diffraction by small holes," *Phys. Rev.*, vol. 66, p. 163, 1944.

[19] C. Flammer, "The vector wave function solution of the diffraction of electromagnetic waves by circular disks and apertures. i. oblate spheroidal vector wave functions," *J. Appl. Phys.*, vol. 24, pp. 1218–1223, 1953.

[20] C. Flammer, "The vector wave function solution of the diffraction of electromagnetic waves by circular disks and apertures. ii. the diffraction problems," *J. Appl. Phys.*, vol. 24, pp. 1224–1231, 1953.

[21] C. Bouwkamp, "Diffraction theory," *Reports on progress in physics*, vol. 17, pp. 35–100, 1954.

[22] T. Ebbesen, H. Lezec, H. Ghaemi, T. Thio, and P. Wolff, "Extraordinary optical transmission through sub-wavelength hole arrays," *Nature*, vol. 391, pp. 667–669, 1998.

[23] H. Schouten, T. Visser, D. Lenstra, and H. Blok, "Light transmission through a subwavelength slit: Waveguiding and optical vortices," *Phys. Rev. E*, vol. 67, p. 036608, 2003.

[24] J. Bravo-Abad, L. Martin-Moreno, and F. Garcia-Vidal, “Transmission properties of a single metallic slit: From the subwavelength regime to the geometrical-optics limit,” *Phys. Rev. E*, vol. 69, p. 026601, 2004.

[25] H. Schouten, N. Kuzmin, G. Dubois, T. Visser, G. Gbur, P. Alkemade, H. Blok, G. Hooft, D. Lenstra, and E. Eliel, “Plasmon-assisted two-slit transmission: Young’s experiment revisited,” *Phys. Rev. Lett.*, vol. 94, p. 053901, 2005.

[26] M. Moharam and T. Gaylord, “Rigorous coupled-wave analysis of metallic surface-relief gratings,” *J. Opt. Soc. Am. A*, vol. 3, pp. 1780–1787, 1986.

[27] J. Porto, F. Garcia-Vidal, and J. Pendry, “Transmission resonances on metallic gratings with very narrow slits,” *Phys. Rev. Lett.*, vol. 83, pp. 2845–2848, 1999.

[28] Q. Cao and P. Lalanne, “Negative role of surface plasmons in the transmission of metallic gratings with very narrow slits,” *Phys. Rev. Lett.*, vol. 88, p. 057403, 2002.

[29] L. Martin-Moreno and F. Garcia-Vidal, “Optical transmission through circular hole arrays in optically thick metal films,” *Opt. Express*, vol. 12, pp. 3619–3628, 2004.

[30] S. Chang, S. Gray, and G. Schatz, “Surface plasmon generation and light transmission by isolated nanoholes and arrays of nanoholes in thin metal films,” *Opt. Express*, vol. 13, pp. 3150–3165, 2005.

[31] F. d. Abajo, “Light transmission through a single cylindrical hole in a metallic film,” *Opt. Express*, vol. 10, pp. 1475–1484, 2002.

[32] J. Pendry, L. Martin-Moreno, and F. Garcia-Vidal, “Mimicking surface plasmons with structured surfaces,” *Science*, vol. 305, p. 847, 2004.

[33] A. Hibbins, B. Evans, and J. Sambles, “Experimental verification of designer surface plasmons,” *Science*, vol. 308, p. 670, 2005.

[34] A. E. Siegman, *Lasers*. Mill Valley: University Science Books, 1986.

[35] T. H. Koornwinder, *The topological degree of a mapping*, ser. Nonlinear Analysis, N. M. Temme, Ed. Amsterdam: Mathematisch Centrum, 1980, vol. 1.

[36] M. S. Soskin and M. V. Vasnetsov, *Singular optics*, ser. Progress in Optics, E. Wolf, Ed. Amsterdam: Elsevier, 2001, vol. 42.

[37] C. Kittel, *Introduction to Solid State Physics*, 7th ed. New York: Wiley, 1996.

[38] J. M. Brok and H. P. Urbach, “Rigorous model of the scattering of a focused spot by a grating and its application in optical recording,” *Journal of the Optical Society of America A*, vol. 20, pp. 256–272, Feb. 2003.

[39] C. M. Bender and S. A. Orszag, *Advanced mathematical methods for scientists and engineers.* McGraw-Hill Book Company, New York, 1978.

[40] J. J. Stamnes, *Waves in focal regions. Propagation, diffraction and focusing of light, sound and water waves.* Adam Hilger Series on Optics and Optoelectronics, Bristol, 1986.

[41] G. C. Sherman, J. J. Stamnes, and E. Lalor, "Asymptotic approximations to angular-spectrum representations," *J. Math. Phys.*, vol. 17, no. 5, pp. 760–776, 1976.

[42] E. Wolf and J. T. Foley, "Do evanescent waves contribute to the far field?" *Opt. Lett.*, vol. 23, pp. 16–18, Jan. 1998.

[43] M. V. Berry, "Asymptotics of evanescence," *J. Mod. Opt.*, vol. 48, pp. 1535–1541, Oct. 2001.

[44] E. M. Purcell, "Spontaneous emission probabilities at radio frequencies," *Phys. Rev. Lett.*, vol. 69, p. 681, 1946.

[45] K. H. Drexhage, *Interaction of light with monomolecular dye layers*, ser. Progress in Optics, E. Wolf, Ed. North-Holland Publishing Company, 1974, vol. 12.

[46] R. R. Chance, A. Prock, and R. Silbey, "Comments on the classical theory of energy transfer," *J. Chem. Phys.*, vol. 62, pp. 2245–2253, Mar. 1975.

[47] D. Kleppner, "Inhibited Spontaneous Emission," *Phys. Rev. Lett.*, vol. 47, pp. 233–236, July 1981.

[48] S. M. Dutra and P. L. Knight, "Spontaneous emission in a planar Fabry-Pérot microcavity," *Phys. Rev. A*, vol. 53, pp. 3587–3605, May 1996.

[49] K. G. Sullivan and D. G. Hall, "Enhancement and inhibition of electromagnetic radiation in plane-layered media. I.Plane-wave spectrum approach to modeling classical effects," *J. Opt. Soc. Am. B*, vol. 14, pp. 1149–1159, May 1997.

[50] H. P. Urbach and G. L. J. A. Rikken, "Spontaneous emission from a dielectric slab," *Phys. Rev. A*, vol. 57, pp. 3913–3930, May 1998.

[51] W. L. Barnes, "Fluorescence near interfaces: the role of photonic mode density," *J. Mod. Opt.*, vol. 45, pp. 661–699, Apr. 1998.

[52] Y. Xu, J. S. Vuckovic, R. K. Lee, O. J. Painter, A. Scherer, and A. Yariv, "Finite-difference time-domain calculation of spontaneous emission lifetime in a microcavity," *J. Opt. Soc. Am. B*, vol. 16, pp. 465–474, Mar. 1999.

[53] S. Noda, K. Tomoda, N. Yamamoto, and A. Chutinan, "Full Three-Dimensional Photonic Bandgap Crystals at Near-Infrared Wavelengths," *Science*, vol. 289, pp. 604–606, July 2000.

[54] V. V. Klimov, M. Ducloy, and L. V. S., "Spontaneous emission of an atom in the presence of nanobodies," *Quant. Electron.*, vol. 31, no. 7, pp. 569–586, 2001.

[55] L. A. Blanco and F. J. Garcia de Abajo, "Spontaneous emission enhancement near nanoparticles," *J. Quant. Spectrosc. Radiat. Transfer*, vol. 89, pp. 37–42, Nov. 2004.

[56] L. Rogobete and C. Henkel, "Spontaneous emission in a subwavelength environment characterized by boundary integral equations," *Phys. Rev. A*, vol. 70, no. 6, pp. 063 815–+, Dec. 2004.

[57] S. Haroche, *Cavity quantum electrodynamics*, ser. Fundamental systems in quantum optics, J. Dalibard, J. M. Raimond, and J. Zinn-Justin, Eds. Elsevier, 1992.

Nawoord

Dat was dat. Proefschrift af, promotie bijna achter de rug. Een korte terugblik.

Het onderzoek. Het duurde wel een tijdje voor we de juiste notatie voor het verstrooiingsprobleem gevonden hadden. Ook het nauwkeurig uitrekenen van de interactie-integraal bleek niet eenvoudig. Uitzicht op de horizon, waar het naar toe moet, is in de wetenschap meestal niet gegeven. Dat ik aan Paul Urbach een goede promotor zou hebben, dat was na mijn afstuderen al wel duidelijk. Je enthousiasme voor wis- en natuurkunde werkt aanstekelijk, maar ook je warme persoonlijke belangstelling maakt de samenwerking prettig. Hoe je zo snel altijd weer in de stof zit, na een halve zin door de telefoon, of tussen een college en een vergadering door op vrijdag, is me nog steeds een raadsel. En hoewel je het behoorlijk druk hebt, hoef ik nooit lang te wachten op een antwoord. Een speciaal woord van dank wil ik hier ook richten aan Roland Horsten. Ik weet niet waar ik zonder jouw ondersteuning op het gebied van software en hardware zou zijn geweest. Furthermore, I mention the fruitful cooperation with Paul Planken, Aurèle Adam and Minah Seo. With the experimental setup and the samples, you were able to perform experiments that could be compared directly with my calculations. Although not anticipated in the beginning of my research, this symbiosis turned out to be a most rewarding way of doing research and I feel fortunate to have experienced this. Natuurlijk vergeet ik niet hier ook Yvonne van Aalst en Lucia Heijenga te bedanken, die met hun administratieve ondersteuning het leven op de TU stukken gemakkelijker maken. En Jos Burger, voor zijn hulp bij Figuur 1.1.

De collega's. Optica was en is een gezellige groep. Soms vreesde ik dat met het vertrekken van mijn collega-promovendi ook de gezelligheid beetje bij beetje zou verdwijnen, maar dat bleek geenszins het geval. Optica-uitjes, kerstdiner, fietsen naar Jaarsveld, mtb-en in Limburg, het filmfestival in Rotterdam (de film kon soms beter), filmavonden in onze eigen bibliotheek, de kamercompetitie, maar vooral de zinnige en onzinnige discussies tijdens de koffie en de lunch, ze vormen het cement van de groep. Een speciaal woord van dank aan mijn kamergenoten Luke, Iciar, Arthur, Sami, Sven en Olaf is hier op zijn plaats.

Buiten het werk. Het belangrijkst voor een mens zijn diens vrienden, heeft een dierbare persoon me ooit gezegd. Vriendschappen vormen zich bij gedeelde bezigheden. Samen eten, discussies over van alles en nog wat. Samen fietsen, mooie kilometers maken, trainingen, wedstrijden, weekendjes weg. De verhalen en belevenissen komen vanzelf. Studentenwielervereniging WTOS bleek wat dat betreft een warm bad. Mijn ploeg Vrienden van het Platteland en mijn club Het Snelle Wiel wil ik bedanken voor het delen van mijn enthousiasme voor en het stimuleren van mijn ambities in het wielrennen.

Wouter en Cas, mijn paranimfen, bedankt voor jullie vriendschap en steun. Mijn ouders, bij wie het prettig thuiskomen is, voor jullie frisse blik en vanzelfsprekende vertrouwen. En Alex, mijn lief, om jou te bedanken heb ik geen woorden nodig.

Janne Brok, mei 2007

About the author

Janne Brok was born in 1978 in ’s-Hertogenbosch, the Netherlands. She studied Applied Physics at Eindhoven University of Technology. Her master thesis project was carried out in 2001 at Philips Research Laboratories under the guidance of Professor Urbach, her present promotor. The subject was vector diffraction and polarization effects in DVD-like structures. After doing a one year master study in Applied Ethics at the University of Leuven, Belgium, she started her PhD in the Optics Research Group of Professor Braat at Delft University of Technology, in 2002. During this PhD, she attended the summer school *Vortices: a Unifying Concept in Physics* in Cargése, Corsica, and the winter school *Quantum and Classical Aspects of Information Optics* in Trieste, Italy. Janne has presented large parts of this thesis at conferences in Oxford, Rochester, Warwick, St. Petersburg, Lunteren and Paris. Janne is a passionate racing cyclist. In addition to her work as a PhD, she has joined the professional women’s cycling team *Vrienden van het Platteland* in 2006 to compete in national, as well as international races.

List of publications

J.M. Brok and H.P. Urbach, Simulation of polarization effects in diffraction problems of optical recording, Journal of Modern Optics, Volume 49, Issue 11, pp. 1811-1829, November 2002.

J.M. Brok and H.P. Urbach, Rigorous model of the scattering of a focused spot by a grating and its application in optical recording, Journal of the Optical Society of America A, Volume 20, Issue 2, pp. 256-272, February 2003.

J.M. Brok and H.P. Urbach, A mode expansion technique for rigorously calculating the scattering from 3D subwavelength structures in optical recording, Journal of Modern Optics, Volume 51, Issue 14, pp. 2059-2077, January 2005.

J.M. Brok and H.P. Urbach, Extraordinary transmission through 1, 2 and 3 holes in a perfect conductor, modelled by a mode expansion technique, Optics Express, Volume 14, Issue 7, pp. 2552-2572, April 2006.

A.J.L. Adam, J.M. Brok, P.C.M. Planken, M.A. Seo, and D.S. Kim, THz near-field measurements of metal structures, submitted to Comptes Rendus Physique.

J.M. Brok and H.P. Urbach, Spontaneous emission calculations near sub-wavelength pits and holes, in preparation.